TUFTS UNIVERSITY

DOE/ER/40085-19
Tufts University
May 1, 1990

A Study of Intranuclear Rescattering in ν_μ -Ne versus ν_μ -D Interactions: Implications for Nucleon Decay Searches

Robert C. Merenyi

(Ph.D. dissertation)

DOE/ER/40085--19

DE90 010662

ABSTRACT

Pion intranuclear rescattering rates are determined for processes which can distort reaction final states observed and/or searched for in nucleon decay experiments. We compare the interactions of low energy neutrinos with neon versus deuterium nuclei, weighted to simulate the atmospherically-induced neutrino spectrum. The pion charge exchange and absorption rates, expressed as probabilities per final state pion, are measured to be 0.05 ± 0.09 and 0.23 ± 0.08, respectively. Using the excess momentum degraded, backscattered pions in neon relative to deuterium, we measure a lower limit for π^- inelastic rescattering to be 0.11 ± 0.10 and for π^+ to be 0.03 ± 0.04. The apparent charge dependence of $\pi^\pm$ inelastic rates may be associated with abundant Δ^{++} production in threshold ν_μ interactions. The resonance lifetime allows "transport" of π^+ mesons to the lower density nuclear periphery, prior to $\Delta^{++} \rightarrow p\pi^+$ decay. The pion rescattering rates are used to calibrate a simple phenomenological cascade model for A = 20. The model enables extrapolation of pion rescattering rates for higher atomic number nuclei, e.g. argon and iron, detector media which are being employed in second generation current nucleon decay searches.

ACKNOWLEDGEMENTS

I wish to take this opportunity to thank those people whose efforts made the research described in this Thesis possible. My supervisor, Prof. W. Anthony Mann, has been very patient and enthusiastic during all phases of the research. Our late night discussions served to resolve many anomalous results and to define new avenues of investigation.

To the faculty and research staff of Bacon Hall a sincere thank you is due for making my sojourn at Tufts University pleasant and enjoyable. Special appreciation is extended to Larry McMaster for his encouragement, support, and lasting friendship.

My deepest affection and appreciation to my wife Celia and our son Alex whose patience, encouragement, and love made this endeavor a reality. After four years, I return the dining room table sans notes, printout, and preprints.

TABLE OF CONTENTS

TABLE OF CONTENTS (Continued)

TABLE OF CONTENTS (Continued)

TABLE OF CONTENTS (Continued)

TABLE OF CONTENTS (Continued)

LIST OF TABLES

LIST OF TABLES (Continued)

LIST OF TABLES (Continued)

LIST OF FIGURES

LIST OF FIGURES (Continued)

LIST OF FIGURES (Continued)

LIST OF FIGURES (Continued)

A STUDY OF INTRANUCLEAR RESCATTERING

IN ν_μ-Ne VERSUS ν_μ-D INTERACTIONS:

IMPLICATIONS FOR

NUCLEON DECAY SEARCHES

CHAPTER 1

INTRODUCTION

Attempts to unify the electroweak and strong interactions have led to predictions that baryon number is not strictly conserved[1]. The simplest of the hypothesized grand unification theories (GUTs), those based on the symmetry group SU(5), initially predicted a lifetime for the proton to be on the order of 10^{29} years[2]. However, ninety-percent confidence level limits on proton lifetimes as determined by nucleon decay experiments have been steadily increasing, and recently published limits would seem to exclude lifetimes on the order of 10^{31}-10^{32} years[3,4]. These lifetimes eliminate minimal SU(5) GUTs, constrain supersymmetric (SUSY) grand unification models[5], and impose limits on supergravity models[6].

The current lifetime limits and new GUT model predictions pose serious challenges to searches for, and analysis of, nucleon decay candidates. Supersymmetric GUT models favor decay modes yielding final state neutrinos and strange mesons,

$$N \rightarrow (\bar{\nu}_\ell) + K, \quad \ell = \tau, \mu, e \qquad (1\text{-}1)$$

neutrinos and non-strange mesons,

$$N \rightarrow \begin{pmatrix} \bar{\nu}_\ell \end{pmatrix} + M, \quad \ell = \tau, \mu, e \qquad (1\text{-}2)$$

and also charged leptons and strange mesons,

$$N \rightarrow \ell^{\pm} + K, \quad \ell = \mu, e \qquad (1\text{-}3)$$

while still permitting the SU(5)-favored decay channels

$$N \rightarrow \ell^{\pm} + M, \quad \ell = \mu, e \qquad (1\text{-}4)$$

allbeit with reduced branching ratios[7]. Detection of nucleon halflives on the order of 10^{32} years within a reasonable amount of time requires a material sample weighing more than a metric kiloton. Since such a large sample of pure hydrogen is impractical, heavier nuclei must be used. Thus, two critical issues in nucleon decay search experiments are (i) the detection of proton or neutron decay rates (or rate limits) into various possible decay modes, and (ii) seperatio of these presumably rare events from background processes, particularly interactions induced by atmospheric neutrinos in underground detectors. It is to the latter issue that this Thesis is addressed.

In many grand unification schemes[8], nucleon decay will result in the production of final state pions; from phase space considerations, two-body modes might be expected to be dominant, e.g.,

$$p \rightarrow \pi^0 e^+, \quad n \rightarrow \pi^- e^+. \qquad (1\text{-}5)$$

Though an underlying GUT dynamics may mitigate against these simple modes, all significant observational problems can be readily characterized using them. For this reason, modes (1-5) will be utilized in this Chapter for illustrative discussions. For any nucleon decay mode, the kinematic quantities of final state particles will be smeared due to Fermi motion, and the produced hadrons can possibly interact with other nucleons before emerging

from the nucleus. The likelihood of intranuclear rescattering by final state hadrons thus has a direct bearing on the ease with which nucleon decay can be identified.

Crucial to any nucleon decay analysis is the understanding and predicting of background contamination due to atmospheric neutrino interactions with the detector material. For example, events of the type

$$\nu + N \rightarrow \ell + N' + M, \tag{1-6}$$

in which the recoil nucleon is below detector threshold, can mimic nucleon decay if the lepton and the meson are sufficiently back-to-back to simulate

$$N \rightarrow \ell + M. \tag{1-7}$$

In addition, atmospherically-induced neutrino interactions can yield multi-meson final states. The final state hadrons can be absorbed, charge exchanged, and/or scattered, and so can fake nucleon decay signatures.

Neutrino interactions which can conceivably imitate nucleon decays can be usefully divided into five categories:

i) Charged current quasi-elastic scattering ($\nu+N \rightarrow \ell^{\pm}+N'$);

ii) Charged currents at the Δ resonance ($\nu+N \rightarrow \ell^{\pm}+N'+\pi$);

iii) Charged current multi-π production ($\nu+N \rightarrow \ell^{\pm}+N'+m\pi$);

iv) Neutral currents at the Δ resonance ($\nu+N \rightarrow \nu+N'+\pi$);

v) Neutral current multi-π production ($\nu+N \rightarrow \nu+N'+m\pi$).

These neutrino event categories will be referred to in discussions to follow.

Methods to estimate both the rate and character of neutrino-induced backgrounds to nucleon decay modes, including the extent of intranuclear rescattering effects, include:

α) Exposing a representative portion of a nucleon decay detector to a low energy accelerator neutrino beam;

β) Calculating exclusive channel rates for all relevant atmospheric neutrino interactions and modeling the final state pion production and subsequent propagation within the nucleus;

γ) Analyzing existing accelerator neutrino data taken with an energy distribution nearly that of atmospheric neutrinos.

It should be noted that all three methods (hereafter referred to as Methods α), β), and γ)) require use of the atmospheric neutrino energy spectrum and flux, as calculated be several authors[9], to determine background neutrino contamination. These calculations employ both muon- and electron-neutrino and anti-neutrino fluxes. The computations are tuned for specific nucleon decay search experiments by setting the $\nu/\bar{\nu}$ ratio to duplicate the cosmic ray-produced μ^+/μ^- ratio as observed at sea level at the detector latitude.

1.1 Exposure of Nucleon Decay Detectors to Accelerator Neutrino Beams

Determination of nuclear interaction rates via Method α) requires an accelerator neutrino beam with an energy spectrum as close as possible to that of atmospherically-produced neutrinos. The NUSEX collaboration performed such an experiment[10], using a test module similar to their Mont Blanc calorimeter detector in a dedicated CERN experiment. The test module, consisting of iron plates interleaved with planes of plastic streamer tubes filled with an argon-isobutane gas mixture, had a 1 cm

spatial resolution in both views of the detector plane. For the Soudan II experiment, a calibration exposure, employing standardized tracking calorimeter modules in the BNL neutrino beam line, has been proposed[11]. The Soudan detector is assembled by close-packing five-ton modules, each of which contains steel sheets with hexagonal corrugations. The corrugations are stacked so as to form a lattice of long, hexagonal cells. Each cell encloses a separate drift tube made of resistive plastic filled with an argon-CO_2 gas mixture. The modules have three-dimensional spatial resolution of order 5 mm per axis.

1.2 Calculations of Intranuclear Rescattering Effects

In Background Method β), a complete simulation is attempted of pion production and propagation within the nucleus and in the detector, taking into account Fermi motion, charge exchange, scattering, and absorption of pions both inside and outside the nucleus in which the neutrino interacts. Calculation of pion production within the nucleus is frequently based on the Sternheim and Silbar[12] model for π-production in the $\Delta(3,3)$-resonance region. The original model utilizes proton-nucleon scattering data to determine the nuclear pion absorption cross section. Adler, Nussinov, and Paschos[13] (ANP) modified this model to examine leptonic pion production on a nuclear target by employing the experimental pion-nucleon charge exchange cross section. Additionally, the ANP model improves the Sternheim and Silbar approximation for multiple pion scattering.

The ANP model differs significantly with the earlier work by assuming a two-step process for leptonic nuclear pion production. In the first step, pions are produced from constituent nucleons of the target nucleus with the free lepton-nucleon cross section, subject to a Pauli-principle reduction factor. In the second step, the produced pions undergo nuclear interactions involving pion scattering, charge exchange, and absorption in two-nucleon or more complex nuclear processes. The ANP model characterizes the effects of nuclear rescattering in forward and backward directions with a 3x3 matrix, the elements of which depend on nuclear size and pion energy. These parameters have been used by a number of authors[14,15] to compute corrections to pion propagation in nuclear matter.

The ANP model was first used to study pion attenuation following nucleon decay by D.A.Sparrow[16]. In the calculation by Sparrow, pions are produced via intermediate Δ-production with the mean free path calculated using proton-proton scattering data. The resulting pions propagate in their original direction subject to absorption and quasi-free charge exchange as described by semi-classical transport equations.

More recently, Rein and Sehgal[17] give a complete treatment of ν-induced pion production in the region of nucleon resonances up to 2 GeV in center-of-mass energy. For the $\Delta(1232)$, which has the largest production cross section in the nucleon region, the Rein and Sehgal model assumes isotropic decay in the Δ rest frame, leading to uniform distribution in pion laboratory energy.

Calculations of pion propagation often follow the example of the ANP model[13] which assumes the target nucleus to be a collection of

independent nucleons. The nucleons are spatially distributed with a density profile determined by electron scattering experiments. For aluminum and lighter nuclei, the ANP model uses the harmonic well parameterization of the nucleon density and regards nucleons to be fixed within the nucleus. Thus, the ANP pion propagation model neglects Fermi motion and nucleon recoil effects. The model assumes incoherent pion-nucleon interactions and uses π-N cross sections to determine multiple scattering probabilities in one dimension.

Since the model of Sparrow[16] considers only pions produced from nucleon decay, the propagation problem in this later model is reduced to the calculation of the survival of specific energy pions appearing suddenly inside a nucleus. By assuming that the decay of any particular neutron or proton occurs uniformly throughout the nucleus, Sparrow expresses the probability of pion survival as an integral over the nuclear density. Using an Eikonal approximation, the integral is simplified to a calculation of the nuclear density in the direction of pion travel. The probabilities are computed using pion absorption and charge exchange cross sections. In this way, for example, Sparrow determines the probability that the π° will escape the nucleus without nuclear rescattering following the decay $p \rightarrow \pi^\circ e^+$ to be approximately 0.33.

A phenomenlogically different treatment of pion-nucleus interactions is presented by Zavarzina, Sergeev, and Stepanov[18]. This work assumes that the strong interaction of the pion with the residual nucleus can be described via a pion wave distorted by an optical potential. Their model correlates the expected π°-e^+ angular distribution from proton decay with

nucleon Fermi motion and predicts a 0.40 survival probability for the final state π°.

Modeling of intranuclear pion propagation seems to have undergone a reorientation in early 1982 with the "rediscovery" of the internuclear cascade concept of particle-nuclear interaction. First implemented by Bertini[19] in 1972, the cascade model assumes that particle nuclear interactions can be treated as a series of two-body collisions within the nucleus and that the location of the collision, and resulting particles from the collisions, are governed by particle-particle cross section data. In this way, the mean free paths of pion absorption, charge exchange, and scattering are calculated from experimental data and the angular and momentum distributions of scattered pions are obtained from π-N scattering data, taking into account the Pauli principle and Fermi motion.

Among the first authors to employ the cascade model were Gabriel and Goodman[20], who replaced the original nuclear model with a smoothly decreasing nuclear density profile based on e-^{16}O scattering data. Nuclear potentials are determined from this profile by using a zero-temperature Fermi distribution. The total nucleon potential well depth is then defined as the Fermi energy plus 7 MeV (which represents the average binding energy of the most loosely bound nucleon). The location, initial direction, and energy of decaying protons are sampled from the well potentials with the nucleon kinematics determining the directions and energies - upon decay - of the e^{+} and π°. The pions are subsequently propagated through the nuclear media (^{16}O, ^{56}Fe, and ^{207}Pb), subject to nuclear interactions, to determine the pion survival probability. This basic model has been used by a number

of researchers[21,22], with details tuned to particular detector configurations search for nucleon decay.

Variations of the cascade model have included the use of photoproduction pion cross sections[23] (to more accurately reflect isotropic nucleon decay), different nuclear density profiles[24], and the effects of virtual meson exchange[25] on nucleon decay. The effects of various model alterations can be roughly gauged from Table 1-1, which is a compendium of fate probabilities for neutral pions, produced in the decay reaction $p \rightarrow \pi^0 e^+$ interacting with ^{16}O.

1.3 Intranuclear Rescattering Determined From Existing Neutrino Data

The third approach to determining intranuclear rescattering rates, Method γ), requires analysis of existing accelerator neutrino data taken with neutrino beam spectra as close as possible to that of atmospheric neutrinos. Approach γ), with ν-D and ν-Ne data sets, is the one taken by this Thesis.

The outline of the Thesis is as follows: Chapters 2 and 3 describe the two neutrino interaction data sets, selection criteria, and event weights used for the analysis. Chapter 4 details the weighting technique used to simulate atmospheric neutrino interactions. Chapter 5 presents inclusive and exclusive reaction channel comparisons between the two data sets. Pion intranuclear rescattering, as observed in the data sets, is examined in Chapters 6, 7, 8, and 9. A summary of the results and their implications for nucleon decay is discussed in Chapter 10.

TABLE 1-1

COMPENDIUM OF PUBLISHED RESULTS FOR
π°-^{16}O INTRANUCLEAR INTERACTIONS

Author	π° Fate		
	No Interaction	Charge Exchange	Absorption
D.A.Sparrow[16]	0.33	-	-
V.P.Zavarzina, V.A.Sergeev, and A.V.Stepanov[18]	0.40	-	-
T.A.Gabriel and M.S.Goodman[20]	0.39	-	-
A.Nishimura and K.Takahashi[26]	0.49	0.11	0.27
B.A.Meking[21]	0.42	0.12	0.20
N.Nakahata, et al.[22]	0.43	0.16	0.14

References

1. J.Pati and A.Salam, Phys. Rev. D 10, 275 (1974); H.Georgi and S.L.Glashow, Phys. Rev. Lett. 32, 438 (1975).
2. H.Georgi, H.Quinn, and S.Weinberg, Phys. Rev. Lett. 33, 151 (1974); H.Buras et al., Nucl. Phys. B135, 66 (1978); D.Ross, Nucl. Phys. B140, 1 (1978); T.Goldman and D.Ross, Phys. Lett. 84B, 208 (1978).
3. Ch. Berger et al., LAL-88-34 1988 (unpublished).
4. T.J.Haines et al., Phys. Rev. Lett. 57, 1986 (1986), S.Seidel et al. Phys. Rev. Lett. 61, 2522 (1988).
5. W.J.Marciano in Eigth Workshop on Grand Unification, ed. K.C.Wali, World Scientific Publishing (Singapore), chapter 4 (1988).
6. P.Nath and R.Arnowitt, Phys. Rev. D 38, 1479 (1988).
7. W.Lucha, Comments Nucl. Part. Phys. 16, 155 (1986).
8. see, e.g., P.Langacker, Phys. Rep. 72, 185 (1981).
9. A.W.Wolfendale et al., Proc. Phys. Soc. 86, 93 (1965); E.C.M.Young in Cosmic Rays at Ground Level, ed. A.W.Wolfendale, The Institute of Physics (London), chapter 6 (1973); D.C.Cundy in Neutrino 81, proceedings of the International Conference on Neutrino Physics and Astrophysics, Maui, Hawaii 1981, ed. R.J.Cence, E.Ma, and A.Roberts (University of Hawaii, Honolulu, 1981).
10. G.Battistoni et al., Nucl. Instrum. Methods 219, 300 (1984).
11. W.A.Mann et al., BNL Proposal 841 (1987).
12. M.M.Sternheim and R.R.Silbar, Phys. Rev. D 6, 3117 (1972).
13. S.L.Adler, S.Nussinov, and E.A.Paschos, Phys. Rev. D 9, 2125 (1974).

14. W.Krenz et al., Nucl. Phys. B135, 45 (1978).

15. T.K.Gaisser, M.Nowakowski, and E.A.Paschos, Phys. Rev D 33, 1233 (1986).

16. D.A.Sparrow, Phys. Rev. Lett. 44, 625 (1980).

17. D.Rein and L.M.Sehgal, Ann. Phys. (N.Y.) 133, 79 (1981).

18. V.P.Zavarzina, V.A.Sergeev, and A.V.Stepanov, Sov. J. Nucl. Phys. 36, 101 (1982).

19. H.W.Bertini, Phys. Rev. C 6, 631 (1972).

20. T.A.Gabriel and M.S.Goodman, Phys. Rev. D 25, 2463 (1982).

21. D. Rein, Phys. Rev. D 28, 1800 (1983).

22. H.Nakahata et al., J. Phys. Soc. Jpn. 55, 3786 (1986).

23. B.A.Meking, BONN-HE-84-19, 1984 (unpublished).

24. H.E.Miettinen and P.M.Stevenson, Phys. Lett. 1998, 591 (1987).

25. E.Oset, Nucl. Phys. B304, 820 (1988).

26. A.Nishimura and K.Takahashi, KEK-82-6, 1982 (unpublished).

CHAPTER 2

DATA SELECTION AND EVENT WEIGHTING FOR ν_μ-DEUTERIUM INTERACTIONS

2.1 Introduction

To determine intranuclear scattering rates relevant to nucleon decay searches, we require at least two accelerator neutrino data sets taken with neutrino beam energy distributions approximating that of atmospheric neutrinos. The target nuclei for one data set should be of low atomic number (A), preferably hydrogen or deuterium, to calibrate event rates without the effects of intranuclear rescattering, while the target nuclei of the second data set need be of distinctly higher A. The bubble chamber data used for this Thesis, consisting of muon-neutrino interactions in deuterium and in neon (A=20), fulfill these requirements.

This chapter and Chapter 3 summarizes procedures used to ensure "clean", exclusive-channel neutrino event samples prior to intranuclear rescattering analysis for the neutrino-deuterium and neutrino-neon interactions, respectively. Weighting calculations and factors required to compensate for event removal processes are described and tabulated. An

overview of the data reduction analysis for the ν_μ-D events is presented in the following paragraphs.

The ν_μ-D data consists of 3359 events with 4261 successful fits to exclusive channel ν_μ-D hypotheses. The data was originally obtained and processed by collaborating groups from consisting of Argonne National Laboratory, Carnegie-Mellon, Kansas, and Purdue (the E-412 collaboration). The neutrino-deuterium events were recorded in wide-band horn-focussed exposures of ANL's 12-foot diameter bubble chamber with a liquid deuterium fill to the muon-neutrino beam at the Zero Gradient Synchrotron. All measured events were reconstructed using a modified version of the Three View Geometry Program (TVGP) and were kinematically fitted to a comprehensive list of neutrino and neutral hadron interactions with deuterons. The list of fit hypotheses is given in Appendix A of the Thesis.

The topological efficiencies for scanning and measuring the film are compiled in Section 2.2. The initial event sample is defined by imposing restrictions on the fiducial volume and on the beam energy as described in Section 2.3 and 2.4. The fits which pass these requirements are subsequently compared with sketches and scan-table information compiled in a physicist edit of the film. Events which failed to yield any fits to charged current reaction hypotheses are removed. Fit hypotheses which were incompatible with scan-table information or which involved reduced fit constraints were also rejected, as documented in Section 2.5 and 2.6. Evidence is found for faking of neutrino fits by topologies induced by

charged pions and muons emerging from the walls of the bubble chamber. Through the use of edit information and production angle analysis, these events are removed. The criteria for event rejection and for defining corrective weights are detailed in Section 2.7. To remove residual contamination from non-neutrino events in the data sample, final state fit hypotheses with zero constraints are compared to three-constraint final final states having similar kinematics. These comparisons, together with the kinematical selections which they motivate, are described in Section 2.8. The E-412 data is then compared on a channel-by-channel basis with a similar earlier, published ANL experiment (E-234) to compute topology-dependent processing weights. This analysis is presented in Section 2.9. Results of all ν_μ-D event selections and weighting procedures are presented in Section 2.10. Isolation of two ν_e quasi-elastic events is discussed in Section 2.11. Section 2.12 summarizes the Chapter.

2.2 Data Scanning and Processing Efficiencies

The deuterium bubble chamber film was scanned twice to locate all events prior to processing. Table 2-1 presents the combined efficiencies for the E-412 experiment. The efficiencies associated with measuring the events are given in Table 2-2. These efficiencies are taken from the analysis of reference 1 and are based upon the Geiger-Werner coincidence method[2] for combining efficiencies from two scans.

TABLE 2-1

E-412 DATA SCANNING EFFICIENCY

Observed

Topology	1-prong	2-prongs	3-prongs	4 or more prongs
Efficiency	95.7 ± 0.5	97.2 ± 0.2	99.2 ± 0.2	99.8 ± 0.2

TABLE 2-2

E-412 DATA PROCESSING EFFICIENCIES

Topology	1-prong	2-prongs	3-prongs	4 or more prongs
Efficiency	99.2 ± 2.5	95.0 ± 4.0	94.7 ± 5.0	79.0 ± 16.0

2.3 Interaction Fiducial Volume Requirement

In the analysis presented here, the 11.1 m^3 fiducial volume employed in previous E-412 data studies[1] is further reduced to 9.0 m^3 to assure that charged tracks have lengths sufficient for reliable reconstruction and scan-table editing work. The fiducial volume is defined by:

$$70.0 \text{ cm} < z < 210.0 \text{ cm} \quad (219.3)$$

$$(x^2+y^2)^{1/2} = R < 160.0 \text{ cm} \quad (172.0) \qquad (2\text{-}1)$$

$$z_c = -0.259R + 210.0 \text{ cm} \quad (219.3)$$

$$z < z_c.$$

The parenthetical values indicate previous E-412 parameters.

Gamma converting plates were installed in the chamber during later exposures of the experiment. In these later exposures, the fiducial region between the plates was eliminated by requiring:

$$-0.136z + 62.579 > x > 0.305z + 74.243; \qquad (2\text{-}2)$$

thereby further reducing the interaction volume. Equations 2-1 and 2-2 define a fiducial volume of 6.74 m^3 (compared with 8.64 m^3 in previous E-412 analyses). The reduced fiducial volumes are shown in Figure 2-1 and are indicated in dotted outline in comparison with the previously used volume. The current volumes correspond to a target mass of 1281 kg and 952 kg of liquid deuterium, respectively. The fiducial volume criteria removes 594 events (819 fits) from the data analysis.

FIGURE 2-1a

FIDUCIAL VOLUME WITHOUT GAMMA PLATES

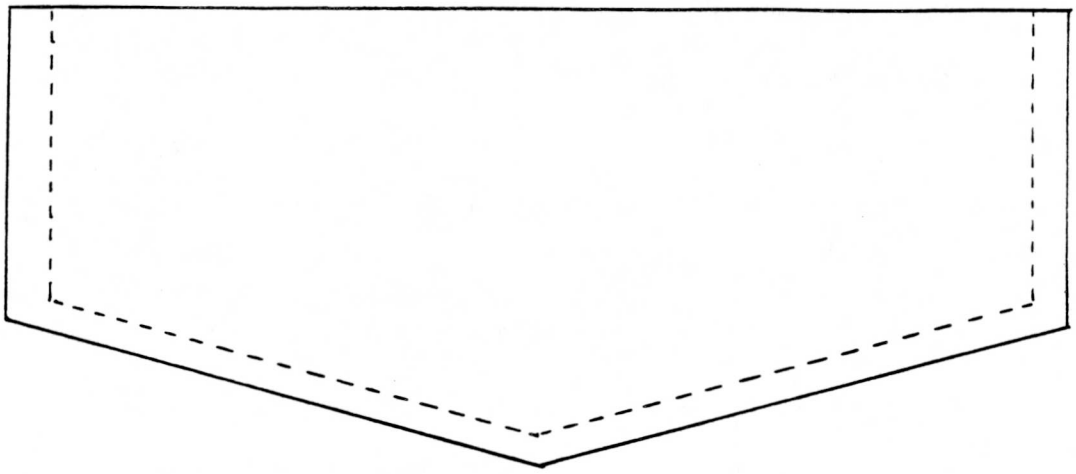

Solid Outline - Previous E-412 Analysis

Dotted Outline - Present Analysis

FIGURE 2-1b

FIDUCIAL VOLUME WITH GAMMA PLATES

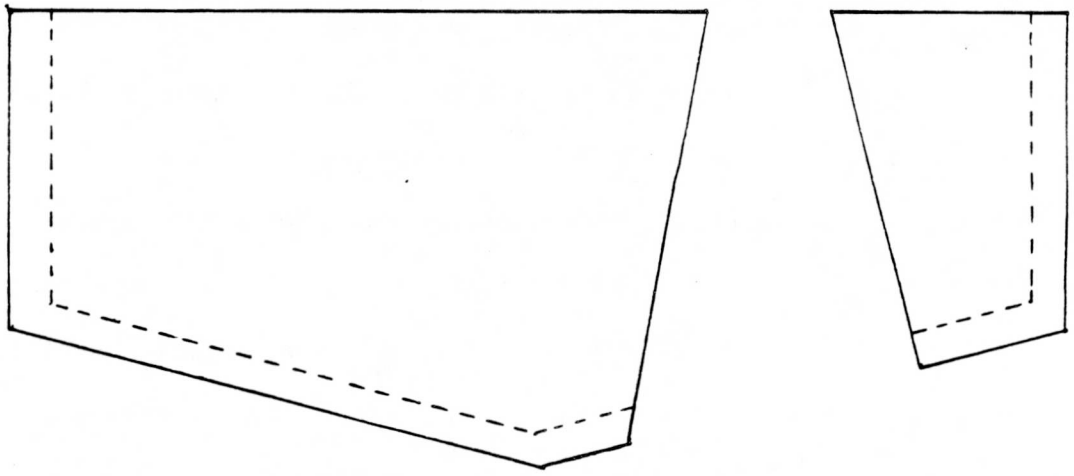

Solid Outline - Previous E-412 Analysis

Dotted Outline - Present Analysis

2.4 Fitted Beam Energy Requirement

The deuterium interaction data was recorded using the ANL 12-foot bubble chamber facility. The 12.4 GeV/c circulating protons of the Argonne Zero Gradient Synchrotron (ZGS) were extracted and focussed on a beryllium target (see Ref.3). Based on the neutrino energy distribution for observed events (shown in Figure 2-2), a maximum $E(\nu_\mu)$ cut of 6 GeV is imposed. This requirement removes 109 fits from further data analysis.

2.5 Removal of Non-Charged Current Final State Hypotheses

To remove fits which are not germane to the analysis of muon neutrino-induced charged current events, the neutral current reactions and also the neutron-induced hypotheses listed in Table 2-3 are removed from analysis. This constraint removes 176 fits from further DST analysis.

2.6 Removal of Reduced Constraint Fit Hypotheses

The ν_μ-D events were fit to neutrino hypotheses which included zero-constraint fits. Some events are consistent only with neutron-induced interactions and are rejected on this basis. Additionally, the event fitting program was allowed to reduce hypothesis constraints in order to fit poorly measured events. Since all events were eventually measured to uniform standards, reduction of the fit constraint indicates an incorrect final state hypothesis for an event. Such fits, 339 in number,

FIGURE 2-2

E-412 NEUTRINO ENERGY DISTRIBUTION

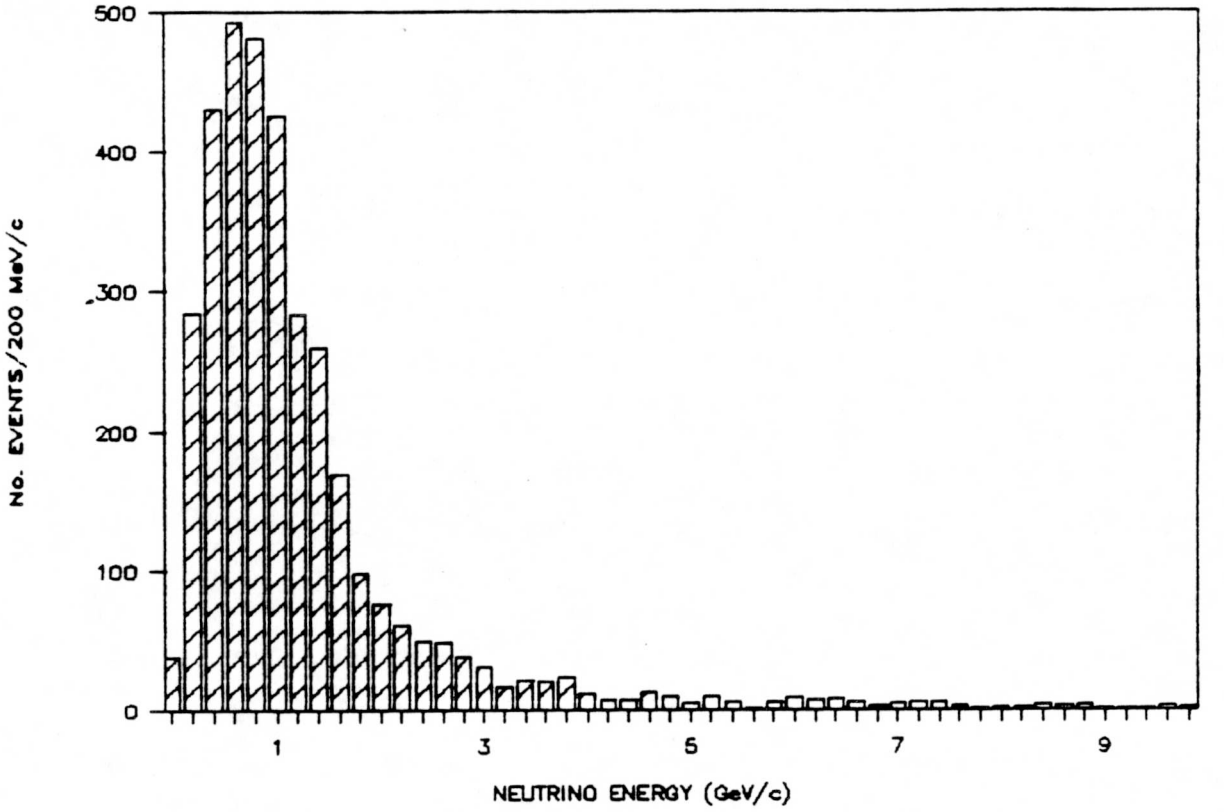

TABLE 2-3

HYPOTHESES OTHER THAN
MUON-NEUTRINO CHARGED CURRENT REACTIONS

Hypothesis
$\nu d \rightarrow \nu p n_s$
$\nu d \rightarrow \nu \pi^- p p_s$
$\nu d \rightarrow \mu^+ \pi^+ p_s$
$\nu d \rightarrow e \pi^- \pi^+ p p_s$
$\nu d \rightarrow e p p_s$
$\gamma d \rightarrow \pi^- p p_s$
$nd \rightarrow \pi^- \pi^+ p n_s$
$nd \rightarrow \pi^- p p n_s$
$nd \rightarrow \pi^- \pi^\circ p p n_s$
$nd \rightarrow \pi^- \pi^+ p n n_s$
$nd \rightarrow \pi^- p p n_s$

are removed from further analysis. Table 2-4 lists the final state hypotheses which removed by these requirements.

2.7 Incorporation of Physicist Edit Information

All measured events were examined on a scan table by a physicist; the events were sketched and compared to geometrically reconstructed and kinematically fitted information on a track-by-track basis. The edit results serve to resolve many events which fit to several final state hypotheses, as well as to eliminate many "events" as interactions of incoming charged hadrons ($\pi^{\pm}$, p's) or as topologies arising from cosmic ray or beam-associated muons.

$\nu d \rightarrow \mu^- \pi^+ n p_s$ Fits

Specific procedures were developed to handle contamination problems peculiar to individual channels. Events fitted to the zero-constraint reaction

$$\nu d \rightarrow \mu^- \pi^+ n p_s \qquad (2\text{-}3)$$

were examined to eliminate contamination from incoming charged pions as depicted in Figure 2-3. This contamination is removed by examining the opening angle, θ, between the fitted $\mu^- \text{-} \pi^+$ tracks and comparing the resultant distribution to the same opening angle in the fully constrained reaction

$$\nu d \rightarrow \mu^- \pi^+ p n_s. \qquad (2\text{-}4)$$

The $\mu^- \text{-} \pi^+$ opening angles of Equation 2-3, like those of the three-constraint Equation 2-4 fit, should be roughly isotropic, and so their cosine distributions should be flat. In comparison, charged pions incident

TABLE 2-4

UNDERCONSTRAINED AND REDUCED-CONSTRAINT FITS

Constraint	Hypothesis
2 and 1	$\nu d \rightarrow \mu^- p p_s$
1 and 0	$\nu d \rightarrow \mu^- \pi^+ p n_s$
1 and 0	$\nu d \rightarrow \mu^- K^+ p n_s$

FIGURE 2-3

TOPOLOGY OF NON-NEUTRINO EVENTS

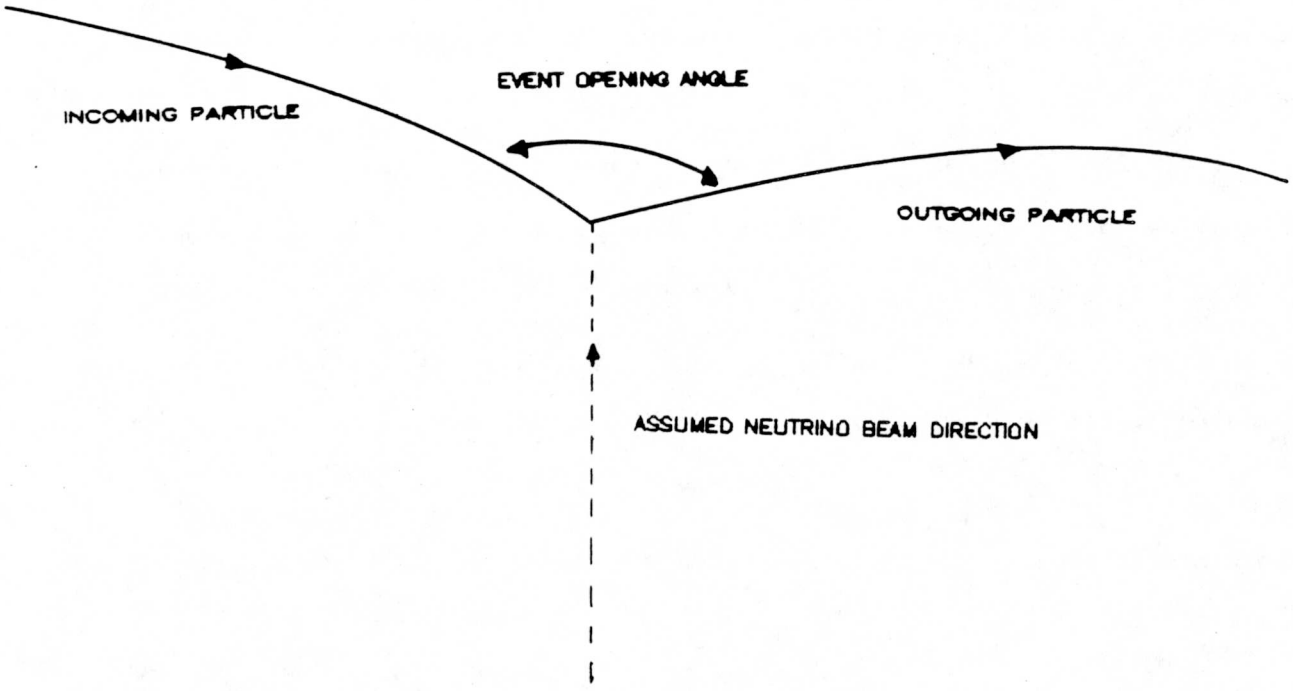

from outside the bubble chamber and scattering off the deuterons generate topologies roughly aligned in the original direction of travel. These reactions can be misinterpreted as neutrino-induced events with a wide opening angle and a $\cos\theta$ distribution strongly peaked about -1.0. Figures 2-4a) and b) illustrate the $\cos\theta$ distributions for the final state hypotheses given by Equations 2-3 and 2-4, respectively. The Figures clearly show the occurrence of non-neutrino induced contamination in the zero-constraint fit hypotheses. Based on comparison of the distributions, we regard events with $\cos\theta \leq -0.9$ to be events generated by incident pions and remove them from the candidate neutrino data set.

Having removed events in reaction channel (2-3) with $\cos\theta \leq -0.9$, some residual contamination in the region

$$-0.9 < \cos\theta < -0.5 \qquad (2\text{-}5)$$

is still suggested by Figure 2-4a). The residual contaminants, together with the "good" neutrino events which are removed by the $\cos\theta < -0.9$ cut, are compensated for by assuming a flat $\cos\theta$ distribution, by weighting upward ($w > 1$) all channel fits to account for the removed events, and by weighting downward ($w < 1$) the fits which are within the region bounded by relation (2-5). Out of a total (uncut) sample, N_T, of 648 fits, 116 fits are below $\cos\theta \leq -0.9$ (N_C), 135 fits are bounded by Equation 2-5 (N_{RC}), and 48 fits are residual non-neutrino fits (N_R). Finally, a flat $\cos\theta$ distribution produces 514 fits (N_D). Therefore, all Equation 2-3 hypothesis fits are weighted by

$$W_{1C} = N_D/(N_T - N_C - N_R)$$
$$= 1.062 \qquad (2\text{-}6)$$

FIGURE 2-4a

$\nu d \rightarrow \mu^- \pi^+ n p_s$ OPENING ANGLE COSINE DISTRIBUTION

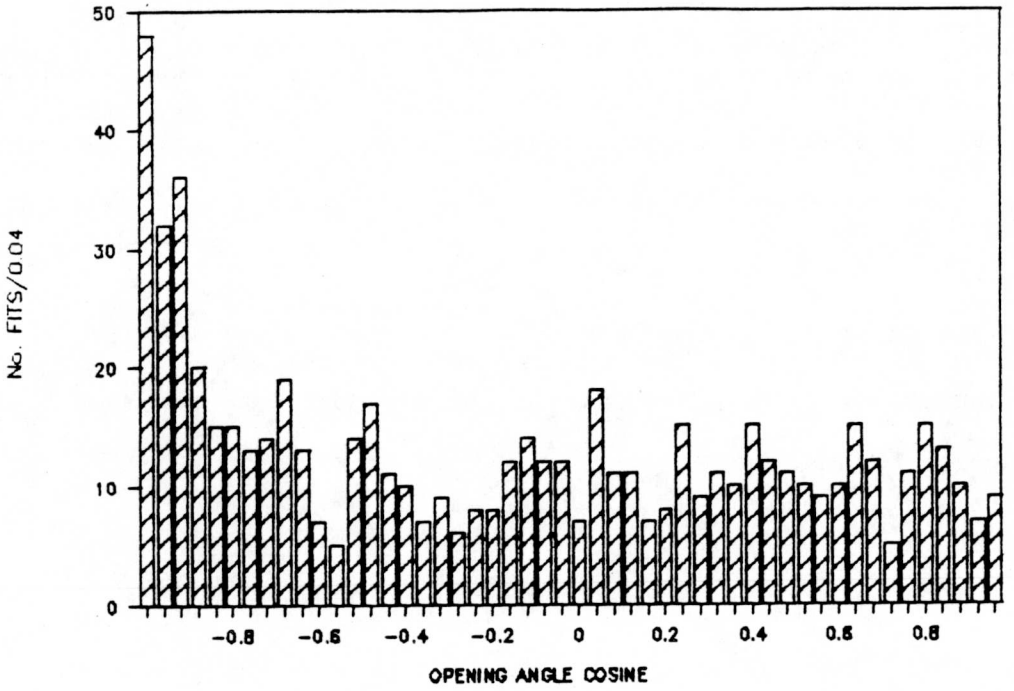

FIGURE 2-4b

$\nu d \rightarrow \mu^- \pi^+ p n_s$ OPENING ANGLE COSINE DISTRIBUTION

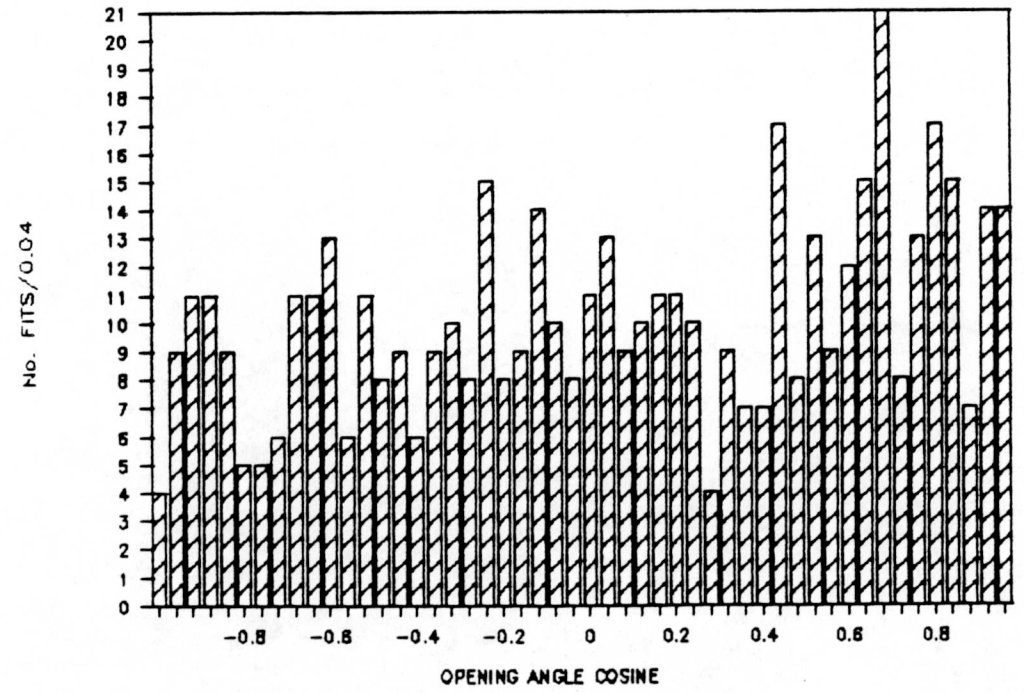

while fits with $\cos\theta < -0.5$ are additionally weighted by

$$W_{2C} = N_R/N_{RC}$$
$$= 0.355. \qquad (2\text{-}7)$$

Unedited Events

After incorporating all edit information, 23 events remain which had not been examined during the physicist scan. Of these events, eight events are fits to the reaction

$$\nu d \rightarrow \mu^- \pi^+ p n_s. \qquad (2\text{-}8)$$

While this reaction is fully constrained, six events are zero-constraint and two are two-constraint fits. In addition, one of the unexamined events is fitted to the reaction

$$\nu d \rightarrow \mu^- p p_s. \qquad (2\text{-}9)$$

with zero constraints. These nine events are removed from further analysis as reduced constraint fits.

Of the remaining unexamined events, one event is fitted to the reaction

$$\nu d \rightarrow \mu^- \pi^- \pi^+ \pi^+ n p_s \qquad (2\text{-}10)$$

one event is fitted to the reaction

$$\nu d \rightarrow \mu^- \pi^- \pi^+ p p_s \qquad (2\text{-}11)$$

one event is fitted to the reaction

$$\nu d \rightarrow \mu^- \pi^+ \pi^+ n n_s \qquad (2\text{-}12)$$

two events are fitted to the reaction

$$\nu d \rightarrow \mu^- \pi^\circ p p_s \qquad (2\text{-}13)$$

and four events are fits to

$$\nu d \rightarrow \mu^- \pi^+ n p_s. \qquad (2\text{-}14)$$

These nine events are removed from analysis and the corresponding reactions samples are weighted to correct for this event loss.

The five remaining uneditted events fit reaction hypotheses 2-13 and 2-14. A study of the edit results reveals 226 events with this ambiguity: 46 events (20.3 percent) failed both reaction hypotheses, 66 events (29.2 percent) are unresolvable (i.e., fit both reaction hypotheses), 35 events (15.5 percent) are resolved to be Equation 2-14 reactions, and 79 events (34.9 percent) are resolved to be Equation 2-13 reactions. Using these observations, the five uneditted events are removed from analysis, and the reaction hypotheses of Equations 2-13 and 2-14 are correspondingly weighted upward.

Adding up events removed by the cosθ cut together with topologies ascribed to non-neutrino events and unexamined events, there are a total of 681 fits removed from further analysis.

An examination of the opening angle for events fitted to the Equation 2-13 reaction hypothesis was conducted to check for the presence of non-neutrino induced reactions. Figure 2-5 illustrates the cosθ distribution of this analysis. No evidence exists for contamination.

2.8 Neutral Momentum Constraints

$\nu d \rightarrow \mu^- \pi^+ n p_s$ Fits

Even with the results of the edit, many events are compatible with multiple fit hypotheses, particularly with the Equation 2-14 reaction

FIGURE 2-5

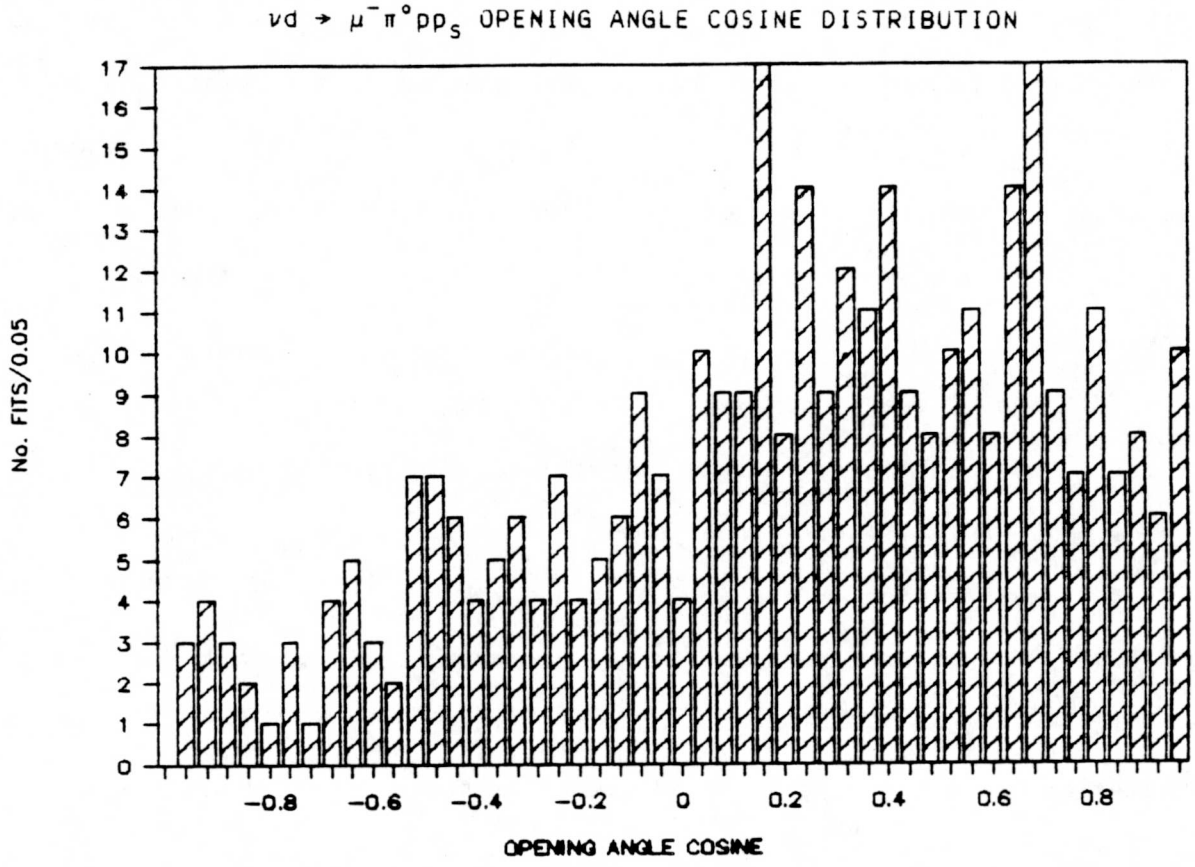
νd → μ⁻π°pp_s OPENING ANGLE COSINE DISTRIBUTION
No. FITS/0.05
0
1
2
3
4
5
6
7
8
9
10
11
12
13
14
15
16
17
-0.8
-0.6
-0.4
-0.2
0
0.2
0.4
0.6
0.8
OPENING ANGLE COSINE

hypothesis. These classes of fit hypotheses are kinematically similar to the three-constraint reaction fit

$$\nu d \rightarrow \mu^- \pi^+ p n_s . \qquad (2\text{-}15)$$

Hence, the momentum ratios R and R', defined by

$$R = |p_x(p)/p(\nu_\mu)|$$

$$R' = |p_x(n)/p(\nu_\mu)| \qquad (2\text{-}16)$$

should be similar since both ratios measure the fraction of the incident momentum imparted to the recoil baryon. Figures 2-6a) and b) show these ratios. Contamination in the zero-constraint fit can be seen in Figure 2-6a) as a peak near $R \sim 1$. This "fast-forward" neutron momentum is a result of the fitting process attempting to conserve momentum in the event. Based on this analysis, fits to the Equation 2-14 reaction hypothesis with R greater than 0.9 are weighted downward in further data analysis.

By assuming a distribution similar to the three-constraint Equation 2-16 reaction hypothesis (observed in Figure 2-6b), 12 fits are expected in the region $R > 0.9$ and 37 are observed. The resulting weight is

$$W_R = 0.324. \qquad (2\text{-}17)$$

Further scrutiny of the fast-forward neutral momentum in this reaction was conducted using the Feynman-x distribution defined by

$$x_f = Q^2/(2M_p(E_\nu - E_\mu)). \qquad (2\text{-}18)$$

It was expected that reactions exhibiting high R values would have an associated high momentum transfer. Figures 2-7a) and b) illustrate the x_f distribution for all Equation 2-16 reaction fits and for those events with $R > 0.9$, respectively. We do not observe that many of the latter events also have high x_f values, and so x_f-weighting could not be contemplated.

FIGURE 2-6a

$\nu d \rightarrow \mu^- \pi^+ n p_s$ NEUTRON/NEUTRINO MOMENTUM RATIO

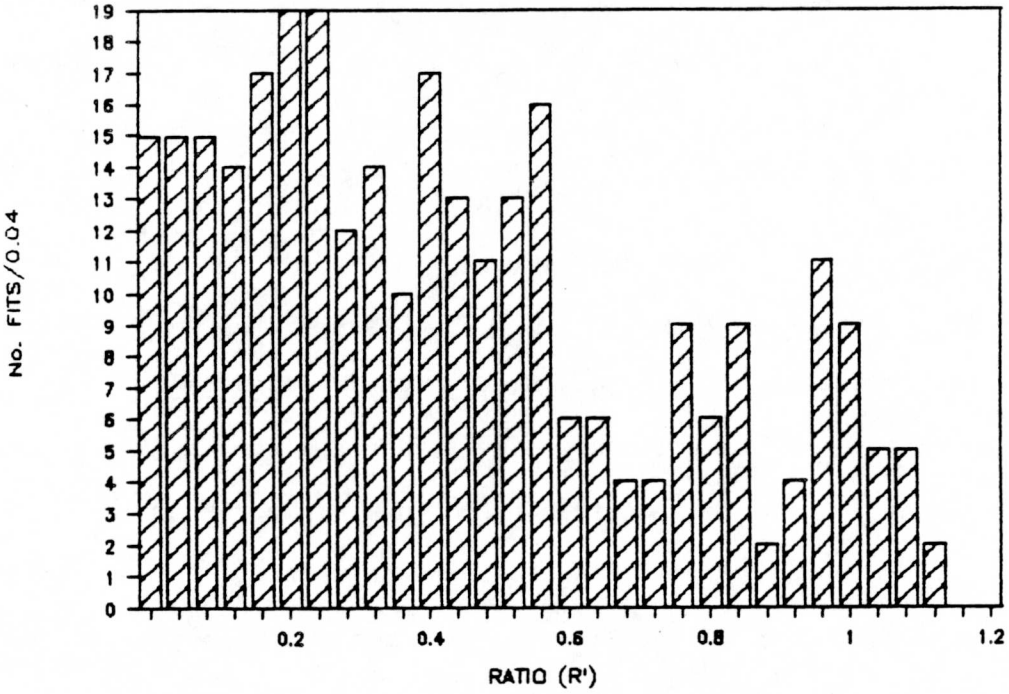

FIGURE 2-6b

$\nu d \rightarrow \mu^- \pi^+ p n_s$ PROTON/NEUTRINO MOMENTUM RATIO

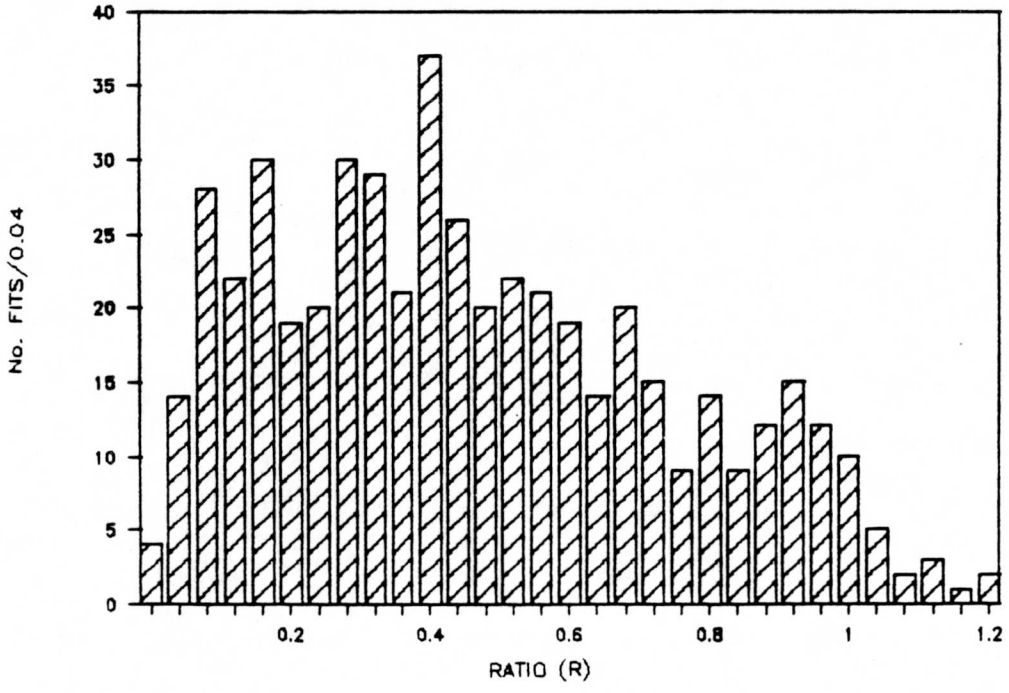

FIGURE 2-7a

$\nu d \rightarrow \mu^- \pi^+ n p_s$ FEYNMAN-X DISTRIBUTION

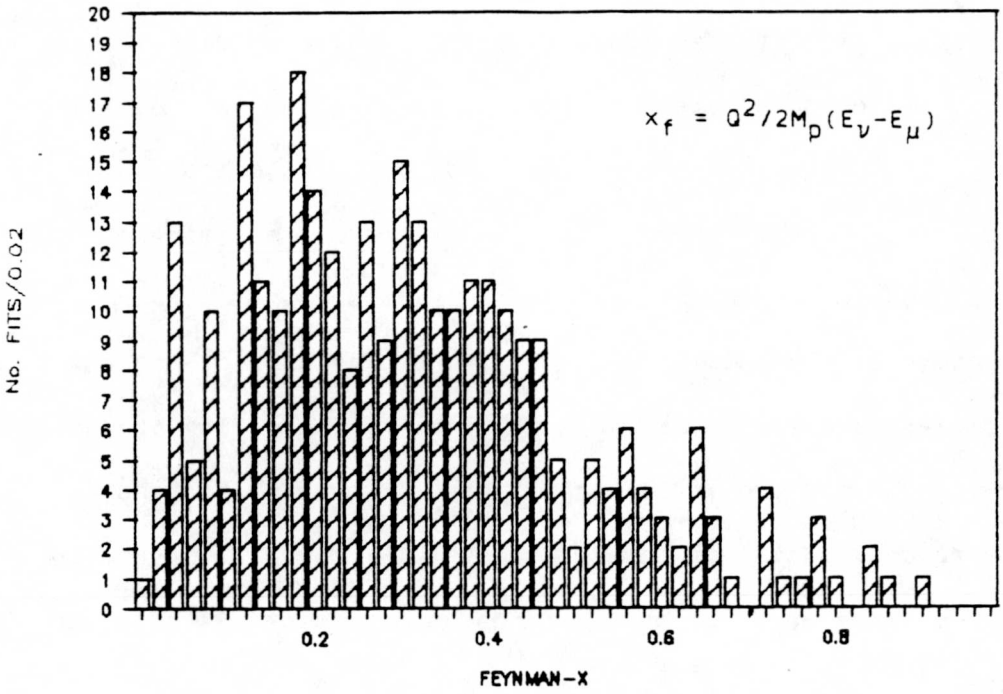

FIGURE 2-7b

$\nu d \rightarrow \mu^- \pi^+ n p_s$ R>0.9 FEYNMAN-X DISTRIBUTION

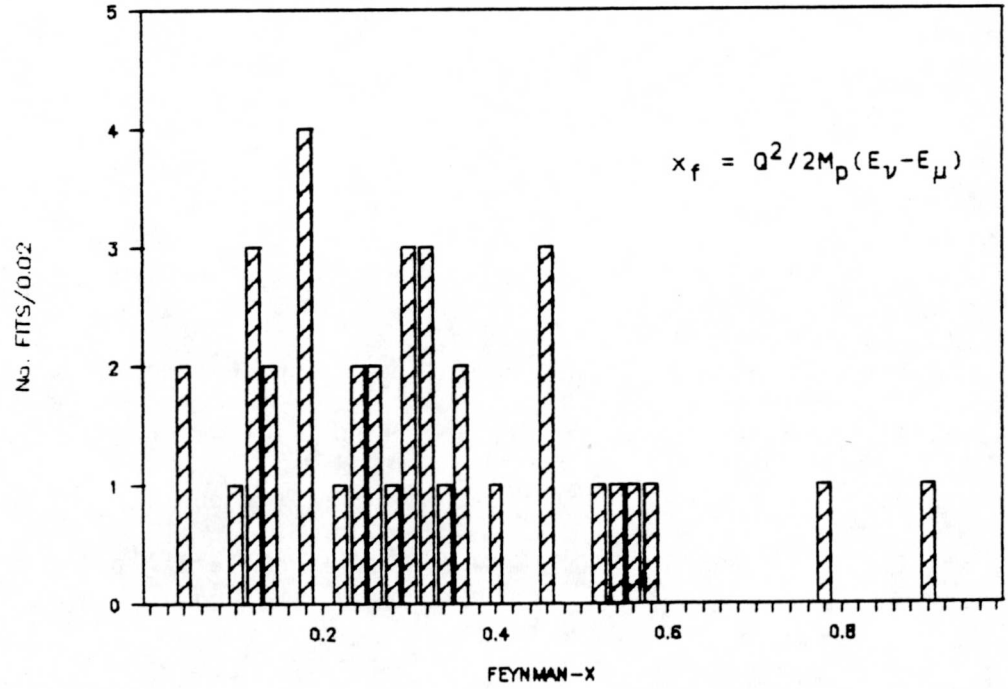

$\nu d \rightarrow \mu^- \pi^\circ pp_s$ Fits

A similar momentum ratio study was conducted on final state fits to Equation 2-13 reaction states. This analysis incorporated production pion momentum for comparison (instead of leading baryon) and the resulting distributions are shown in Figures 2-8a) and b). Similar to the neutron sample of Equation 2-14 fit hypothesis, an excess of fast-forward neutral pions is observed in the Equation 2-13 fit reaction sample. Further analysis of this channel utilized the neutrino-pion production angle, θ, for Equation 2-13 and 2-15 reaction hypotheses. Single pion production should show comparable angular distributions. Figures 2-9a) and b) illustrate the $\cos\theta$ distributions for these two final state reactions. Considerable difference is observed in the neutral pion distribution (Figure 2-9a) at $\cos\theta = 1$. Assuming a distribution shape as in Figure 2-9b), 15 events are expected in the region $\cos\theta > 0.98$ in Figure 2-9b), and 58 are observed. Thus, fits to Equation 2-13 reaction fits within this region are weighted by

$$W_G = 0.259. \qquad (2\text{-}19)$$

2.9 Final Processing Weights

In Tables 2-1 and 2-2, we have compiled the scanning, measureing, and processing efficiencies for the E-412 experiment. However, we have reservations concerning the verity of these efficiencies due to the fact that different exclusive channel analyses were given differing priorities at

FIGURE 2-8a

$\nu d \rightarrow \mu^- \pi^0 p p_s$ NEUTRAL PION/NEUTRINO MOMENTUM RATIO

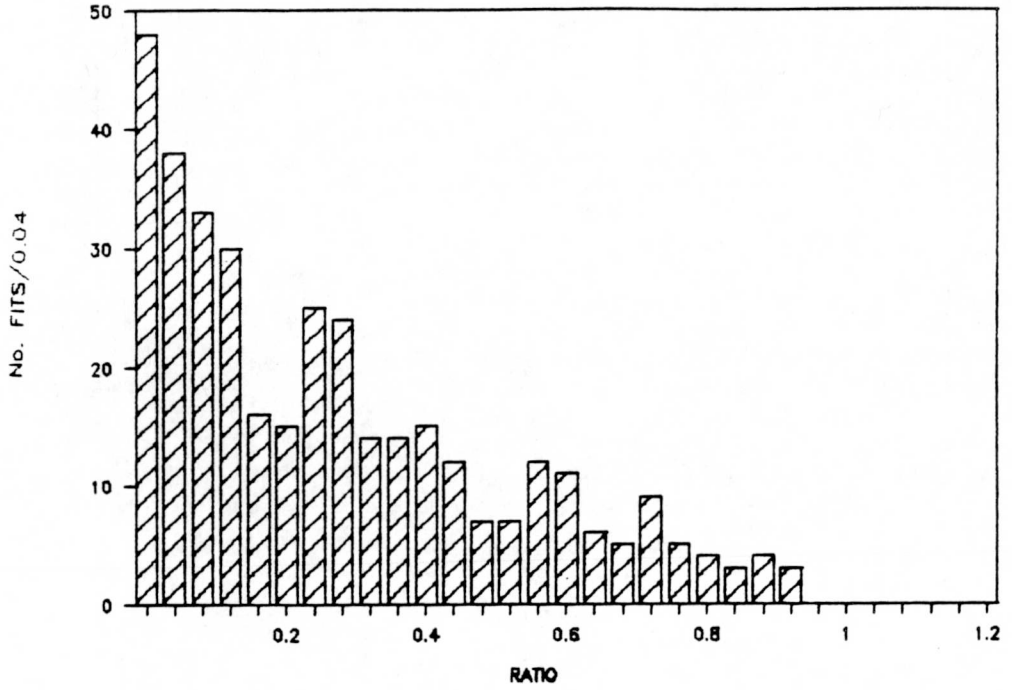

FIGURE 2-8b

$\nu d \rightarrow \mu^- \pi^+ p n_s$ POSITIVE PION/NEUTRINO MOMENTUM RATIO

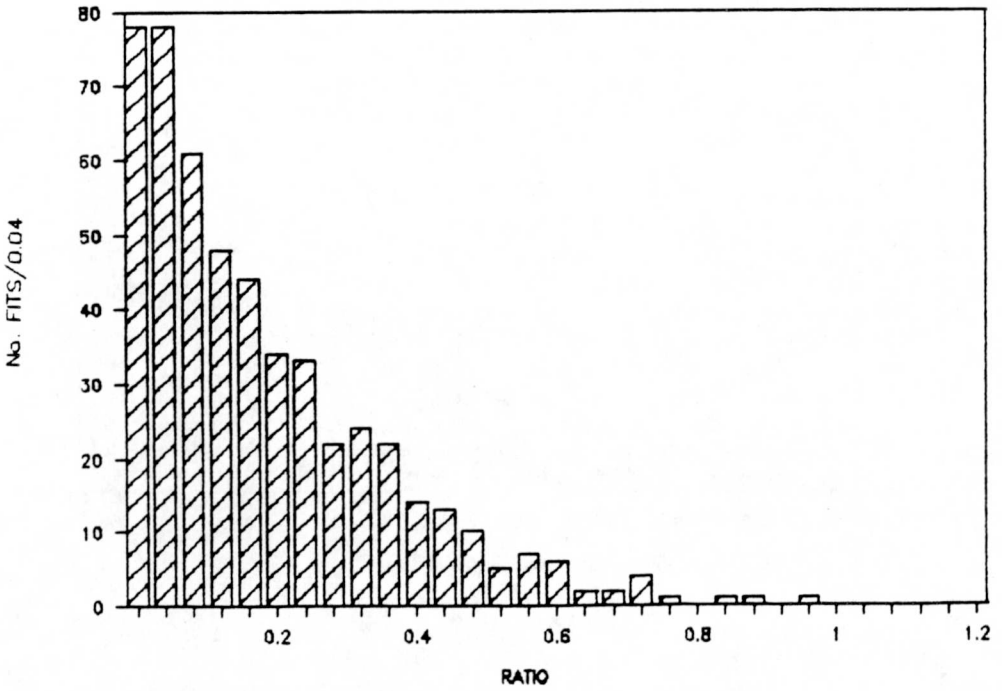

FIGURE 2-9a

$\nu d \rightarrow \mu^- \pi^0 p p_s$ NEUTRAL PION - NEUTRINO ANGLE COSINE DISTRIBUTION

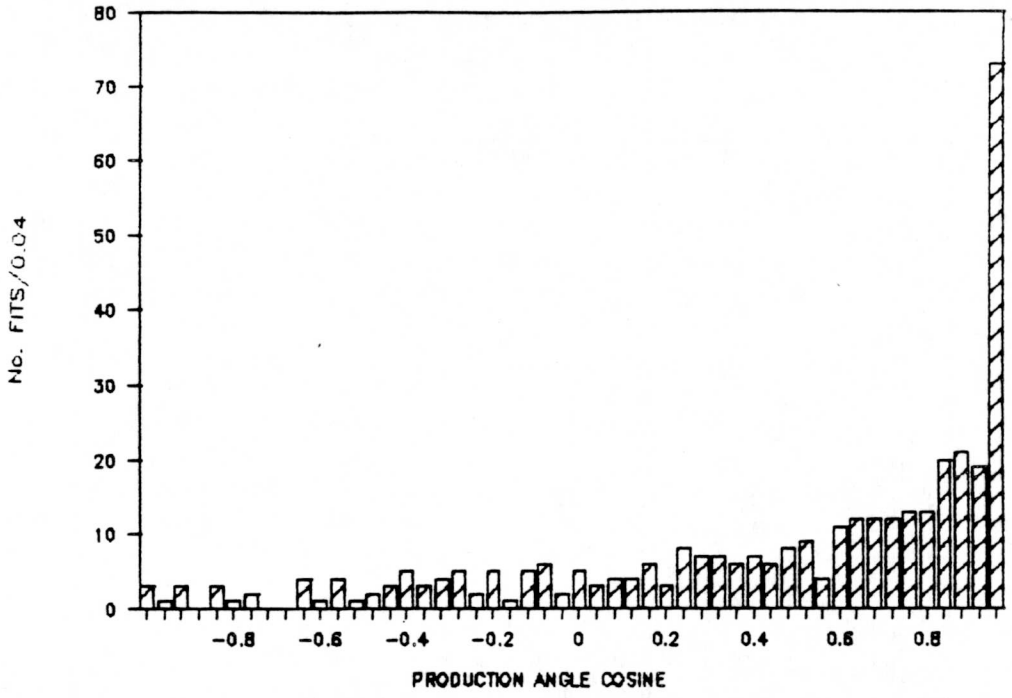

FIGURE 2-9b

$\nu d \rightarrow \mu^- \pi^+ p n_s$ POSITIVE PION - NEUTRINO ANGLE COSINE DISTRIBUTION

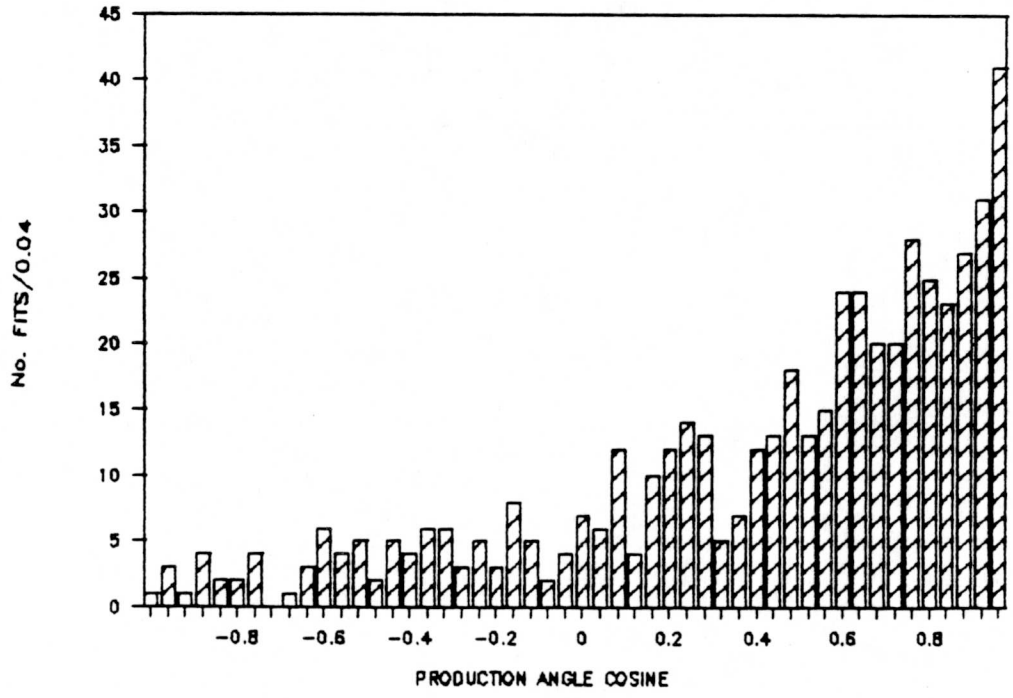

four participating institutions. Consequently, correction of the deuterium data for scanning, measuring, and processing is performed by comparing the E-412 data with results from experiment E-234 published by an ANL and Purdue University collaboration. The earlier E-234 experiment used a single-horn neutrino beam incident on deuterium at the same energy as E-412. Although the flux spectrum between the single- and double-horn exposures differs, the shape variation is minor and is neglected in the current analysis.

Exclusive channel results from E-234 were carefully corrected for processing inefficiencies and have been published[3]. To utilize the effort which went into determining the E-234 efficiencies, the weighted E-412 data is compared to the E-234 populations for sixteen reactions channels. Table 2-5 shows this comparison.

The comparison highlights some channels which were treated differently in the two experiments. Two such reactions are $\nu n \rightarrow \mu^- (k\pi^\circ) p$ and $\nu n \rightarrow \mu^- \pi^+ (\ell\pi^\circ) n$, listed in Table 2-5 as reactions 10 and 11, respectively. These E-234 exclusive channels were included in the E-412 reactions $\nu n \rightarrow \mu^- \pi^\circ p$ and $\nu n \rightarrow \mu^- \pi^+ n$, listed in Table 2-5 as reactions 8 and 9, respectively.

In addition, the reaction

$$\nu p \rightarrow \mu^- \pi^+ \pi^+ (m\pi^\circ) n, \; m \geq 0 \qquad (2\text{-}20)$$

can be considered underconstrained if neutral pions are included. The E-412 deuterium data set was only fit to the zero-constrained $\nu p \rightarrow \mu^- \pi^+ \pi^+ n$. To estimate the contribution from the Equation 2-21 reaction channel to the E-412 data, 2/3 of the reaction channel is assumed to be zero-constraint fits, that is, double-pion final state consistent with the E-412 event

TABLE 2-5

DEUTERIUM DATA EXCLUSIVE CHANNEL EVENT COMPARISONS

No.	Reaction	E-234 Data	E-412 Data Raw	E-412 Data Weighted*
1	$\nu p \rightarrow \mu^- \pi^+ p$	308	373	400
2	$\nu p \rightarrow \mu^- \pi^+ (\ell\pi^\circ) p$, $\ell \geq 1$	20	20	22
3	$\nu p \rightarrow \mu^- \pi^+ \pi^+ (m\pi^\circ) n$, $m \geq 0$	15	14	16
4	$\nu p \rightarrow \mu^- \pi^- \pi^+ p$	10	3	4
5	$\nu p \rightarrow \mu^- \pi^- \pi^+ \pi^+ \pi^\circ p$	0	0	0
6	$\nu p \rightarrow \mu^- \pi^- \pi^+ \pi^+ \pi^+ n$	0	0	0
7	$\nu n \rightarrow \mu^- p$	833	1013	1092
8	$\nu n \rightarrow \mu^- \pi^\circ p$	124	160	164
9	$\nu n \rightarrow \mu^- \pi^+ n$	90	201	209
10	$\nu n \rightarrow \mu^- (k\pi^\circ) p$, $k \geq 2$	31	0	0
11	$\nu n \rightarrow \mu^- \pi^+ (\ell\pi^\circ) p$	29	0	0
12	$\nu n \rightarrow \mu^- \pi^- \pi^+ p$	20	31	42
13	$\nu n \rightarrow \mu^- \pi^- \pi^+ (\ell\pi^\circ) p$	8	3	3
14	$\nu n \rightarrow \mu^- \pi^- \pi^+ \pi^+ (m\pi^\circ) n$	3	3	5
15	$\nu n \rightarrow \mu^- \pi^- \pi^- \pi^+ \pi^+ p$	0	0	0
16	$\nu N \rightarrow \mu^-$ + Strange	13	5	5

*Scanning, measuring, and editting weights applied.

fitting procedures. The remainder of the reaction population is considered to be unconstrained fits to three-pion final states. These ratios are obtained by the Equation 2-21 reaction channel to the kinematically similar reactions $\nu n \rightarrow \mu^- \pi^- \pi^+ p$ and $\nu n \rightarrow \mu^- \pi^- \pi^+ (\ell \pi^o) p$, listed in Table 2-5 as reaction number 12 and 13, respectively.

Having made these adjustments for experimental differences, the two data sets are grouped according to the number of final state pions. The first group of no final state pions consist of quasi-elastic events (reaction number 7). The five single-pion final state channels constitute the second group (reaction numbers 1, 8+10, and 9+11). The third group consists of double-pion final states and is composed of reaction numbers 2, 12, and 2/3 of 3. The multi-pion ($\geq$3 π's) final state consists of 1/3 of reaction 3, and reactions 4, 13, and 14. Finally, reaction number 16 contains the contribution of charged-current neutrino interactions to strange particle final states. These five groups are used to compute the E-412 processing efficiencies based on the E-234 analysis.

2.10 Data Set Reduction and Weight Summary

Table 2-6 shows the results of the data reduction process as a function of fit criteria. A total of 1929 events passed all final state criteria and are used for data analysis. Table 2-7 presents the topology distribution for these events. The reduced data set contains a total of 1683 charged-current interactions with unambiguous final state hypotheses (which are listed in Table 2-8) and 96 charged-current interactions with

TABLE 2-6

RESULT OF DEUTERIUM DATA REDUCTION ANALYSIS

Initial number of DST fits:	4261
Number of fits outside fiducial volume:	819
Number of fits with E_ν > 6 GeV/c:	109
Number of non-charge current fits:	176
Number of reduced constraint fits:	339
Number of non-neutrino induced fits:	681
Total number of DST fits removed:	2124

TABLE 2-7

TOPOLOGY DISTRIBUTION OF PASSING DEUTERIUM EVENTS

Tracks Observed	1	2	3	4	5	6
Number of Events	2	990	872	45	18	2

TABLE 2-8

UNAMBIGUOUS FINAL STATE DEUTERIUM REACTION HYPOTHESES

Number	Constraint	Hypothesis
1008	3	$\nu d \rightarrow \mu^- p p_s$
127	0	$\nu d \rightarrow \mu^- \pi^\circ p p_s$
152	0	$\nu d \rightarrow \mu^- \pi^+ n p_s$
355	3	$\nu d \rightarrow \mu^- \pi^+ p n_s$
9	0	$\nu d \rightarrow \mu^- \pi^+ \pi^\circ p n_s$
8	0	$\nu d \rightarrow \mu^- \pi^+ \pi^+ n n_s$
1	0	$\nu d \rightarrow \mu^- K^+ p n_s$
6	3	$\nu d \rightarrow \mu^- \pi^- \pi^+ p n_s$
14	3	$\nu d \rightarrow \mu^- \pi^- \pi^+ p p_s$
1	0	$\nu d \rightarrow \mu^- \pi^- \pi^+ \pi^\circ p p_s$
2	3	$\nu d \rightarrow \mu^- \pi^- \pi^+ \pi^+ \pi^+ n p_s$

TABLE 2-9

AMBIGUOUS DEUTERIUM FINAL STATE REACTION HYPOTHESES

Number	Constraint	Hypothesis
2	3	$\nu d \rightarrow \mu^- pp_s$
66	0	$\nu d \rightarrow \mu^- \pi^\circ pp_s$
114	0	$\nu d \rightarrow \mu^- \pi^+ np_s$
18	3	$\nu d \rightarrow \mu^- \pi^+ pn_s$
8	0	$\nu d \rightarrow \mu^- \pi^+ \pi^\circ pn_s$
16	0	$\nu d \rightarrow \mu^- \pi^+ \pi^+ nn_s$
3	0	$\nu d \rightarrow \mu^- K^+ pn_s$
39	3	$\nu d \rightarrow \mu^- \pi^- \pi^+ pn_s$
3	3	$\nu d \rightarrow \mu^- \pi^- \pi^+ pp_s$

TABLE 2-10

DEUTERIUM EVENT WEIGHTS

Processing and Scanning Weights

Topology	1	2	3	4 or more
Weight	1.054	1.082	1.065	1.269

$\nu d \rightarrow \mu^- \pi^+ pn_s$ Weights

Non-neutrino Contamination:	$W_{1C} = 1.062$
Residual Contamination ($0.9 < \cos\theta < 0.5$):	$W_{2C} = 0.355$
Unexamined Events:	$W_X = 1.021$

$\nu d \rightarrow \mu^- \pi^\circ pp_s$ Weights

Non-neutrino Contamination ($\cos\gamma > 0.98$)	$W_G = 0.259$
Unexamined Events:	$W_X = 1.023$

Weights for Uneditted Events

$\nu d \rightarrow \mu^- \pi^+ \pi^+ nn_s$:	$W_X = 1.042$
$\nu d \rightarrow \mu^- \pi^+ \pi^+ pp_s$:	$W_X = 1.059$
$\nu d \rightarrow \mu^- \pi^- \pi^+ \pi^+ pn_s$:	$W_X = 1.500$

Final Processing Weights

Number of Pions	Published Data	Deuterium Data		Correction Weight
		Raw	Weighted*	
0	833	1013	1092	0.99
1	582	734	773	0.98
2	50	61	74	0.88
≥ 3	36	13	18	2.59
Strange	13	5	5	3.37

*Scanning, measuring, and editting weights applied.

unresolved multiple final state hypotheses (listed in Table 2-9). Based on these distributions, final event weights are computed and are presented in Table 2-10.

2.11 Analysis of $\nu d \rightarrow e^- p$ Events

In addition to the 1683 events listed in Table 2-9 with unambiguous fits to muon-neutrino events, four events passed all data reduction criteria and were unambiguous fits to electron-neutrino reaction hypotheses. Based on neutrino flux calculations for the ANL-ZGS neutrino beam, four ν_e-deuterium interactions seemed too many to be ascribed to ν_μ beam contamination, and initial steps were made towards a neutrino-oscillation measurement.

The bubble chamber film for these events was re-examined, with particular emphasis on obtaining further ionization and shower information on the identified leptonic track. Two of the events, which are near the perimeter of the fiducial volume, were identified by track ionizations to be beam-induced neutron interactions; these were removed from the analysis. The two remaining events are consistent with an electron neutrino reaction hypothesis, and are also consistent with the number of ν_e-events expected for the ZGS neutrino beam. At this point, the neutrino-oscillation analysis was abandoned.

2.12 Neutrino-Deuterium Data Set Summary

Having completed the ν_μ-D data reduction analysis, 1929 events remain for use as a control sample when determining the intranuclear rescattering rate in neon. Besides providing a clean sample of interactions, the analysis determined the event and processing weights and established the best fit hypothesis for 1683 events while removing many ambiguous fits from 96 other ν_μ-D charged-current interactions. Of the latter 96 events, the reduced data set contains 58 events with two compatible reaction hypotheses, 36 events with three compatible reaction hypotheses, and two events with four compatible reaction hypotheses. In all studies using exclusive neutrino reaction channels which will be presented in subsequent chapters, events having multiple hypotheses are included but weighted according to the inverse of the total number of reaction hypotheses.

The flux-weighting technique also allows us to use the high statistic, kinematically fitted ν_μ-deuterium sample to estimate relative populations of neutrino reactions induced by atmospheric neutrinos. This estimate is of particular interest to the new generation of high resolution detectors (such as Frejus, Soudan II, and ICARUS) and is presented in Appendix B. The accelerator neutrino data is used to predict the energy and final state topology distribution of charged-current events for atmospheric neutrinos per kiloton year. Although the energy region $E_\nu \sim m_N$ is dominated by the quasi-elastic channel, single- and threshold double-pion production are in evidence. The latter reactions, coupled with nuclear rescattering, are potentially worrisome to nucleon decay searches.

In analysis of neutrino interactions in underground experiments which search for astrophysical neutrino sources, the final state muon is often used to gauge the incident ν_μ direction. Appendix B also presents results that indicate that the assumption of "near" collinearity is subject to greater errors than is usually indicated in the literature.

References

1. G.M. Radecky, "Study of Single-Pion Production by the Weak Charged-Current", Ph.D. Thesis, Purdue University, 1980 (unpublished).
2. H. Geiger and A. Werner, Z. Physik 21, 187 (1924).
3. S.J. Barish et al., Phys. Lett. B66, 291 (1977).

CHAPTER 3

DATA SELECTION AND EVENT WEIGHTING FOR ν_μ-NEON INTERACTIONS

3.1 Introduction

The ν_μ-Ne data consists of 515 events obtained by the Athens-Padova-Pisa-Wisconsin Collaboration in two exposures of the BEBC bubble chamber to a low-energy neutrino beam (CERN PS 180). The experiment was optimized to search for $\nu_\mu \rightarrow \nu_e$ oscillations. The efficiencies for scanning and measuring the BEBC film are compiled in Section 3.2. The initial event sample is defined by imposing a restriction on the beam energy as described in Section 3.3. Events which pass this requirement are analyzed to determine reaction hypotheses; this analysis is described in Section 3.4. Results of the event selection and weighting procedures for the ν_μ-Ne data are presented in Section 3.5.

3.2 Event Scanning and Processing Efficiencies

The neutrino-neon experiment consisted of the Big European Bubble Chamber (BEBC) filled with a Ne/H_2 mixture (about 72 percent Ne/H_2) with a set of cylindrically-symmetric proportional wire chambers (the Internal Picket Fence or IPF) surrounding of the chamber to provide timing information on leaving tracks. The candidate neutrino-neon events were collected in two visual scans of the film and a third independent scan of the frames tagged by the IPF. All events were repeatedly measured to ensure high processing efficiency. The combined scanning and measuring efficiencies for the neon data are listed in Table 3-1.

3.3 Beam Energy Requirement

The neutrino-neon interactions were obtained using the CERN PS facility with 19.2 GeV/c protons incident upon a beryllium-oxide target. Based on the neutrino energy distribution for the observed events (shown in Figure 3-1), a maximum $E(\nu_\mu)$ cut of 6 GeV is imposed. This requirement removes 25 events from further data analysis.

3.4 Event Reaction Analysis

All neutrino-neon events were examined by physicists and interaction tracks were identified by ionization, or by using scattering or decay signatures. For analysis and for purposes of comparison with the ν_μ-

TABLE 3-1

NEUTRINO-NEON DATA SCANNING AND
PROCESSING EFFICIENCIES*

Process	Efficiency	No. Events
Single visual scan	0.76	166
Double visual scan	0.95	125
Single visual scan with IPF	0.98	128
Double visual scan with IPF	0.99	96

* Efficiencies are from Reference 1.

FIGURE 3-1

NEUTRINO ENERGY DISTRIBUTION IN THE NEON DATA SET

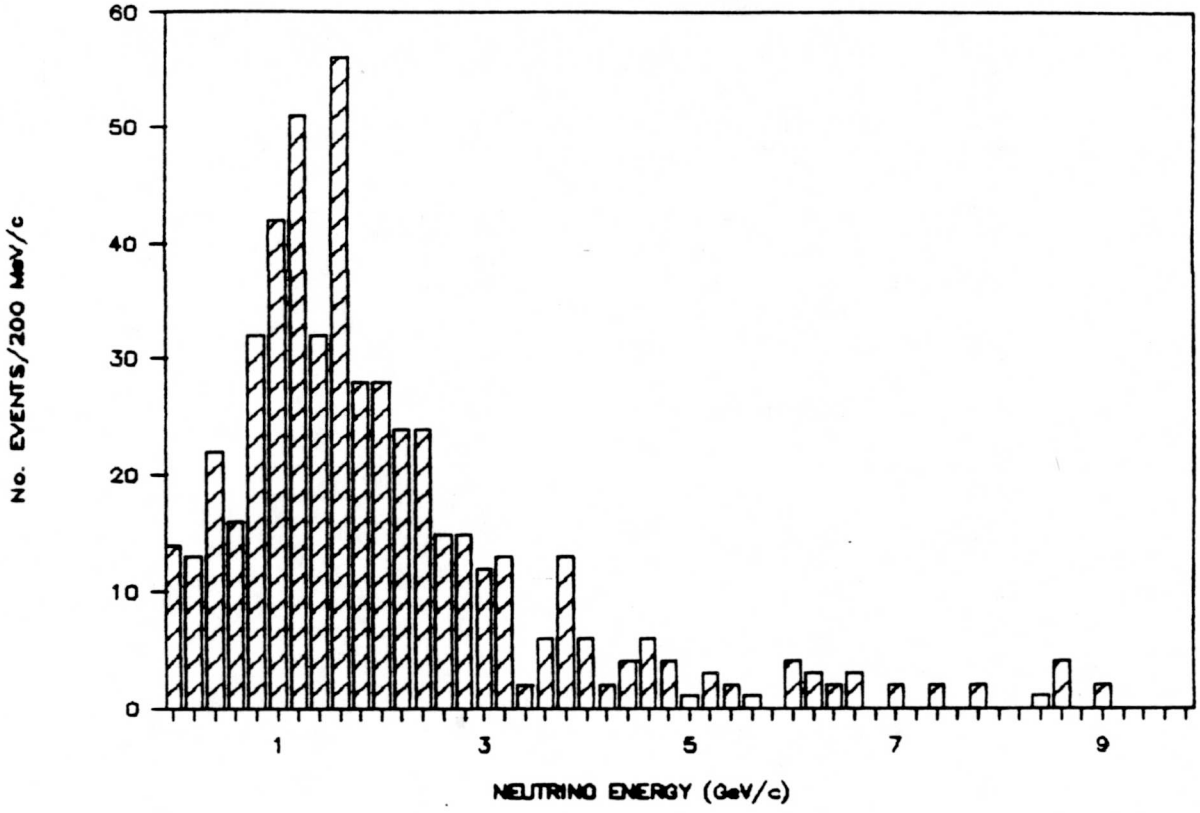

deuterium data, the events are categorized into reaction channels. The channels assignments require proper identification of spectator protons and neutral pions. The procedures for these identifications are described below.

Determination of Event Spectator Protons

Neutrino interactions with neon yield final states having spectator nucleons in addition to the final state interaction proton or neutron. In order to identify the interaction nucleon, the following criteria are imposed on the data:

a) For events containing more than one identified proton, the highest momentum proton is taken to be the interaction proton; all remaining proton tracks are then regarded to be spectator protons.

b) For events containing a single identified proton, the proton momentum is required to be greater than 200 MeV/c for the track to be regarded as an interaction proton, otherwise the track is a spectator proton.

The momentum requirement for the criterion b) is based on the observed proton momentum distribution shown in Figure 3-2. In addition, the interaction proton's momentum is required to be in the forward direction.

Determination of Neutral Pions

Figure 3-3 shows the gamma momentum distribution for the neutrino-neon interactions. Invariant mass combinations are calculated for all events containing two or more photons. The initial distribution with all gamma combinations is shown in Figure 3-4. This distribution shows that 30 photon pairs have invariant masses below 40 MeV/c^2. To check whether

FIGURE 3-2

PROTON MOMENTUM DISTRIBUTION

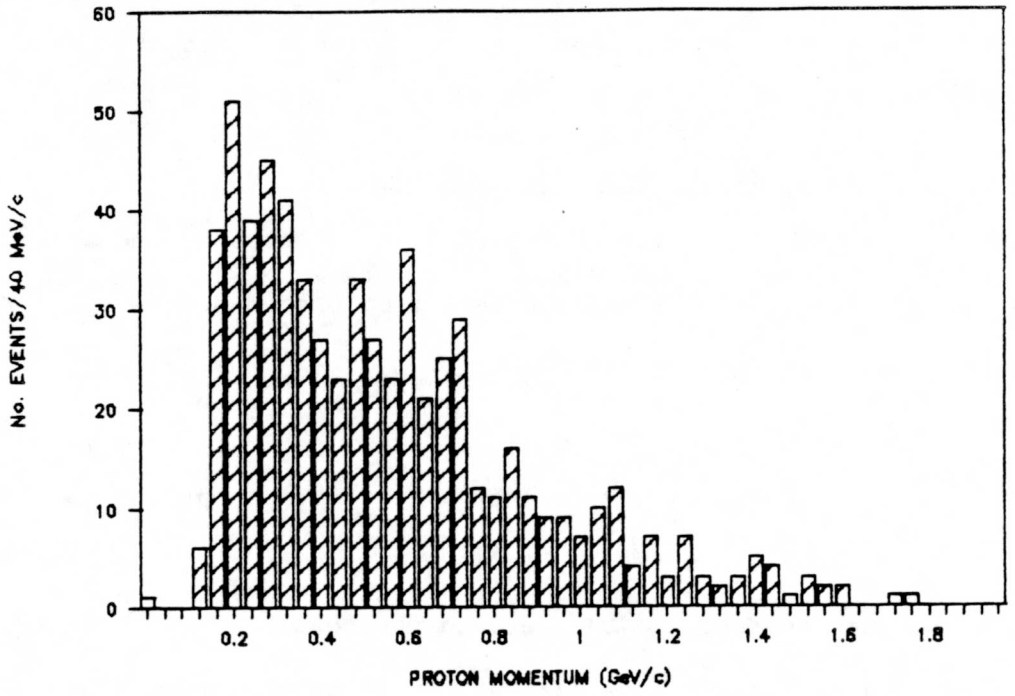

FIGURE 3-3

GAMMA MOMENTUM DISTRIBUTION

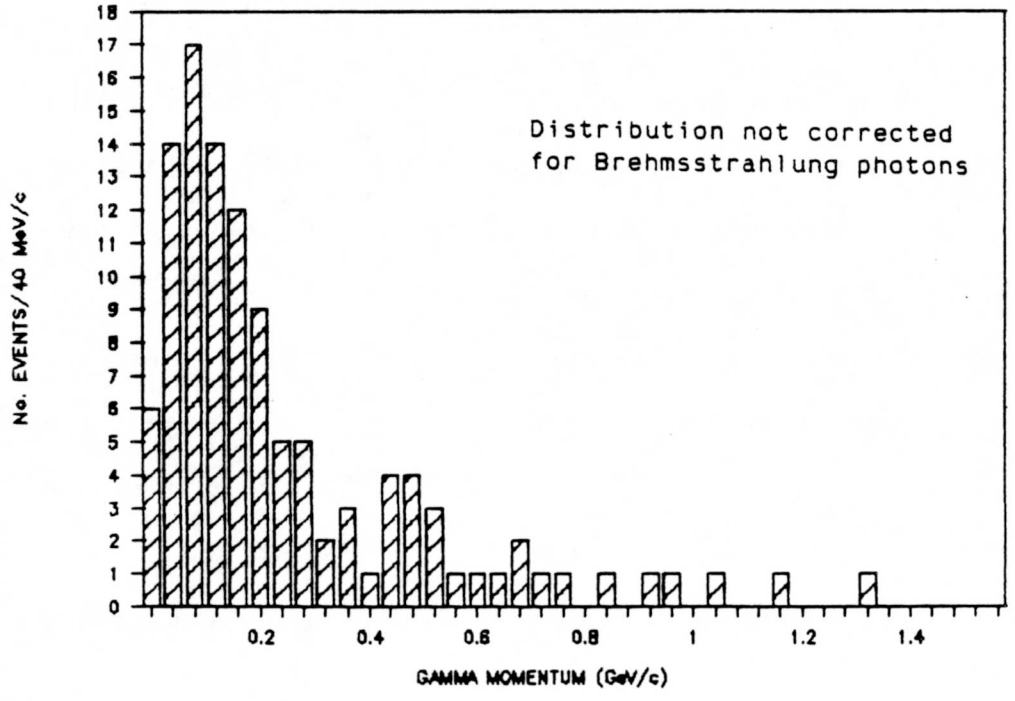

FIGURE 3-4

GAMMA-GAMMA INVARIANT MASS

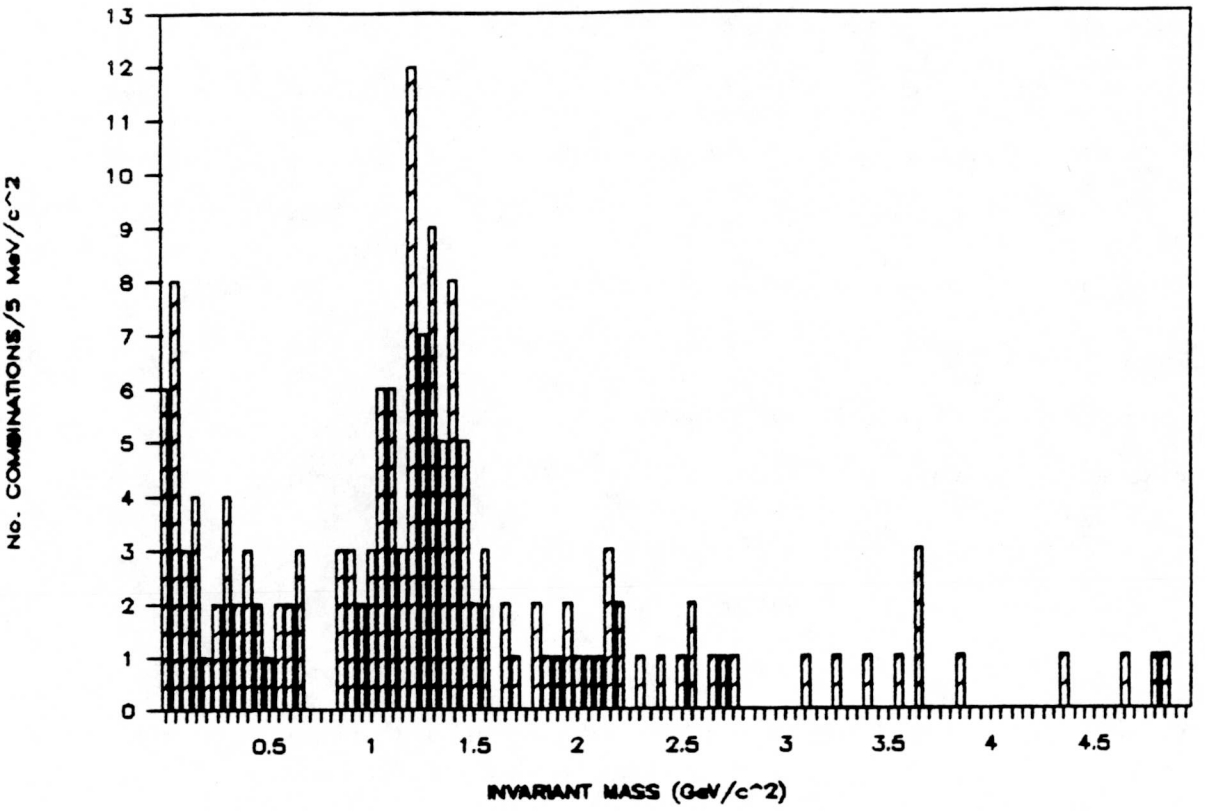

these pairs are brehmsstrahlung photons, the angle between the two gammas' line of flight, θ, is computed. Brehmsstrahlung photons should lie in a narrow forward cone with respect to the original gamma direction. Figure 3-5 shows the cosine distribution for the reconstructed low mass pairs. From this distribution, it is inferred that one photon in a gamma-gamma pair is a brehmsstrahlung photon if the invariant mass of the pair is less than 40 MeV/c^2 and if their angular separation is less than 8 degrees ($\cos\theta > 0.99$). The four-momenta of brehmsstrahlung gammas were added to their parent four-momenta to yield "effective" photons, and then all photon-photon invariant mass combinations were recomputed. In this way, all brehmsstrahlung gammas were removed from the pairing procedure while their energies were still accounted for.

A subsequent invariant mass distribution for events with two or more photons is given in Figure 3-6. The distribution shows a π° signal at 130 MeV/c^2. There are 77 photon pairs within the mass range $80 < M(\gamma\gamma) < 160$ MeV/c^2. Of these pairs, 20 are estimated to constitute the combinatorial background.

3.5 Neon Data Set Reduction and Weight Summary

Table 3-2 shows the results of the beam energy cut and reaction analysis. Of the 490 events with E_ν less than 6 GeV, 56 do not contain a final state muon, 1 is an ν_e-interaction, and 1 is a $\bar{\nu}_\mu$-interaction. In addition, 28 events contain either negatively, or double- or triple-positively charged final states. These events, listed in Table 3-3, are

FIGURE 3-5

$M(\gamma\gamma) < 40$ MeV/c^2 COLINEARITY COSINE DISTRIBUTION

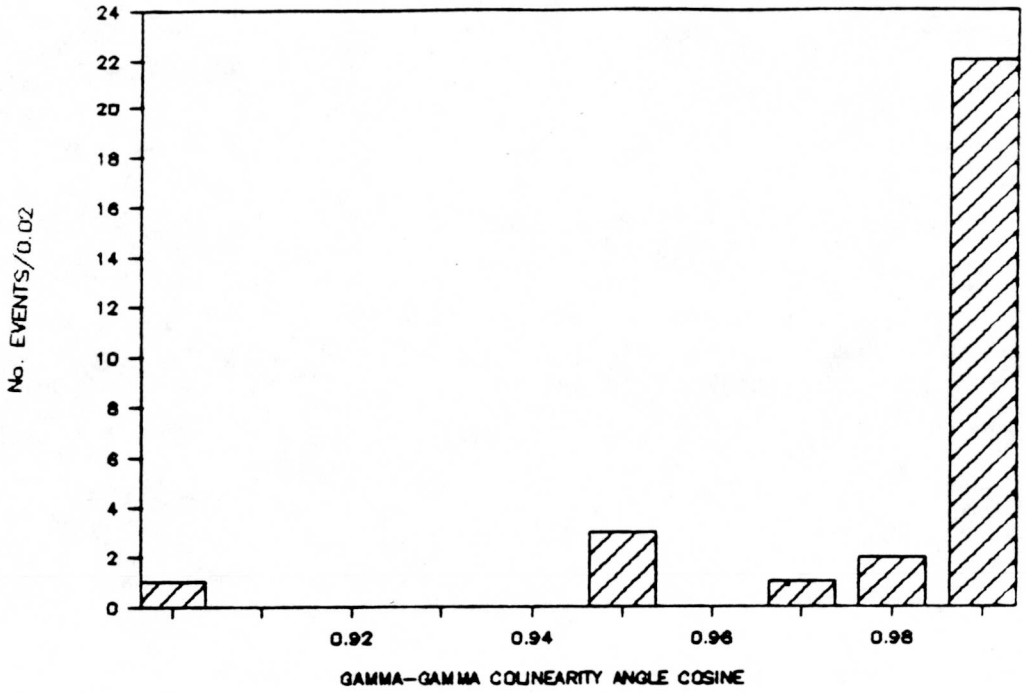

FIGURE 3-6

GAMMA-GAMMA INVARIANT MASS DISTRIBUTION

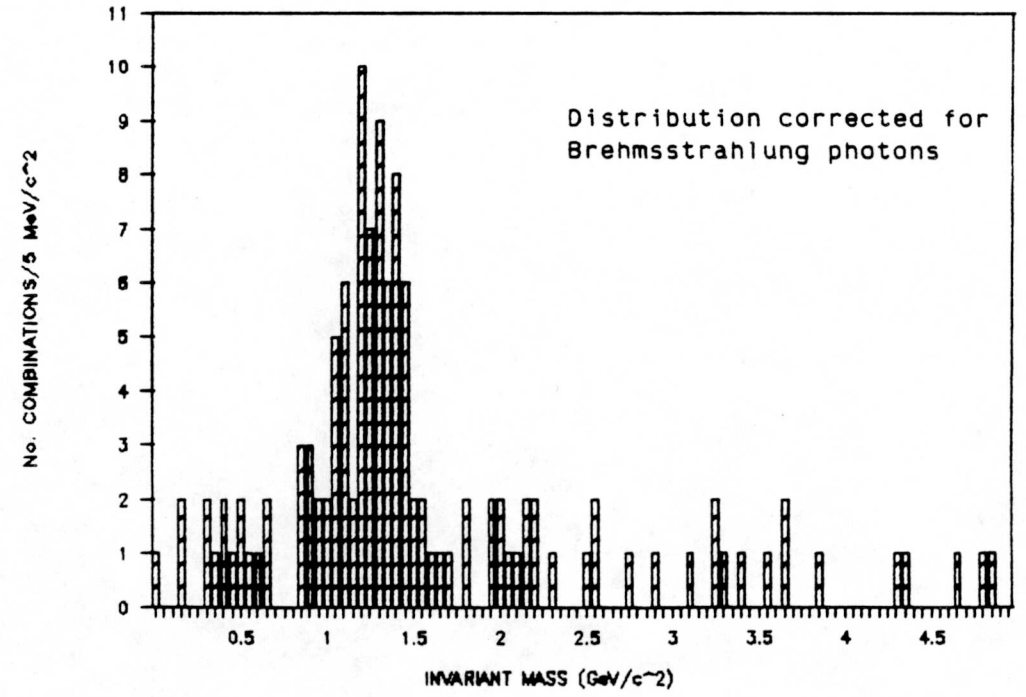

TABLE 3-2

RESULT OF DATA REDUCTION AND
REACTION ANALYSIS

Initial Number of DST Events: 515
Number of Events with E_ν > 6 GeV/c: 25
Number of Passing Events: 490

No. Events	Reaction
80	$\nu Ne \rightarrow \mu^- \pi^+ p$
17	$\nu Ne \rightarrow \mu^- \pi^+ \pi^\circ p$
3	$\nu Ne \rightarrow \mu^- \pi^- \pi^+ \pi^+ p$
4	$\nu Ne \rightarrow \mu^- \pi^- \pi^+ \pi^+ \pi^\circ p$
199	$\nu Ne \rightarrow \mu^- p$
19	$\nu Ne \rightarrow \mu^- \pi^- \pi^+ p$
11	$\nu Ne \rightarrow \mu^- \pi^- \pi^+ \pi^\circ p$
0	$\nu Ne \rightarrow \mu^- \pi^- \pi^- \pi^+ \pi^+ p$
29	$\nu Ne \rightarrow \mu^- \pi^+ n$
10	$\nu Ne \rightarrow \mu^- \pi^+ \pi^\circ n$
5	$\nu Ne \rightarrow \mu^- \pi^+ \pi^+ n$
1	$\nu Ne \rightarrow \mu^- \pi^+ \pi^+ \pi^\circ n$
0	$\nu Ne \rightarrow \mu^- \pi^- \pi^+ \pi^+ n$
0	$\nu Ne \rightarrow \mu^- \pi^- \pi^+ \pi^+ \pi^\circ n$
2	$\nu Ne \rightarrow \mu^- \pi^- \pi^+ \pi^+ \pi^+ n$
1	$\nu Ne \rightarrow \mu^- \pi^- \pi^- \pi^+ \pi^+ \pi^+ \pi^\circ p$
46	$\nu Ne \rightarrow \mu^- \pi^\circ p$
3	$\nu Ne \rightarrow \mu^-$ + strange particles
86	$\nu Ne \rightarrow$ Other

TABLE 3-3

FINAL STATES HAVING TOTAL CHARGE UNEQUAL
TO $\nu n(Q=0)$ OR $\nu p(Q=+1)$

No. Events	Reaction	Final State Charge
6	$\nu Ne \rightarrow \mu^- \pi^- p$	-1
2	$\nu Ne \rightarrow \mu^- \pi^- \pi^\circ p$	-1
4	$\nu Ne \rightarrow \mu^- \pi^+ \pi^+ p$	+2
1	$\nu Ne \rightarrow \mu^- \pi^+ \pi^+ \pi^\circ p$	+2
4	$\nu Ne \rightarrow \mu^- \pi^+ \pi^+ \pi^+ p$	+3
2	$\nu Ne \rightarrow \mu^- \pi^+ \pi^+ \pi^+ \pi^\circ p$	+3
1	$\nu Ne \rightarrow \mu^- \pi^- \pi^- \pi^+ p$	-1
1	$\nu Ne \rightarrow \mu^- \pi^- \pi^+ \pi^+ \pi^+ p$	+2
3	$\nu Ne \rightarrow \mu^- \pi^- \pi^- \pi^+ \pi^+ \pi^\circ p$	-1
1	$\nu Ne \rightarrow \mu^- \pi^- \pi^+ n$	-1
2	$\nu Ne \rightarrow \mu^- \pi^+ \pi^+ \pi^+ n$	+2

TABLE 3-4

NEON DATA PROCESSING WEIGHTS

Category	Weight
Single scan event	1.32
Double scan event	1.05
Single scan event with IPF	1.02
Double scan event with IPF	1.01

Neutral Pion Reconstruction Weight

Reconstruction weight per π° 57/77 = 0.74

direct evidence for intranuclear rescattering in neon. Table 3-4 lists the event weights associated with the neon data set.

References

1. C. Angelini et al. Phys. Lett. B179, 307 (1986).

CHAPTER 4

ENERGY NORMALIZATION WEIGHTING AND NEUTRINO FLUX WEIGHTING

4.1 Introduction

By comparing neutrino-neon to neutrino-deuterium interactions at comparable energies, one can elucidate the effects of hadronic rescattering within a spatially extended nucleus. By weighting the two data sets to match the atmospheric neutrino flux spectrum, it is possible to estimate the effects of rescattering in underground nucleon decay searches. This chapter describes weighting methods which enable interesting comparisons of the two neutrino event samples.

Two weighting schemes have been explored. The first method uses the observed neutrino energy distributions of the ν_μ-deuterium and the ν_μ-neon data to determine event weights. The method requires the event energy distributions for charged current channels to be normalized to each other and weights to be computed equal to the relative populations of events in the normalized energy distributions. For this reason, the technique is called the Energy Normalized Method, or ENM. This method is described in Section 4.2.

The ENM method permits direct comparisons for data consistency between the two neutrino event samples. It does not, however, provide the best means to examine intranuclear rescattering effects in the context of nucleon decay searches, which is the subject of this Thesis. With this latter analysis goal in mind, we have developed a second weighting technique, which utilizes the flux spectra of accelerator experiments ANL E412 and CERN PS 180 together with the flux spectrum of atmospheric neutrinos. The accelerator-induced spectra are shape-matched to the atmospheric neutrino flux spectrum to determine event weights. The energy-dependent weights are subsequently applied to events which have been corrected for detection inefficiencies. This "flux-weighting" method is described in Section 4.3. Section 4.4 summarizes the two weighting approaches.

4.2 Energy Normalization Method Event Weighting

Direct comparison of the ν_μ-deuterium and ν_μ-neon is a comparison between scattering from a relatively simple nucleus (deuterium, A=2) and from a complex and spatially extended nuclear structure (neon, A=20). The Energy Normalization Method (ENM) described in this section employs the neutrino energy distribution as observed in both data sets to compute event weights. This method would, in general, require that weights be determined separately for each exclusive reaction channel. The present analysis, however, takes all charged current events to define the inclusive reaction channel $\nu_\mu N \rightarrow \mu^- +$ Anything.

Events in both data sets are required to pass selection criteria and are weighted to correct for processing inefficiencies and data selection cuts. In addition, a minimum neutrino energy, E_ν, requirement of 400 MeV is imposed on both event samples. Figures 4-1a) and b) show the neutrino energy distributions for the deuterium and neon data sets, respectively. The deuterium energy distribution peaks at about 800 MeV with a FWHM of approximately 400 MeV. The distribution decreases rapidly with increasing energy and exhibits little fluctuation at higher energies. The neon energy distribution, shown in Figure 4-1b), peaks at about 1.4 GeV and has a FWHM of approximately 600 MeV. The distribution slowly decreases with increasing energy, but exhibits fluctuations at higher energies, reflecting the concurrence of low statistics together with inefficiency weighting. The ENM weights are computed by smoothing and normalizing both energy distributions between $0.4 < E_\nu < 6.0$ GeV. The energy dependent weights are subsequently determined by computing the deuterium to neon population ratio in 28 bins, each with width 200 MeV. To compensate for the fourfold statistical advantage of the deuterium data, the deuterium data are multiplied by 0.254.

The weighting function determined from this analysis is shown in Figure 4-2. This function, which "maps" the inclusive deuterium events into neon interactions, reflects the fact that the deuterium data has more statistics in the energy region below 2 GeV, while the neon data has more events between 3 and 5 GeV. Beyond 5 GeV, however, both data sets are statistically similar.

FIGURE 4-1a

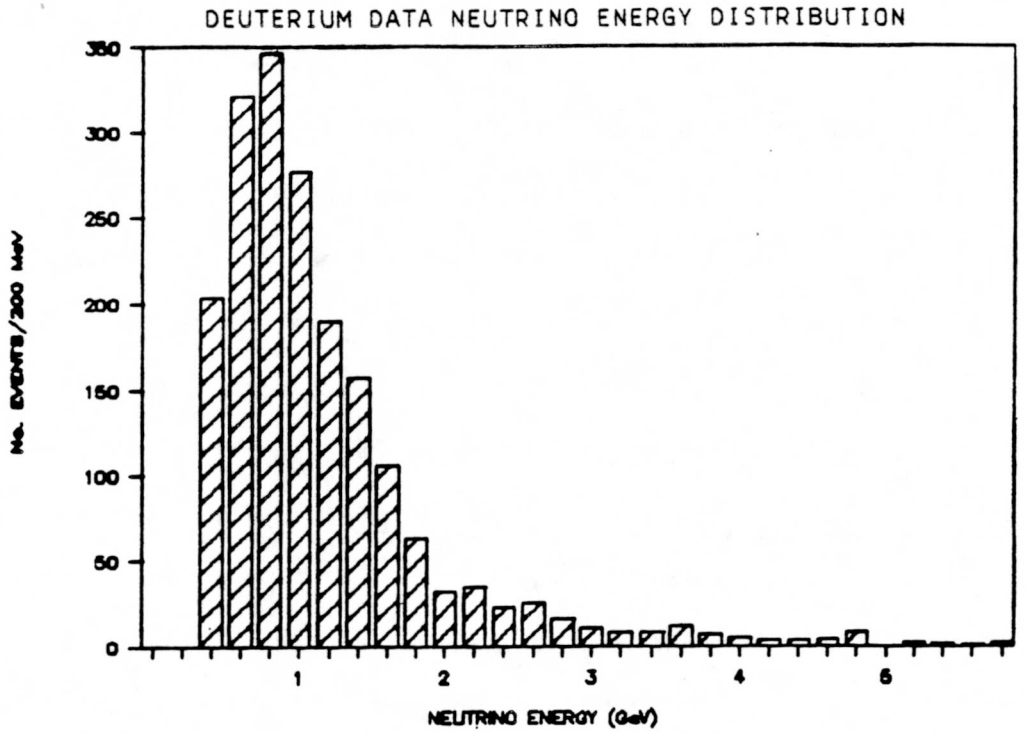

FIGURE 4-1b

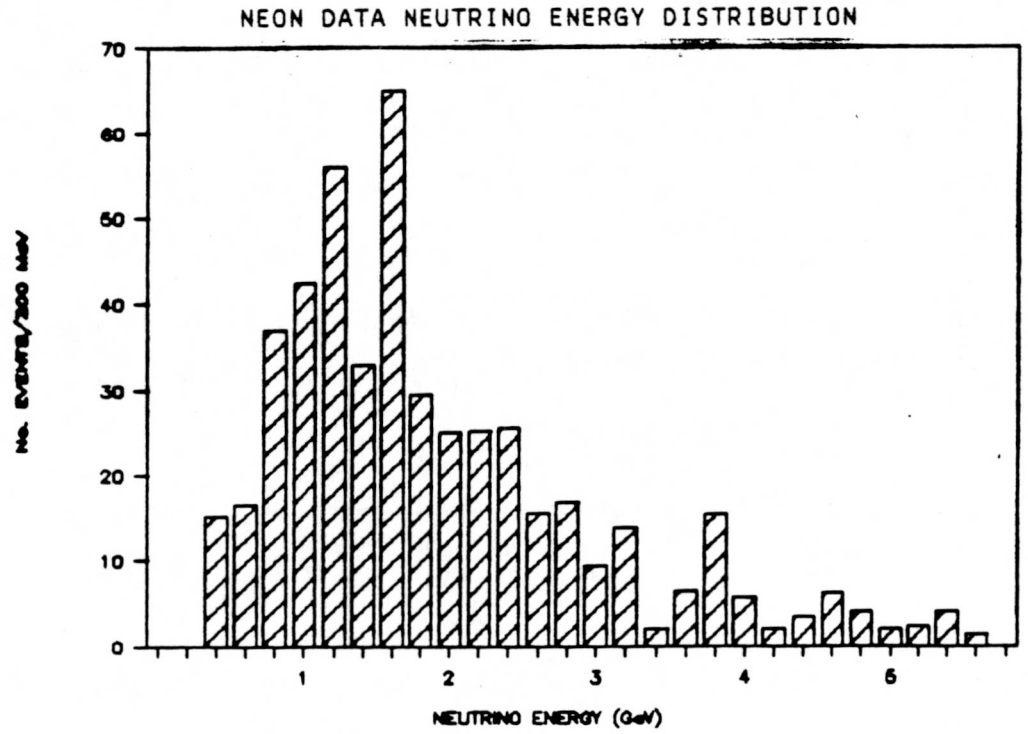

FIGURE 4-2

DEUTERIUM TO NEON ENM WEIGHT

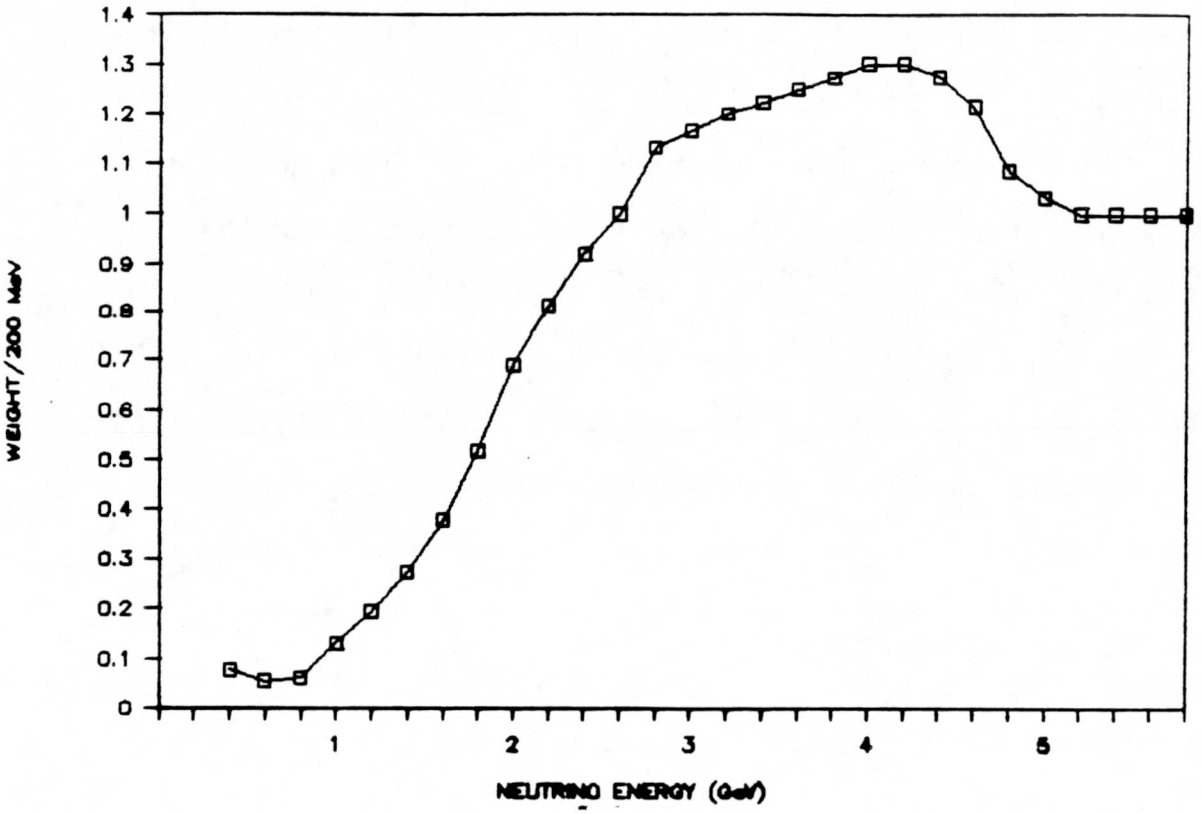

Since the ENM weight set is computed in 200 MeV bins, linear interpolation is used to compute intermediate energy weight values. The effect of the inclusive ENM weights is illustrated in Figures 4-3a) and b). The former figure shows the energy distributions of the neon and the ENM weighted deuterium data. (To allow for direct comparison, all distributions showing both data sets are area normalized.) Likewise, Figure 4-3b) shows the energy distribution of the deuterium versus the ENM weighted neon data. These distributions confirm that the smoothing and normalizing procedures of the ENM method are appropriate and have been correctly implemented.

To test the validity of ENM weighting, two target-independent quantities are used. These quantities are the momentum magnitude and production angle cosine for final-state muons. Naively, the shape of the muon momentum distribution is expected to reflect the neutrino energy distribution which produced it. Hence, the neon μ-momentum distribution is expected to be peaked at a higher energy and have a broader distribution than the deuterium muons. Figures 4-4a) and b) behave in accordance with these naive expectations. Figure 4-4a) shows the neon and the ENM weighted deuterium muon momentum distribution, peaking at 400 MeV/c. Figure 4-4b) shows the deuterium and the ENM weighted neon muon momentum distribution which peaks at 300 MeV/c. The representative errors shown in these distributions reflect statistical uncertainties.

Because of the higher neutrino energy, the muon production angle for the neon data is expected to be peaked in the forward direction; that

FIGURE 4-3a

NEON DATA NEUTRINO ENERGY DISTRIBUTION

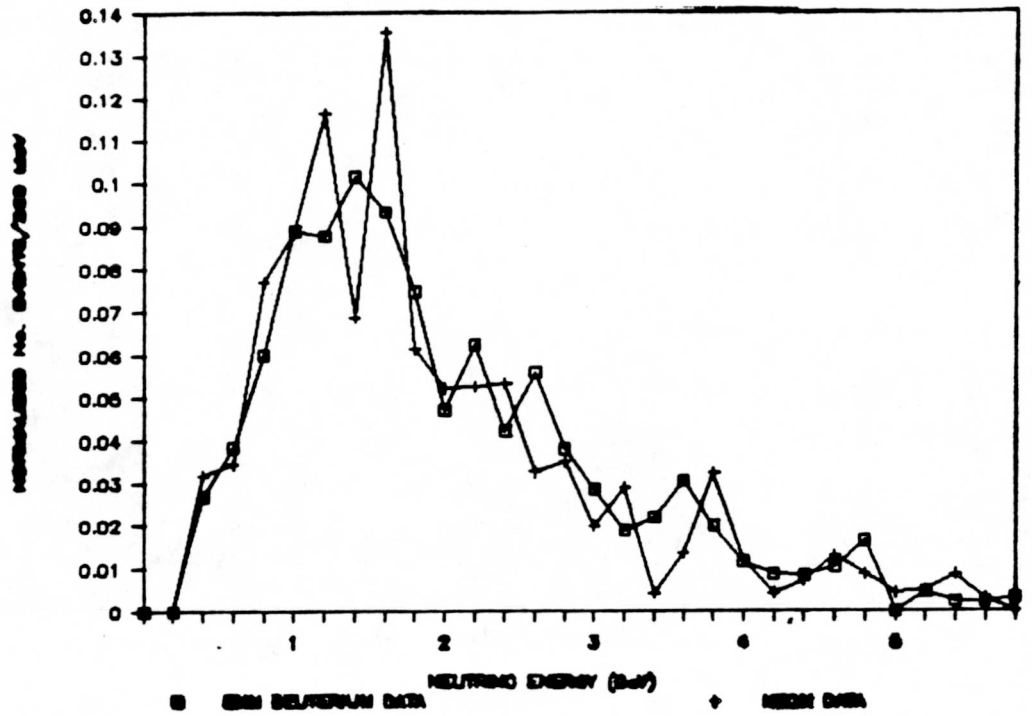

FIGURE 4-3b

DEUTRIUM DATA NEUTRINO ENERGY DISTRIBUTION

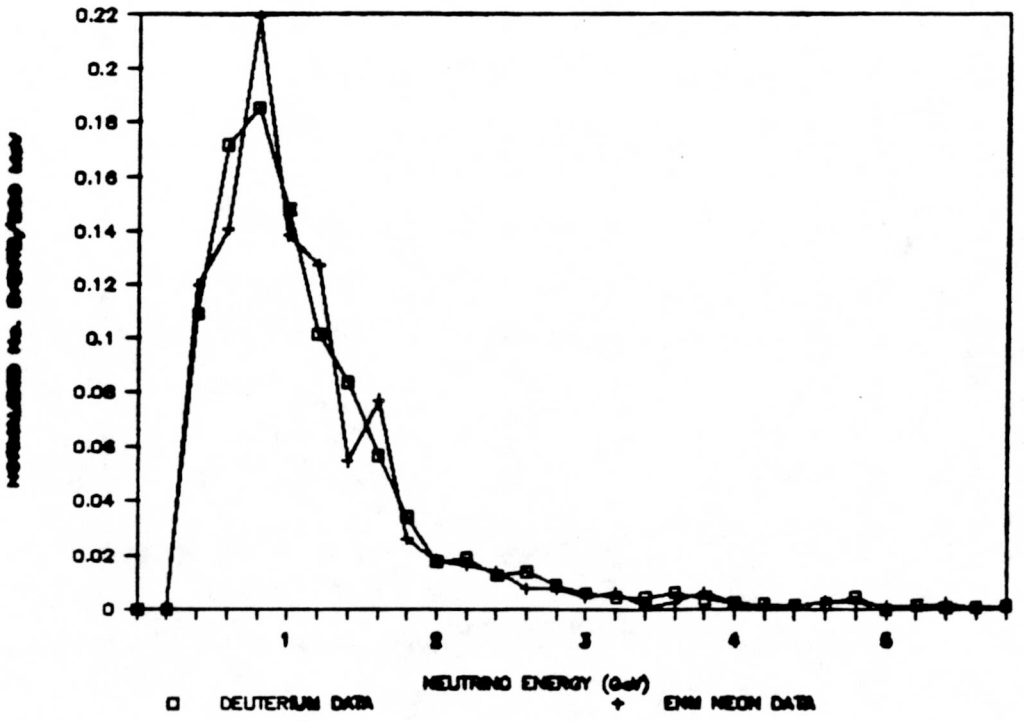

FIGURE 4-4a

NEON DATA MUON MOMENTUM DISTRIBUTION

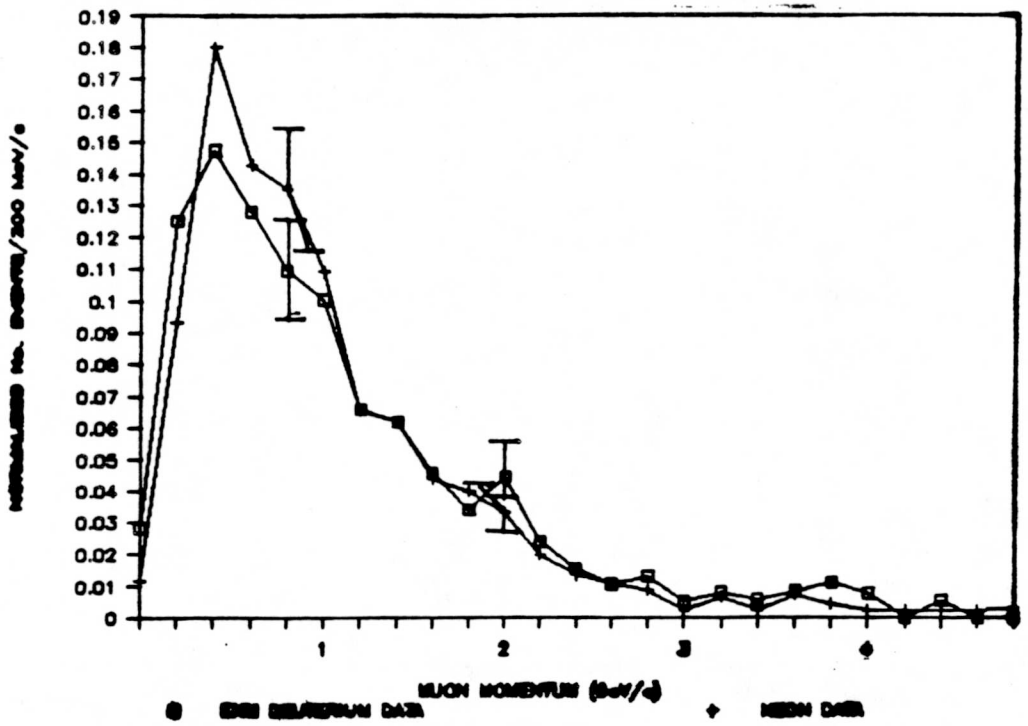

FIGURE 4-4b

DEUTERIUM DATA MUON MOMENTUM DISTRIBUTION

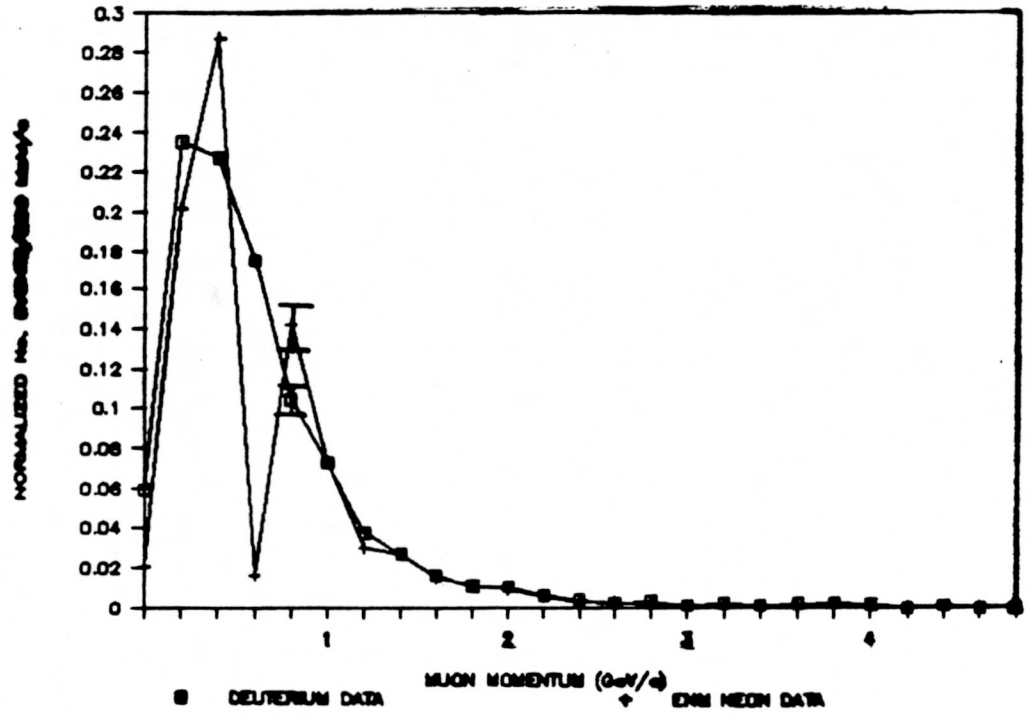

is, near $\cos\theta = 1$. In contrast, the lower energy deuterium data is expected to generate a more isotropic cosine distribution. Figures 4-5a) and b) confirm these expectations.

The distributions validate the ENM technique for comparing exclusive channel reactions between data sets by demonstrating the close correspondence between ν_μ-D (ν_μ-Ne) weighted and ν_μ-Ne (ν_μ-D) unweighted distribution shapes. ENM weighting, however, cannot relate accelerator-neutrino induced events to atmospheric-neutrino induced interactions, which is of primary concern to the nucleon decay community. A method which can is detailed in the next section.

4.3 Neutrino Flux Spectrum Weighting

By matching the accelerator-neutrino flux spectra from the ν_μ-D and ν_μ-Ne interactions to the atmospheric-neutrino flux spectrum, event population differences between the deuterium and neon data sets can be used to determine the effects of nuclear rescattering in nucleon decay searches. As a first step in "flux-weighting", the $\nu_{V\mu}$-D and ν_μ-Ne data spectra of all three neutrino sources are required. The atmospheric ν_μ-flux spectrum is taken from the work of Battistoni[1] for the energy region $0.4 < E_\nu < 6.0$ GeV. To compare the ZGS neutrino flux onto a deuterium fill to the

FIGURE 4-5a

NEON DATA MUON PRODUCTION ANGLE COSINE DISTRIBUTION

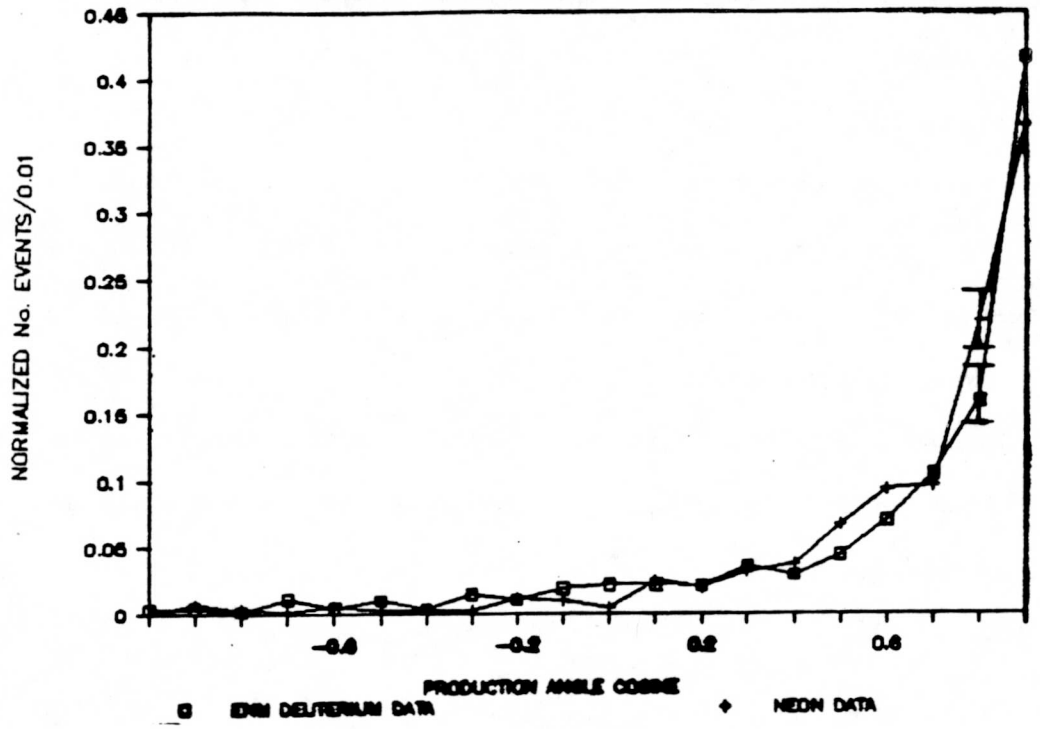

FIGURE 4-5b

DEUTERIUM DATA MUON PRODUCTION ANGLE COSINE DISTRIBUTION

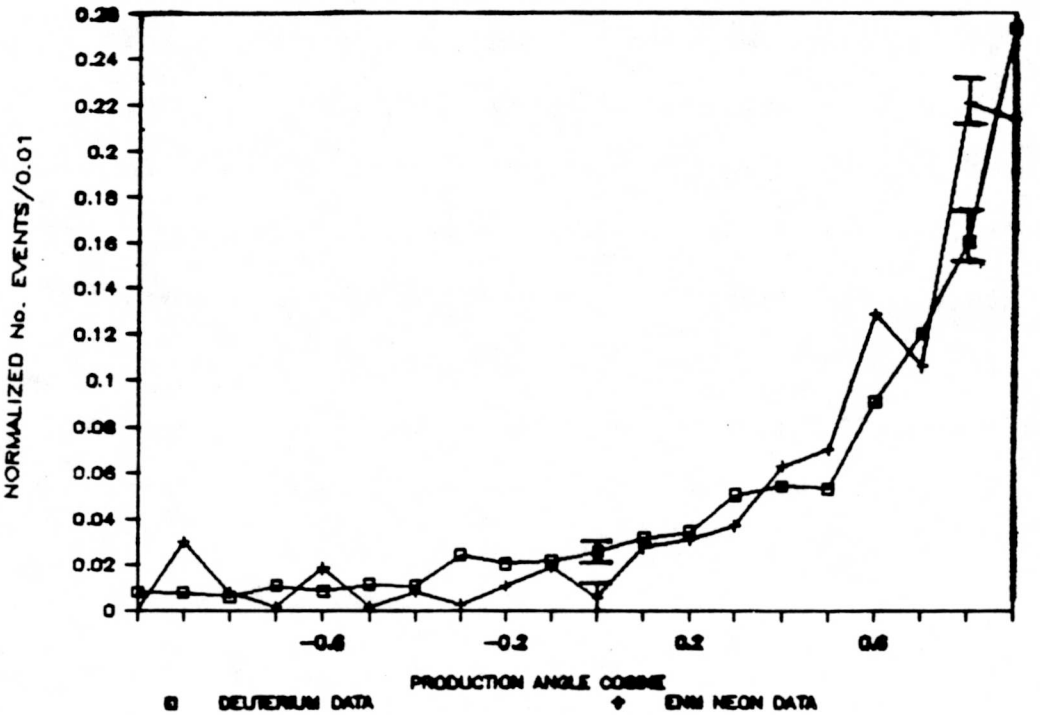

atmospheric flux calculated by Battistoni et al., we utilize the approach of Reference 2; in the latter work, the shape of the deuterium ν_μ-flux was normalized in the interval $0.6 < E_\nu < 2.0$ GeV. The neon neutrino flux spectrum has been calculated for the BEBC neutrino oscillation experiment using the CERN code NUBEAM (Ref. 3). The calculated neutrino energy spectrum has been checked[4] by folding the computed E_ν-distribution with cross sections and kinematics of relevant neutrino reaction channels from existing data. By including all details of BEBC event reconstruction, the event processes expected in the experiment were simulated, and good agreement was found between distributions extracted from simulated and observed events. For the purposes of weighting, the shapes of both the neon and deuterium neutrino flux spectra are separately normalized to the shape of the atmospheric neutrino spectrum over the energy range $0.4 < E_\nu < 6.0$ GeV. A correspondence between the shapes of the three neutrino fluxes is thus established as shown in Figure 4-6. The correspondence between flux shapes implies energy dependent event weights, presented in Figure 4-7. These weights enable direct comparisons between data sets. In addition, the atmospheric weights serve to convert the deuterium and neon distributions into ones appropriate for atmospheric ν_μ events.

To examine the consistency of the flux-weighting technique, events from both data sets are weighted to the atmospheric spectrum after event selection and processing corrections. Figures 4-8 show the "pseudo-atmospheric" neutrino energy distribution for both the deuterium and neon data sets. The distributions peak slightly below the nucleon mass and

FIGURE 4-6

ATMOSPHERIC AND EMPIRICAL NEUTRINO FLUX

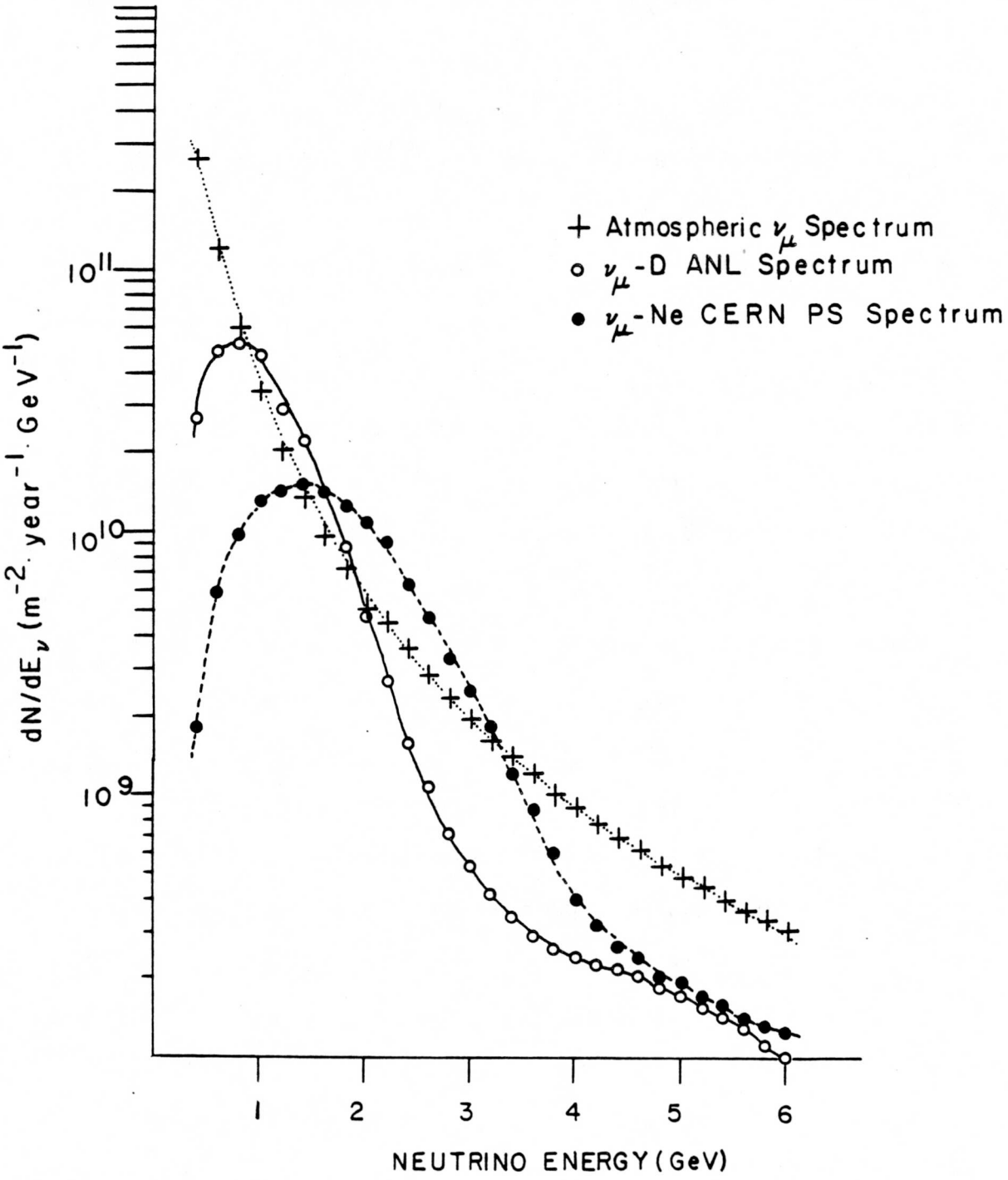

FIGURE 4-7

NEUTRINO FLUX WEIGHTS

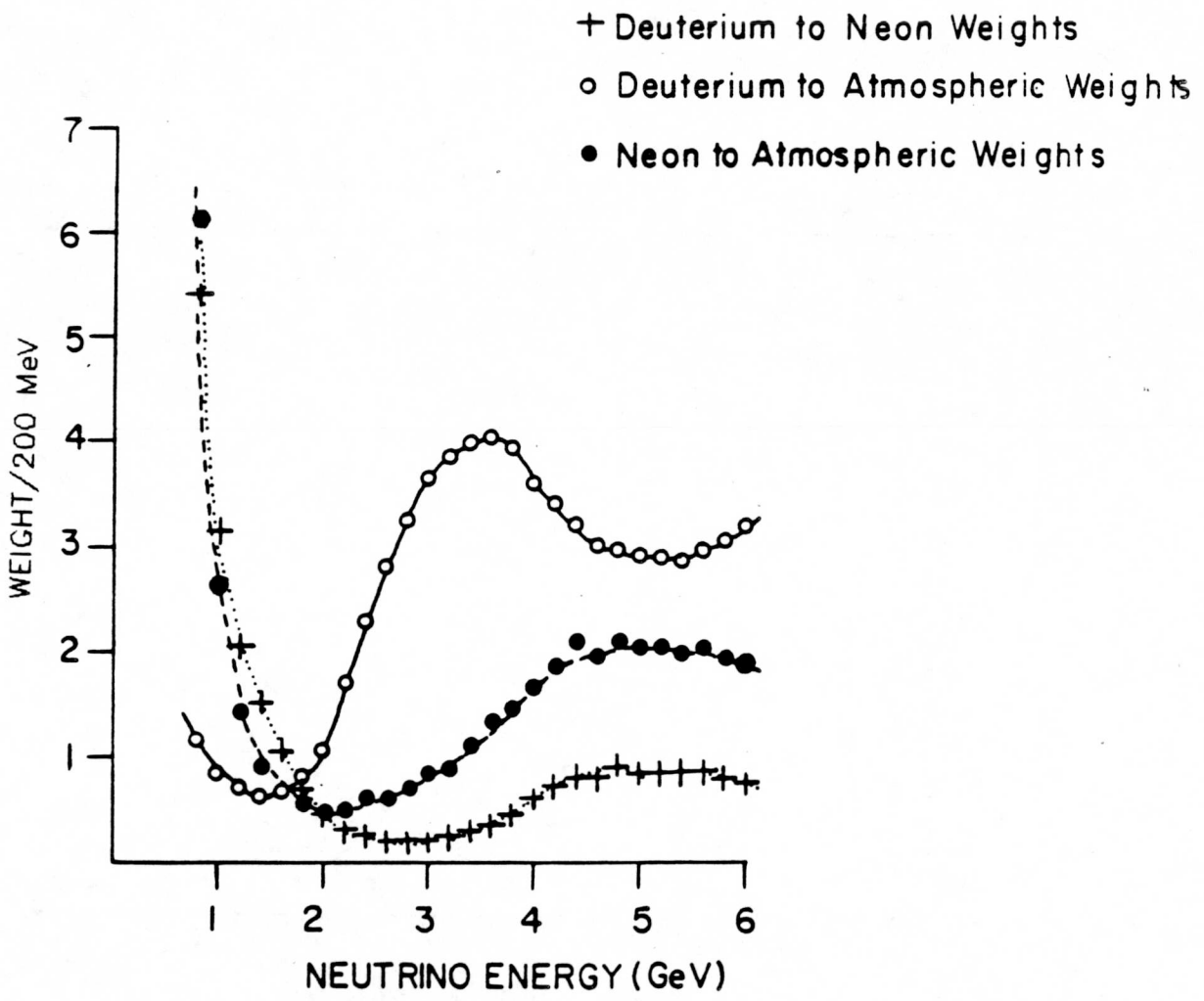

FIGURE 4-8

FLUX-WEIGHTED "PSEUDO-ATMOSPHERIC"
NEUTRINO ENERGY DISTRIBUTION

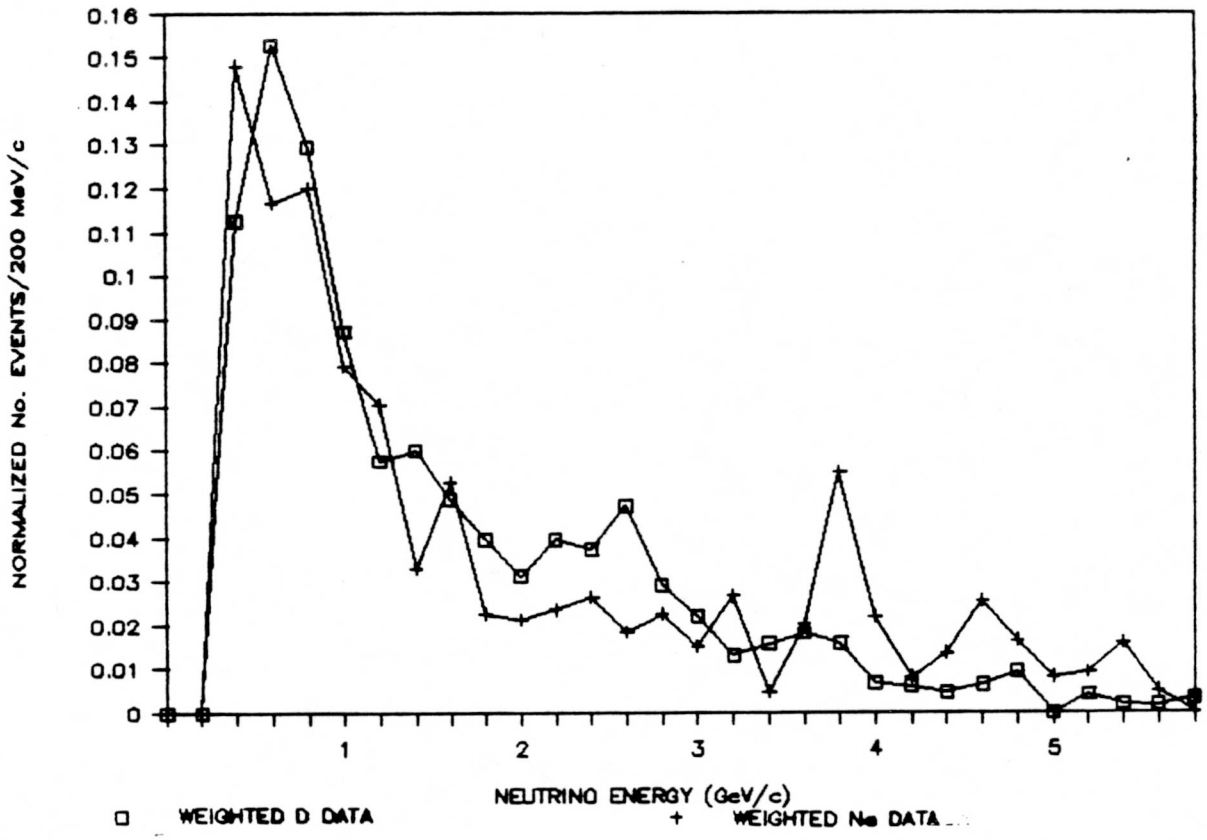

decrease with increasing energy, with statistical fluctuations apparent in both data sets.

The flux-weights can be tested using the muon momentum and production angle cosine distributions. These two quantities are free of target nucleus rescattering effects and therefore allow direct data comparisons. Since the atmospheric neutrino flux spectrum is nearer in energy and shape to the deuterium data distribution, the muon momentum and production angle distributions are expected to similarly mimic the deuterium distributions. Figure 4-9 shows the flux-weighted inclusive muon momentum distribution for both data sets which does assume the characteristics of the unweighted neutrino-deuterium distribution illustrated in Figure 4-4b); that is sharply peaked at ~300 MeV/c with the distribution decreasing rapidly as a function of momentum. However, the muon production angle cosine distribution, shown in Figure 4-10, differs from the lower energy deuterium distribution (illustrated in Figure 4-5b); the flux-weighted production angle distribution is more strongly peaked in the forward direction than the distribution of muon angles from deuterium.

Of concern for validation of the flux-weighting technique is how nearly the two data sets distributions match in shape. The chi-squared per degree of freedom for match-up between the flux-weighted muon momentum distributions is 0.34; the match-up between the muon production angle distributions is χ^2 (per degree freedom) = 0.67. Thus the match between the shapes of these distributions is excellent, as is apparent from Figures 4-9 and 4-10.

FIGURE 4-9

MUON MOMENTUM DISTRIBUTION

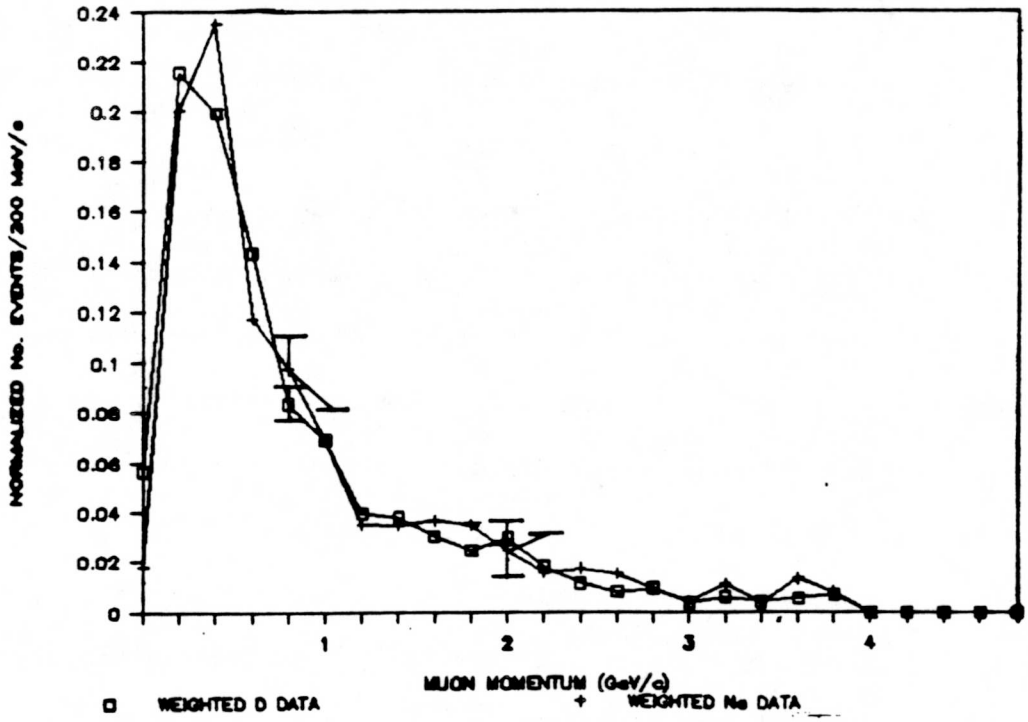

FIGURE 4-10

MUON PRODUCTION ANGLE COSINE DISTRIBUTION

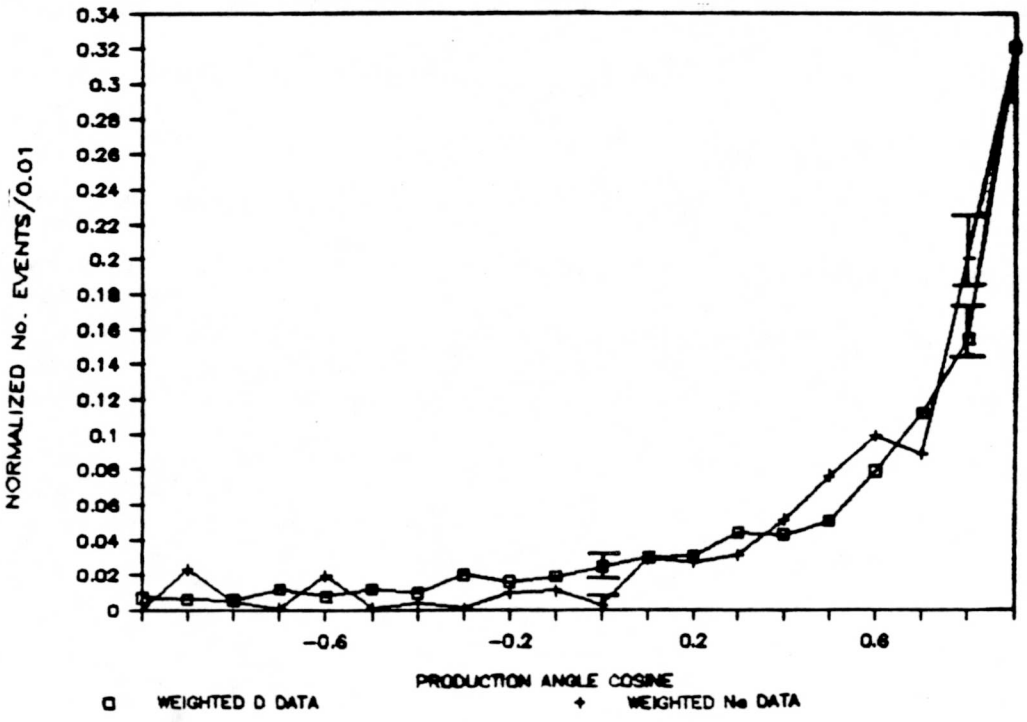

To check how the flux-weighting method compares with traditional cosmic-ray generated neutrino flux calculations, we compare the muon energy distributions for quasi-elastic ν_μ-D and ν_μ-Ne events with the predicted distribution as calculated by Gaisser and O'Connell[5]. In their paper, Gaisser and O'Connell calculate the lepton spectra induced by cosmic-ray neutrino interactions in oxygen. The computed spectra reproduce the empirical Kamioka data and has been employed in later papers by Gaisser, Stanev, and Barr[6,7] to compute the atmospheric neutrino flux for several nucleon decay detectors around the world.

The quasi-elastic muon energy distribution from Reference (5) and the ν_μ-D and ν_μ-Ne interactions are shown in Figure 4-11. These distributions are all normalized in the energy region $0.4 < E(\mu) < 1$ GeV, indicated in the Figure 4-11 inset. The distributions match closely in the region $E(\mu) > 400$ MeV. The close shape correspondence of the two data sets with the computed muon energy spectrum is indicative of the verity and utility of the flux-weighting technique.

4.4 Weighting Techniques Summary

This chapter has sought to define and validate two independent weighting schemes for comparing data. The first method utilizes the observed neutrino energy distribution in reaction channels while the second uses the (inclusive) neutrino flux spectra.

FIGURE 4-11

QUASI-ELASTIC MUON ENERGY DISTRIBUTION

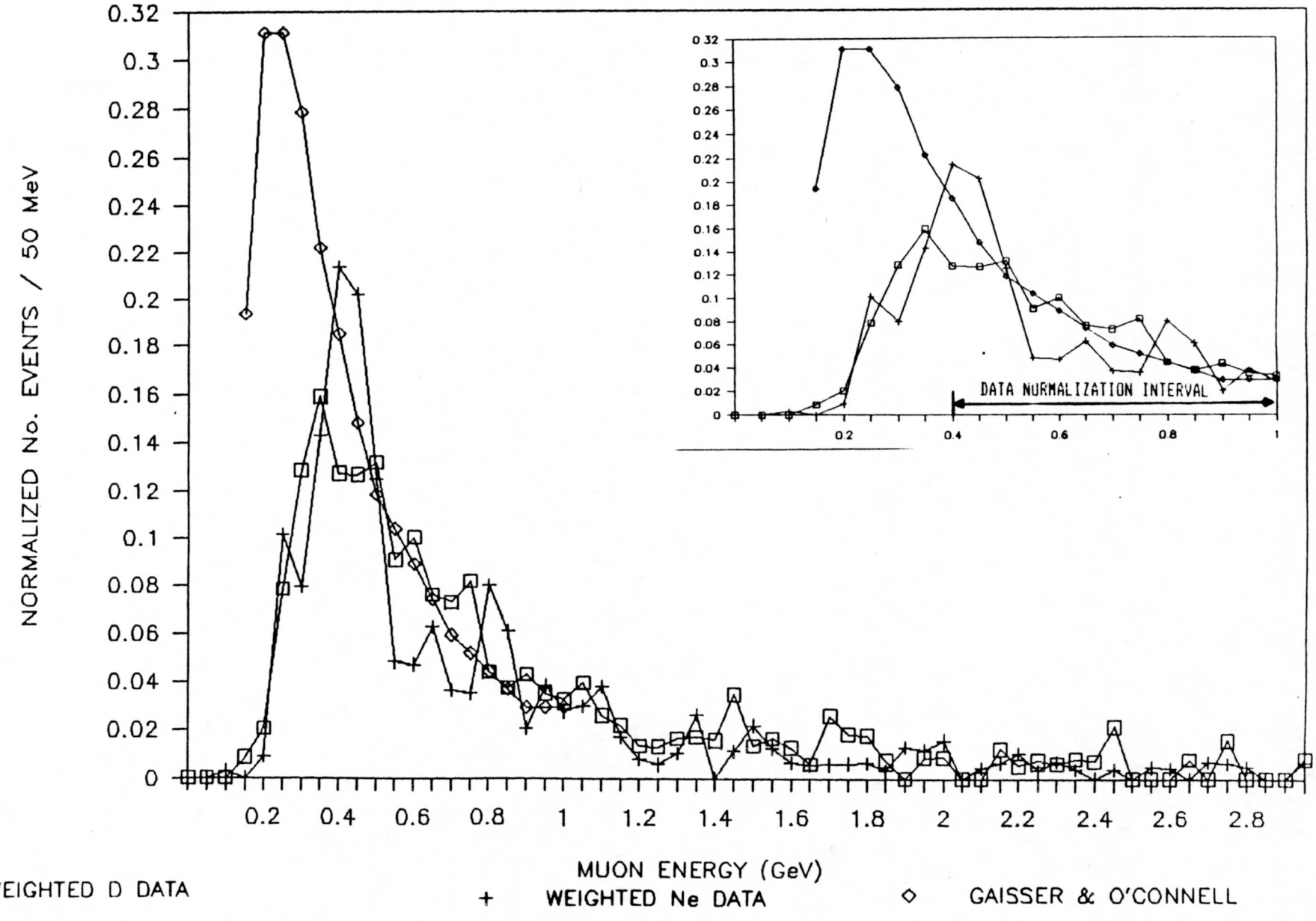

The Energy Normalized Method is a straightforward weighting technique. Its limitation is due to the fact that E_ν energy distributions are the result of the "convolution" of a neutrino-flux spectrum with a reaction cross-section, $\sigma(E_\nu)$. Since $\sigma(E_\nu)$ varies for different neutrino reactions, especially so in reaction threshold regimes, ENM weighting can be invoked on an exclusive, channel-by-channel basis, or inclusively, and completely different weights must be calculated separately for each specific reaction comparison. Event flux-weighting avoids this problem by using the experimental neutrino flux spectra which are independent of production cross-section. There is, however, uncertainty associated with how well these spectra have been calculated and checked in the original experiments. This reservation aside, only one set of weights needs to be determined in the flux-weighting approach. The resulting weights can be used in any comparative studies, either in exclusive channel comparisons or in inclusive ones.

While both methods can be used to compare empirical data, only the flux-weighting method can be employed to translate the deuterium and neon events into atmospheric-induced interactions. For this reason, the flux-weighting method will be used to relate the existing data to nucleon decay predictions.

References

1. G.Battistoni et al., Nucl. Instrum. Methods 219, 300 (1984).

2. M.Derrick et al., Phys. Rev. D30, 1605 (1984).

3. C.Angelini et al., Phys. Lett. B179, 307 (1986).

4. S.Katsanevas and M.Vassiliou, "Simulation of ν Interactions for PS180", Memo - Athens University, July 10, 1985.

5. T.K.Gaisser and J.S.O'Connell, Phys. Rev. D34, 822 (1986).

6. T.K.Gaisser, T.Stanev, and G.Barr, Phys. Rev. D38, 85 (1988).

7. G.Barr, T.K.Gaisser, and T.Stanev, Phys. Rev. D39, 3532 (1989).

CHAPTER 5

COMPARISON OF DEUTERIUM AND NEON REACTION CHANNELS

5.1 Introduction

With clean neutrino event samples and the processing and flux spectrum weights having been obtained, our investigation of intranuclear rescattering effects can begin. Before the deuterium and neon event samples can be compared in detail, however, final corrections to the neon data must be made. The processing of the ν_μ-neon events did not include kinematical fitting to reaction hypotheses, unlike the processing of the ν_μ-deuterium data. As a result, comparisons between deuterium and neon data in both the quasi-elastic and pion production channels require correction for unobserved neutral pions in the neon data. This analysis is described in Section 5.2.

In Section 5.3, initial comparisons of the two neutrino exposures are made by comparing the relative final state populations in exclusive channels within each data set. Effects due to Fermi motion are treated in later chapters, and deuterium rescattering effects are ignored. Differences in these populations are evidence for intranuclear rescattering. Section 5.4 summarizes the Chapter.

5.2 Corrections for Neutral Pions in Exclusive Neon Channels

The ν_μ-neon data consists of bubble chamber events for which all visible particles were geometrically reconstructed; however, no kinematic fitting was attempted. Consequently, final state $\pi^\circ \rightarrow \gamma\gamma$ decays which did not result in gamma conversion in the bubble chamber are undetected. However, it is possible to estimate, on average, the numbers of missing π°s on a channel-by-channel basis using either of two methods. The primary method, described in Section 5.2.1, utilizes known photon conversion length probabilities for neon together with average potential conversion paths to calculate ϵ_γ and subsequently the number of π°s. The second method, used as an independent check on the conversion length analysis, determines the efficiency for detecting photons, ϵ_γ, based on the number of recorded single-, double-, and triple-gamma events. This technique is described in Section 5.2.2. Section 5.2.3 summarizes the results obtained from application of each method.

5.2.1 Estimate of π° Production via Conversion Length Analysis

The number of neutral pions which originate in the energetically accessible exclusive charged current reactions

$$\nu Ne \rightarrow \mu^- p(\ell\pi^\circ),\ \ell = 1,\ 2,\ \text{and}\ 3 \qquad (5\text{-}1)$$

is related to the observed number of converting photons within the bubble chamber fiducial volume for a given radiation length. The photon conversion length, λ_c, is given by[1]:

$$\lambda_c = (9/7)\ x_o,\ x_o = \text{radiation length} \qquad (5\text{-}2)$$

for gamma energies greater than 1 GeV. Given a total number of photons in the experiment, N_T, the number of photons which remain unconverted with at distance x is:

$$N_T(x) = N_T \exp(-x/\lambda_c). \qquad (5\text{-}3)$$

The probability for a photon conversion within a distance x, P(x), is then equal to the fraction of the total number of gammas less $N_T(x)$ divided by the total number of photons. That is,

$$\begin{aligned} P(x) &= [N_T - N_T(x)]/N_T \\ &= 1 - (N_T(x)/N_T) \\ &= 1 - \exp(-x/\lambda_c). \end{aligned} \qquad (5\text{-}4)$$

This probability is the asymptotic (i.e., high photon momentum) photon conversion efficiency, E_γ. Hence

$$E_\gamma = 1 - \exp(-7x/9x_o) \text{ for } E_\gamma > 1 \text{ GeV}. \qquad (5\text{-}5)$$

The bubble chamber and experimental run conditions provide the values for the average conversion path length, x, and the radiation length, x_o.

For the mean conversion path length, we take the bubble chamber radius which, for this BEBC experiment, is 180 cm. Determination of the radiation length is provided in Reference 2: the experiment consisted of two runs, approximately equal in duration, with radiation lengths of 47 cm and 43 cm. For the purposes of this analysis, a value of x_o = 45 cm is used. With this value, the conversion can be computed via Equation 5-2, λ_c = 58 cm. The number of unconverted photons within the distance x = 180 cm, $N_T(x)$, equals 0.05 and so E_γ equals 0.95 for photons with energy greater than 1 GeV.

The average photon energy for the neon experiment is approximately 0.1 GeV, as is indicated in Figure 3-3 in Chapter 3. The photon conversion

efficiency, ϵ_γ, of these gammas is interpolated using the photon energy absorption distributions of Reference 3 and is observed to be $\epsilon_\gamma \sim E_\gamma/2$. Thus, the average gamma conversion efficiency for the ν_μ-neon experiment is approximately 0.48 using mean conversion path analysis.

This value was input to the the MINUIT fitting program to determine the number of one-, two-, and three-neutral pion events produced in the Equation 5-1 reaction channel. The fitted results indicate 23 ± 9, 22 ± 8, and 0 ± 6 single-, double-, and triple-π° events were produced in the reaction channel examined.

5.2.2 Estimate of π° Production from Observed Gamma Conversions

An alternate method for determining the number of π°s in the Equation 5-1 reaction channel is to use the number of observed gamma-containing events in that channel to determine the experimental photon conversion efficiency. For the Equation 5-1 final state, the number of potentially observed photons, T_γ, range from only one gamma seen, $T_\gamma(1)$, to all six photons observed, $T_\gamma(6)$. These observed number of events are listed in Table 5-1 and can be used to determine the number of single-, double-, and triple-π° events produced in the above reaction.

The number of single-π° events produced, L, is equal to

$$L = L_0+L_1+L_2 \qquad (5\text{-}6)$$

where L_0 is the number of (single neutral pion) events with no gammas observed, L_1 is the number of events with a single photon seen, and L_2 is the number of events with both gammas detected. The values for L_0, L_1, and L_2 are determined using the gamma conversion efficiency, ϵ_γ. Thus, L_2 is

TABLE 5-1

DISTRIBUTION OF $\mu^-\pi(\ell\pi^0)$ EVENTS CONTAINING
N CONVERSION PHOTONS

$T_\gamma(n)$ = number of events containing n-gammas

$T_\gamma(1)$ = 15 events
$T_\gamma(2)$ = 18 events
$T_\gamma(3)$ = 4 events
$T_\gamma(4)$ = 0 events
$T_\gamma(5)$ = 1 event
$T_\gamma(6)$ = 0 events

equal to the total number of single-π° events produced times the probability that both gammas converted in the bubble chamber:

$$L_2 = L\epsilon_\gamma^2 \tag{5-7}$$

The total number of single-gamma, one π° events, L_1, is equal to the total number of single neutral pions produced times the sum of the probability of converting photon A and not photon B added to the probability of converting photon B and not photon A:

$$\begin{aligned} L_1 &= L\,[\epsilon_\gamma(1-\epsilon_\gamma) + (1-\epsilon_\gamma)\epsilon_\gamma] \\ &= 2L\epsilon_\gamma(1-\epsilon_\gamma). \end{aligned} \tag{5-8}$$

Finally, the number of single-π° events in which no photons are converted, L_0, is equal to:

$$L_0 = L\,(1-\epsilon_\gamma)^2. \tag{5-9}$$

Similar arguments for double- and triple-π° production yields the following equations:

$$M = \sum_{i=0}^{4} M_i$$

$$\begin{aligned} M_0 &= M\,(1-\epsilon_\gamma)^4 & M_1 &= 4M\,(1-\epsilon_\gamma)^3\epsilon_\gamma \\ M_2 &= 6M\,(1-\epsilon_\gamma)^2\epsilon_\gamma^2 & M_3 &= 4M\,(1-\epsilon_\gamma)\epsilon_\gamma^3 \\ M_4 &= M\epsilon_\gamma^4 \end{aligned} \tag{5-10}$$

$$N = \sum_{i=0}^{6} N_i$$

$$\begin{aligned} N_0 &= N\,(1-\epsilon_\gamma)^6 & N_1 &= 6N\,(1-\epsilon_\gamma)^5\epsilon_\gamma \\ N_2 &= N\,(1-\epsilon_\gamma)^4\epsilon_\gamma^2 & N_3 &= 20N\,(1-\epsilon_\gamma)^3\epsilon_\gamma^3 \\ N_4 &= 9N\,(1-\epsilon_\gamma)^2\epsilon_\gamma^4 & N_5 &= 3N\,(1-\epsilon_\gamma)\epsilon_\gamma^5 \\ N_6 &= N\epsilon_\gamma^6. \end{aligned} \tag{5-11}$$

The number of one-, two-, and three-π^0 events, as well as the gamma conversion efficiency, can be determined by correlating the T_γ values in Table 5-1 with the corresponding $L_i+M_i+N_i$ equations. Thus,

$$\begin{aligned}
&\text{For 1-}\gamma\text{ conversions:} && 2(1-\epsilon_\gamma)\epsilon_\gamma[L + (1-\epsilon_\gamma)^2M + (1-\epsilon_\gamma)4N] = 15. \\
&\text{For 2-}\gamma\text{ conversions:} && \epsilon_\gamma^2[L + 6M(1-\epsilon_\gamma)^2 + 15N(1-\epsilon_\gamma)^4] = 18. \\
&\text{For 3-}\gamma\text{ conversions:} && 4\epsilon_\gamma[(1-\epsilon_\gamma)M + 5N(1-\epsilon_\gamma)^3] = 4. \\
&\text{For 4-}\gamma\text{ conversions:} && \epsilon_\gamma^4[M + 9N(1-\epsilon_\gamma)^2] = 0. \\
&\text{For 5-}\gamma\text{ conversions:} && 3N\epsilon_\gamma^5(1-\epsilon_\gamma) = 1.
\end{aligned} \qquad (5\text{-}12)$$

These relations provide five constraining equations in four variables. Using a chi-squared constraint, the above equations were fitted using the MINUIT software program. The photon conversion efficiency obtained from the fit is $\epsilon_\gamma = 0.67 \pm 0.08$, and the fitted number of single-, double-, and triple-π^0 events are 34 ± 7, 5 ± 6, and 5 ± 7, respectively.

5.2.3 Summary of π^0 Population Estimations

Because the events in the ν_μ-neon data were not fit to final state hypotheses, an effort has been made to compute the number of neutral pions in the exclusive reaction channel

$$\nu Ne \rightarrow \mu^- p(\ell\pi^0),\ \ell = 1, 2, 3 \qquad (5\text{-}13)$$

by estimating the gamma conversion efficiency for the BEBC chamber. The number of π^0-containing events estimated after correction for gamma conversion losses is, of course, larger than the number of events in which a

photon or a π^0 is observed. The difference presumably corresponds to the number of $\mu^-p(\ell\pi^0)$ events incorrectly assigned to the quasi-elastic reaction μ^-p. Thus correction for undetected photons entails reassigning a specific number of events from the quasi-elastic to the $\mu^-p(\ell\pi^0)$ channel.

To estimate the gamma conversion efficiency, two independent approaches have been employed. The first method employed the chamber's conversion and radiation lengths to compute ϵ_γ directly. The second method utilizes the MINUIT fitting routine to determine the gamma conversion efficiency, ϵ_γ, subject to physical and empirical constraints. The values obtained by these two methods are 0.48 ± 0.07 and 0.67 ± 0.08, respectively.

The photon conversion length analysis is considered by us to be the more straightforward and hence reliable method of determining the gamma conversion efficiency. The second method may be sensitive to correlated losses in low-momentum gammas, and consequently yields an overly "optimistic" value for ϵ_γ. We regard the second method to provide an upper bound on the gamma conversion efficiency which is compatible with our conversion length determination. Hereafter we use the value ϵ_γ = 0.48 ± 0.07 to correct for unobserved photons. This ϵ_γ value is then used to compute the total number of π^0 events produced in the reactions of Equation 5-13. We note that the use of a higher ϵ_γ value would induce changes in the single-, double-, and triple-π populations. However, the total number of neutral pions remains approximately either 45 or 44 for ϵ_γ = 0.48 or 0.67, respectively.

5.3 Neutrino-Deuterium and ν_μ-Neon Final State Comparisons

Having corrected for unobserved neutral pions in the neon data set, the relative populations of final states in the ν_μ-D and ν_μ-Ne data can be compared and examined for evidence of pion-nucleon rescattering. The relative numbers of charged-current events generated by atmospheric neutrinos in deuterium and neon are determined. Table 5-2 lists the final state fractions for both exposures from an atmospheric flux. The parenthetical values for the neon quasi-elastic and $\mu^-p(\ell\pi^\circ)$ production final states show their population without corrections for neutral pions.

The final column of Table 5-2 shows the difference in the fractional population of final states between the deuterium and neon data sets. The neon final state populations are depleted in all three single pion final states ($\mu^-\pi^+p$, $\mu^-\pi^\circ p$, and $\mu^-\pi^+n$). These channels represent the bulk of the pion production since multi-pion production is at threshold for our neutrino energies. The net population <u>decrease</u> in these channels, coupled with the population <u>increase</u> in the neon quasi-elastic channels relative to the deuterium population, indicates the occurrence of pion absorption in the neon nucleus.

The final row of Table 5-2 summarizes ν_μ-neon events which do not conform to expected final state charges; that is, reactions which are not "clean" ν_μ-proton interaction with total final state charge $Q_T = +1$, or clean ν_μ-neutron interactions with $Q_T = 0$. These events are evidence for rescattering of final state hadrons within the nucleus. From the latter weighted event populations alone, pion rescattering within neon is seen to

TABLE 5-2

E-412 DEUTERIUM AND NEON DATA WEIGHTED TO ATMOSPHERIC:
FRACTIONAL POPULATION DISTRIBUTION

Reaction	Deuterium		Neon		Δ(D-Ne)
	Weighted Number	Fraction	Weighted Number	Fraction	
$\nu p \rightarrow \mu^- \pi^+ p$	272 ± 21	0.19 ± 0.02	73 ± 9	0.14 ± 0.02	0.05 ± 0.02
$\nu p \rightarrow \mu^- \pi^+ (\ell\pi^\circ) p$, $\ell \geq 1$	20 ± 14	0.01 ± 0.01	9 ± 3	0.02 ± 0.01	-0.01 ± 0.01
$\nu p \rightarrow \mu^- \pi^+ \pi^+ (m\pi^\circ) n$, $m \geq 0$	19 ± 6	0.01 ± 0.01	9 ± 5	0.02 ± 0.01	-0.01 ± 0.01
$\nu p \rightarrow \mu^- \pi^- \pi^+ \pi^+ p$	14 ± 4	0.01 ± 0.01	1 ± 1	0.01 ± 0.01	0.0 ± 0.01
$\nu p \rightarrow \mu^- \pi^- \pi^+ \pi^+ \pi^\circ p$	0	-	0	-	-
$\nu p \rightarrow \mu^- \pi^- \pi^+ \pi^+ \pi^+ n$	0	-	1 ± 1	0.0 ± 0.01	0.0 ± 0.01
$\nu n \rightarrow \mu^- p$	715 ± 36	0.49 ± 0.03	306 ± 21 (324±24)*	0.58 ± 0.04 (0.61±0.04)*	-0.09 ± 0.05 (-0.12±0.05)*
$\nu n \rightarrow \mu^- (\ell\pi^\circ) p$	138 ± 16	0.10 ± 0.01	45 ± 17 (27 ± 5)*	0.09 ± 0.03 (0.05±0.01)*	0.01 ± 0.03 (0.05±0.01)*
$\nu n \rightarrow \mu^- \pi^+ n$	202 ± 26	0.14 ± 0.02	38 ± 8	0.07 ± 0.01	0.07 ± 0.01
$\nu n \rightarrow \mu^- \pi^+ (\ell\pi^\circ) n$	0	-	4 ± 2	0.01 ± 0.01	-0.01 ± 0.01
$\nu n \rightarrow \mu^- \pi^- \pi^+ p$	36 ± 9	0.02 ± 0.01	15 ± 4	0.03 ± 0.01	0.0 ± 0.01
$\nu n \rightarrow \mu^- \pi^- \pi^+ (\ell\pi^\circ) p$	14 ± 7	0.01 ± 0.01	4 ± 3	0.01 ± 0.01	0.0 ± 0.01
$\nu n \rightarrow \mu^- \pi^- \pi^+ \pi^+ (m\pi^\circ) n$	7 ± 4	0.01 ± 0.01	1 ± 1	-	0.01 ± 0.01
$\nu n \rightarrow \mu^- \pi^- \pi^- \pi^+ \pi^+ p$	0	-	0	-	-
$\nu n \rightarrow \mu^-$ + Strange	10 ± 4	0.01 ± 0.01	1 ± 1	0.01 ± 0.01	0.0 ± 0.01
$\nu N \rightarrow \mu^-$ + (Q=-1,+3,+4)			17 ± 4	0.03 ± 0.01	-0.03 ± 0.01
Total	1446		524		

*Neon rates without π° corrections.

occur at least once in every 33 atmospheric neutrino-induced reactions. Table 5-3 summarizes the three $\nu_\mu n$ and 14 $\nu_\mu p$ interactions which constitute the (unweighted) sample of events with this rescattering signature.

5.4 Summary

This chapter presented initial results from ν_μ-neon and ν_μ-deuterium comparisons of interest to nucleon decay experiments. By weighting both data sets to the atmospheric spectrum and correcting for unobserved π°s, a direct comparison of final state topologies shows evidence for nuclear rescattering in neon to occur in neutrino reactions corresponding to the atmospheric flux spectrum. The amount of rescattering is expected to scale with nuclear density (proportional to $A^{1/3}$) and should thus be more pronounced (perhaps by a factor of 1.4) in the iron tracking calorimeter experiments.

References

1. E.Segre, Nuclei and Particles, W A Benjamin, Reading MA (1977), p. 71.
2. C.Angelini et al., Phys. Lett. B179, 307 (1986).
3. Particle Data Group, Review of Particle Properties, Phys. Lett. 170B, 1-350 (1986), p. 51.

TABLE 5-3

NON-$\nu p(Q=1)$ or $-\nu n(Q=0)$ NEON EVENTS
WEIGHTED TO ATMOSPHERIC SPECTRUM*

	Charge	No. of Events	Weighted No. of Evts	Number of Evts. by Charge
$\nu p \rightarrow \mu^- \pi^- p$	-1	5	5.722	
$\nu n \rightarrow \mu^- \pi^- \pi^+ n$	-1	1	1.129	6.851
$\nu p \rightarrow \mu^- \pi^+ \pi^+ p$	+2	3	2.438	
$\nu n \rightarrow \mu^- \pi^+ \pi^+ \pi^+ n$	+2	2	1.473	
$\nu p \rightarrow \mu^- \pi^- \pi^+ \pi^+ \pi^+ p$	+2	2	1.357	5.768
$\nu p \rightarrow \mu^- \pi^+ \pi^+ \pi^+ p$	+3	3	3.531	
$\nu p \rightarrow \mu^- \pi^+ \pi^+ \pi^+ \pi^\circ p$	+3	1	1.489	5.020
Total		17		17.639

*All events restricted to $0.4 < E_\nu < 3.6$ GeV.

CHAPTER 6

PION INTRANUCLEAR RESCATTERING

6.1 Introduction

The previous chapter presented evidence for pion absorption and charge exchange in the neon data. As a prelude to a more comprehensive intranuclear rescattering analysis, this chapter reviews published data on scattering processes involving pions incident upon atomic nuclei. Pion momentum range under consideration here extend from 0 to 1 GeV/c. Pion intranuclear rescattering can involve any of four processes:

i) Charge exchange scattering, in which a charged (neutral) pion changes into a neutral (charged) pion; the scattered pion may be momentum-degraded and deflected, relative to the initial pion.

ii) Absorption, in which the pion "disappears" in the nuclear medium; the resultant energy transfer to the nucleus may result in the "boil-off" of a "stub" nucleon.

iii) Elastic scattering; the pion retains its momentum magnitude but is deflected into small angles.

iv) Inelastic scattering, in which the pion's identity is maintained but its momentum is degraded in magnitude and may be deflected to large angles.

These low energy interactions of hadrons within nuclei are of considerable interest to nucleon decay searches since they can alter otherwise tell-tale baryon decay kinematic signatures. Conversely, atmospheric neutrino-induced reactions, interacting within a nucleon decay detector, could mimic nucleon decay events through occurrence of one or more of the above rescattering processes.

Section 6.2 describes the rescattering processes as currently understood from pion-nucleon scattering experiments. The π-N scattering cross-section can be conveniently decomposed into constituent scattering processes and the kinematic quantities relevant to each can be identified. Section 6.3 examines the phenomenology of pion charge exchange scattering. Using invariance principles, this process is shown to be describable with a single transition probability (rather than four). Section 6.4 summarizes the chapter.

6.2 Pion Scattering on Nuclei

It is useful to review the existing pion-nucleus interaction data to note scattering trends and resonance structure. The published results are helpful in defining analysis approaches to intranuclear ν_μ-Ne rescattering and in assessing our results. Low energy pion interactions, around 200 MeV in the incident pion kinetic energy, strongly excite the first Δ resonance at 1232 MeV/c^2 - pion-nucleon total cross-sections in this resonance region are of order 135 mb[1]. Resonant states, such as the Δ and N^*, can themselves interact with other nucleons, and may mask the direct effects of pion intranuclear rescattering.

The angular distributions of scattered pions, integrated over their final state energies, are shown in Figure 6-1 for positive pions at a kinetic energy of 165 MeV (π^+ momentum 267 MeV/c). These differential cross section distributions, from Ashery et al.[2] are from six atomic targets ranging from lithium (A=3) to bismuth (A=83). All differential cross section distributions display strong peaking in the forward direction, and milder backward scattering. These trends are observed at all energies.

The π-N scattering differential cross section can be characterized by two main effects. At forward angles, the cross section is dominated by elastic scattering, and the dashed lines are the result of elastic scattering calculations (see Reference 2). From Figure 6-1, it can be seen that elastic scattering causes pion deflections which are well within 45°. At backward angles, the cross section is due to inelastic and charge exchange scattering; these two processes can result in pion deflections greater than 90°, and so can cause pions to migrate over hemisphere boundaries. The solid lines at backward angles is the free $(\pi^+p)+(\pi^+n)$ cross section normalized to the data[2]. Figure 6-2a) shows the energy dependence of the pion-nucleon total cross section, while Figure 6-2b) shows the components of pion strong interaction cross sections based on experimental data[3]. Several phenomenological fits[4] and models[5] exist which reproduce the differential cross sections for various nuclei and energies.

6.3 Charge Exchange Phenomenology

The charge exchange transitions for pions interacting on nucleons are:

FIGURE 6-1

DIFFERENTIAL SCATTERING CROSS SECTION
OF 165 MeV π^+ ON NUCLEI*

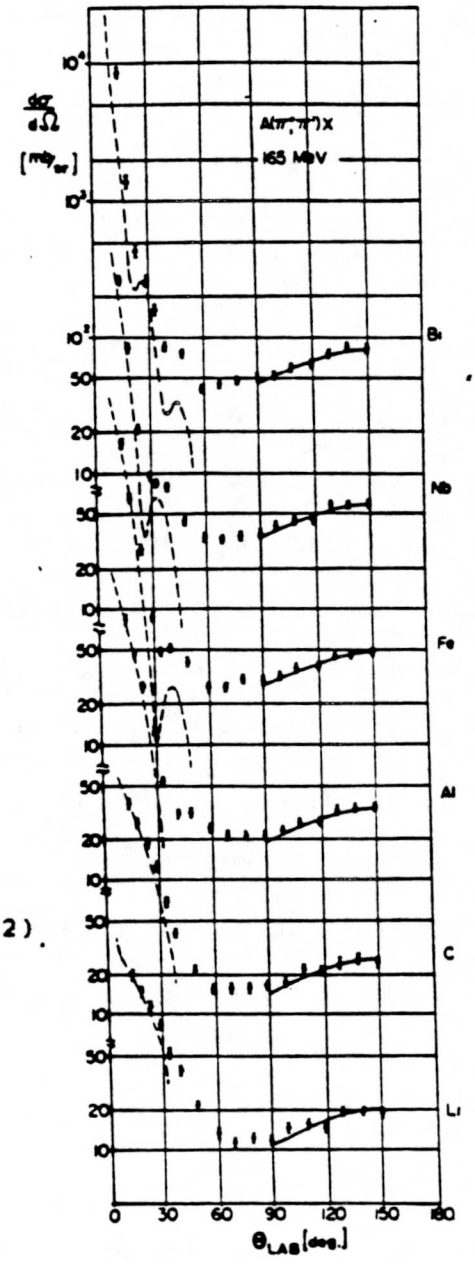

*From D. Ashery, et al.(2).

FIGURE 6-2a

PION-NUCLEUS TOTAL CROSS SECTION ENERGY DEPENDENCE

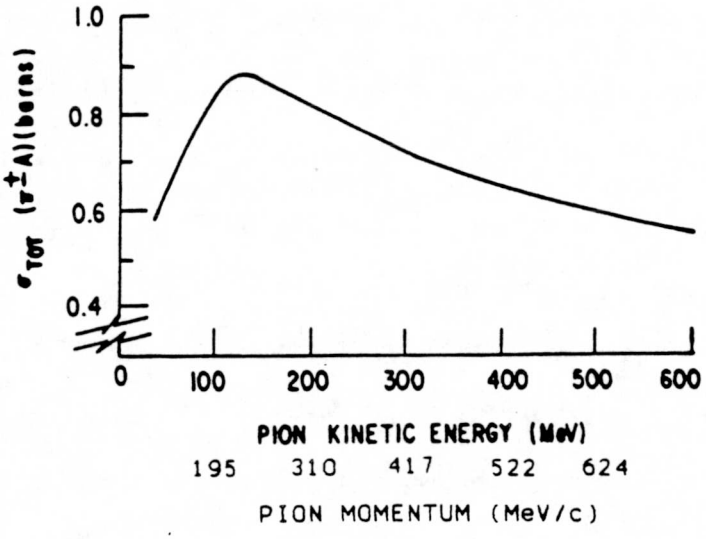

FIGURE 6-2b

ENERGY DEPENDENCE OF THE PION STRONG-INTERACTION CROSS SECTION COMPONENTS

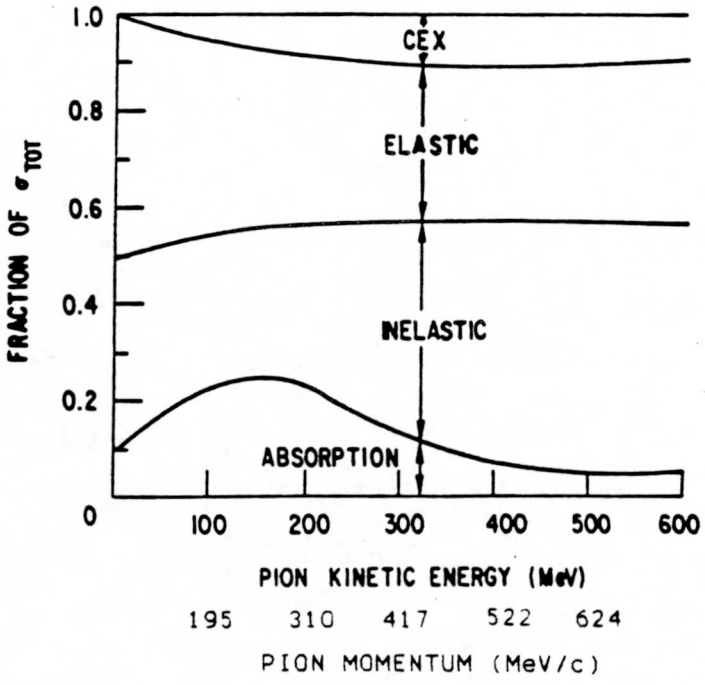

$$\pi^+ n \rightarrow \pi^\circ p \qquad [6\text{-}1]$$

$$\pi^\circ p \rightarrow \pi^+ n \qquad [6\text{-}2]$$

$$\pi^\circ n \rightarrow \pi^- p \qquad [6\text{-}3]$$

$$\pi^- p \rightarrow \pi^\circ n. \qquad [6\text{-}4]$$

By time reversal symmetry, transition [6-1] has the same amplitude as the transition of [6-2]; similarly, transition [6-3] is identical to transition [6-4]. Assuming that the target nucleus is isoscalar, transition [6-1] can be decomposed into isospin amplitudes:

$$|\pi^+ n\rangle = |1,1;1/2,-1/2\rangle = \sqrt{1/3}|3/2,+1/2\rangle + \sqrt{2/3}|1/2,+1/2\rangle \quad (6\text{-}5)$$

$$|\pi^\circ p\rangle = |1,0;1/2,+1/2\rangle = \sqrt{2/3}|3/2,+1/2\rangle - \sqrt{1/3}|1/2,+1/2\rangle. \quad (6\text{-}6)$$

Transition [6-4] can also be decomposed:

$$|\pi^- p\rangle = |1,-1;1/2,+1/2\rangle = \sqrt{1/3}|3/2,-1/2\rangle - \sqrt{2/3}|1/2,-1/2\rangle \quad (6\text{-}7)$$

$$|\pi^\circ n\rangle = |1,0;1/2,-1/2\rangle = \sqrt{2/3}|3/2,-1/2\rangle + \sqrt{1/3}|1/2,-1/2\rangle. \quad (6\text{-}8)$$

Combining Equations (6-5) and (6-6), and (6-7) and (6-8), and defining the isospin 3/2 and 1/2 amplitudes as A(I=3/2) and A(I=1/2), the two charge exchange transitions can be written:

$$\langle\pi^\circ p|\pi^+ n\rangle = \sqrt{2/9}A(I=3/2) - \sqrt{2/9}A(I=1/2) \quad (6\text{-}9)$$

$$\langle\pi^\circ n|\pi^- p\rangle = \sqrt{2/9}A(I=3/2) - \sqrt{2/9}A(I=1/2). \quad (6\text{-}10)$$

Upon decomposing the two-particle states into their I = 1/2, 3/2 components and constructing the transition amplitudes, transitions [6-1] and [6-4] are found to have I = 1/2 and I = 3/2 amplitudes of equal strength. As a result, the total transition amplitudes for reactions [6-1] and [6-4] are equal. Taking this together with the implications of time reversal symmetry, the squares of the amplitudes for all four charge exchange transitions are equal, hence only one probability characterizes all four transitions[6].

6.4 Summary

Based on previous π-N results, rates for the four intranuclear rescattering processes can be determined by comparing the deuterium and neon final state population fractions and angular distributions. Evidence for pion absorption and charge exchange, in the form of varying final state population fractions and charge illegal reaction states, have been presented in Chapter 5. These population fractions will form the basis for a statistical fit to determine the absorption and charge exchange rates.

The rates for elastic and inelastic rescattering are more difficult to determine. As suggested by Section 6.2, these processes can, in principle, be identified by examining pion production angles; examination of stub nuclear protons and broadening of the delta resonance may also help. That is, comparison of the forward and backward angle regions of the neon pion production angle distribution to the deuterium data may provide a measure of the elastic and inelastic rescattering rates. Also, reconstruction of the Δ system through π-p invariant mass combinations may provide an additional measure of the rescattering rates, since any degradation in the constituent pion's energy or direction of flight would widen the neon pπ invariant mass distribution about the delta mass relative to the deuterium distribution.

References

1. T.W.Jones, et al., Phys. Rev. Lett. 52, 720 (1984).

2. D.Ashery, et al., Phys. Rev. C23, 2173 (1981).

3. J. Bartlett, et al., ANL-HEP-PR-81-12, 91 (1981).

4. J.P.Albanese, et al., Nucl. Phys. A350, 301 (1980).

5. R.A.Freeman, G.A.Miller, and E.M.Henley, Nucl. Phys. A389, 457 (1982); M.B.Johnson and H.A.Bethe, Comments Nucl. Part. Phys. 8, 75 (1978).

6. I am indebted to Prof. G.Goldstein for clarifying this point.

CHAPTER 7

PION CHARGE EXCHANGE AND ABSORPTION

7.1 Introduction

As noted in the previous chapter, pion charge exchange and absorption intranuclear rescattering processes in ν_μ-neon interactions will alter the final state identity of these reactions. While these alterations are readily discerned in charge illegal final states (such as those listed in Table 5-3), pion charge exchange and absorption can also alter the relative populations among charge-legal final states from neutrino reactions in a nuclear medium. This chapter describes the determination of the charge exchange and absorption rates for neon. These rates are computed by matching the populations of weighted exclusive final state neon reaction channels to the populations of weighted deuterium final states using the absorption and charge exchange process probabilities as free parameters.

Section 7.2 tabulates the specific pion absorptive and charge exchange transitions which are used to fit the data. In listing these specific transitions, the assumption is made that each pion undergoes a single transformation or absorption. Higher order effects (e.g., a neutral pion scatters into a charged pion and subsequently is absorbed or re-exchanged into a neutral pion) are neglected.

The formulation of all first-order state-altering transitions as constraint equations for fitting data is described in Section 7.3. Results and interpretations of the analysis are also presented.

The exclusive quasi-elastic final state can be used to determine the probability of pion absorption. Section 7.4 discusses this analysis and presents a lower bound on the exclusive channel absorptive rate. Section 7.5 summarizes the chapter.

7.2 Charge Legal and Illegal Final States

Pion absorption can be characterized using one underlying transition probability (abs). As shown in the previous chapter, pion charge exchange can also be ascribed to one transition probability (cex). A table can then be composed which maps initial ν_μ-Ne topologies into charge legal and illegal final states. Table 7-1 lists nine observed, possibly rescattered, charge legal final states, and indicates the absorptive and charge exchange transitions which can cause various "initial" (non-rescattered) final states to end up in an observed final state.

To use the table, consider the transformation of an "initial" final state by the transitions listed. For example, the second entry in Table 7-1 is the initial state

$$\mu^-\pi^\circ\pi^\circ\pi^\circ p. \qquad (7\text{-}1)$$

By the absorption of two pions and charge exchange ($\pi^\circ \rightarrow \pi^+$), this state can be transformed within the target nucleus into the final observed state

TABLE 7-1

CHARGE-LEGAL FINAL STATES RESULTING FROM CHARGE EXCHANGE- AND PION ABSORPTION-ALTERED INITIAL STATES

Final State	Initial State	Rescattering Transition
$\mu^-\pi^+p$	$\mu^-\pi^+\pi^\circ\pi^\circ p$	(abs^2)
	$\mu^-\pi^\circ\pi^\circ\pi^\circ p$	$3(abs^2 \times cex)$
	$\mu^-\pi^+\pi^\circ\pi^\circ p$	$2(abs^2 \times cex)$
	$\mu^-\pi^+\pi^+\pi^-p$	$2(abs^2)$
	$\mu^-\pi^+\pi^-\pi^\circ p$	$(abs^2 \times cex)$
	$\mu^-\pi^+\pi^\circ p$	(abs)
	$\mu^-\pi^+\pi^\circ p$	$(abs \times cex)$
	$\mu^-\pi^\circ\pi^\circ p$	$2(abs \times cex)$
	$\mu^-\pi^+\pi^-p$	(abs)
	$\mu^-\pi^\circ p$	(cex)
	$\mu^-\pi^+p$	
$\mu^-\pi^+\pi^\circ p$	$\mu^-\pi^+\pi^-\pi^\circ p$	(abs)
	$\mu^-\pi^+\pi^-\pi^\circ p$	$(abs \times cex^2)$
	$\mu^-\pi^+\pi^-\pi^\circ p$	$(abs \times cex)$
	$\mu^-\pi^+\pi^+\pi^-p$	$2(abs \times cex)$
	$\mu^-\pi^+\pi^+\pi^-p$	$2(abs \times cex)$
	$\mu^-\pi^\circ\pi^\circ\pi^\circ p$	$6(abs \times cex)$
	$\mu^-p^+\pi^\circ\pi^\circ p$	$2(abs)$
	$\mu^-\pi^+\pi^\circ\pi^\circ p$	$2(abs \times cex)$
	$\mu^-\pi^+\pi^\circ\pi^\circ p$	$2(abs \times cex^2)$
	$\mu^-\pi^+\pi^-p$	(cex)
	$\mu^-\pi^+\pi^\circ p$	(cex^2)
	$\mu^-\pi^+\pi^\circ p$	
$\mu^-\pi^+\pi^+n$	$\mu^-\pi^+\pi^+\pi^\circ n$	(abs)
	$\mu^-\pi^+\pi^+\pi^\circ n$	$2(abs \times cex)$
	$\mu^-\pi^+\pi^+\pi^-n$	(abs)
	$\mu^-\pi^+\pi^\circ\pi^\circ n$	$2(abs \times cex)$
	$\mu^-\pi^+\pi^\circ\pi^\circ n$	$(abs \times cex^2)$
	$\mu^-\pi^+\pi^\circ n$	(cex)
	$\mu^-\pi^+\pi^+n$	
μ^-p	$\mu^-\pi^\circ\pi^\circ\pi^\circ p$	(abs^3)
	$\mu^-\pi^+\pi^\circ\pi^\circ p$	(abs^3)
	$\mu^-\pi^+\pi^-\pi^\circ p$	(abs^3)
	$\mu^-\pi^+\pi^+\pi^-p$	(abs^3)
	$\mu^-\pi^+\pi^\circ p$	(abs^2)
	$\mu^-\pi^\circ\pi^\circ p$	(abs^2)
	$\mu^-\pi^+\pi^-p$	(abs^2)
	$\mu^-\pi^+p$	(abs)
	$\mu^-\pi^\circ p$	(abs)
	$\mu^-\pi^+n$	(abs)
	μ^-p	

TABLE 7-1 (Continued)

Final State	Initial State	Rescattering Transition
$\mu^-\pi^\circ p$	$\mu^-\pi^\circ\pi^\circ\pi^\circ p$	$3(abs^2)$
	$\mu^-\pi^+\pi^\circ\pi^\circ p$	$2(abs^2)$
	$\mu^-\pi^+\pi^\circ\pi^\circ p$	$(abs^2 \times cex)$
	$\mu^-\pi^+\pi^-\pi^\circ p$	(abs^2)
	$\mu^-\pi^+\pi^-\pi^\circ p$	$(abs^2 \times cex)$
	$\mu^-\pi^+\pi^-\pi^\circ p$	$(abs^2 \times cex)$
	$\mu^-\pi^+\pi^+\pi^- p$	$2(abs^2 \times cex)$
	$\mu^-\pi^+\pi^+\pi^- p$	$(abs^2 \times cex)$
	$\mu^-\pi^\circ\pi^\circ p$	$2(abs)$
	$\mu^-\pi^+\pi^\circ p$	(abs)
	$\mu^-\pi^+\pi^\circ p$	$(abs \times cex)$
	$\mu^-\pi^+\pi^- p$	$(abs \times cex)$
	$\mu^-\pi^+\pi^- p$	$(abs \times cex)$
	$\mu^-\pi^+ p$	(cex)
	$\mu-\pi^\circ p$	
$\mu^-\pi^\circ\pi^\circ p$	$\mu^-\pi^\circ\pi^\circ\pi^\circ p$	$3(abs)$
	$\mu^-\pi^+\pi^\circ\pi^\circ p$	(abs)
	$\mu^-\pi^+\pi^\circ\pi^\circ p$	$2(abs \times cex)$
	$\mu^-\pi^+\pi^-\pi^\circ p$	$(abs \times cex)$
	$\mu^-\pi^+\pi^-\pi^\circ p$	$(abs \times cex^2)$
	$\mu^-\pi^+\pi^-\pi^\circ p$	$(abs \times cex)$
	$\mu^-\pi^+\pi^+\pi^- p$	$2(abs \times cex^2)$
	$\mu^-\pi^+\pi^+\pi^- p$	$2(abs \times cex^2)$
	$\mu^-\pi^+\pi^- p$	(cex^2)
	$\mu^-\pi^+\pi^\circ p$	(cex)
	$\mu^-\pi^\circ\pi^\circ p$	
$\mu^-\pi^+ n$	$\mu^-\pi^+\pi^\circ\pi^\circ n$	(abs^2)
	$\mu^-\pi^+\pi^\circ\pi^\circ n$	$2(abs^2 \times cex)$
	$\mu^-\pi^+\pi^+\pi^- n$	$2(abs^2)$
	$\mu^-\pi^+\pi^+\pi^\circ n$	$2(abs^2)$
	$\mu^-\pi^+\pi^+\pi^\circ n$	$(abs^2 \times cex)$
	$\mu^-\pi^+\pi^\circ n$	(abs)
	$\mu^-\pi^+\pi^\circ n$	$(abs \times cex)$
	$\mu^-\pi^+\pi^+ n$	$2(abs)$
	$\mu^-\pi^+ n$	
$\mu^-\pi^+\pi^\circ n$	$\mu^-\pi^+\pi^\circ\pi^\circ n$	$2(abs)$
	$\mu^-\pi^+\pi^\circ\pi^\circ n$	$2(abs \times cex)$
	$\mu^-\pi^+\pi^+\pi^\circ n$	$2(abs)$
	$\mu^-\pi^+\pi^+\pi^\circ n$	$2(abs \times cex)$
	$\mu^-\pi^+\pi^+\pi^\circ n$	$2(abs \times cex^2)$
	$\mu^-\pi^+\pi^+\pi^- n$	$2(abs \times cex)$
	$\mu^-\pi^+\pi^+\pi^- n$	$2(abs \times cex)$
	$\mu^-\pi^+\pi^+ n$	$2(cex)$
	$\mu^-\pi^+\pi^\circ n$	

TABLE 7-1 (Continued)

Final State	Initial State	Rescattering Transition
$\mu^-\pi^+\pi^-p$	$\mu^-\pi^\circ\pi^\circ\pi^\circ p$	$6(\text{abs} \times \text{cex}^2)$
	$\mu^-\pi^+\pi^\circ\pi^\circ p$	$2(\text{abs} \times \text{cex})$
	$\mu^-\pi^+\pi^\circ\pi^\circ p$	$2(\text{abs} \times \text{cex}^2)$
	$\mu^-\pi^+\pi^+\pi^-p$	$2(\text{abs})$
	$\mu^-\pi^+\pi^-\pi^\circ p$	(abs)
	$\mu^-\pi^+\pi^-\pi^\circ p$	$(\text{abs} \times \text{cex})$
	$\mu^-\pi^+\pi^-\pi^\circ p$	$(\text{abs} \times \text{cex})$
	$\mu^-\pi^\circ\pi^\circ p$	(cex^2)
	$\mu^-\pi^+\pi^\circ p$	(cex)
	$\mu^-\pi^+\pi^-p$	

$$\mu^- \pi^+ p. \qquad (7\text{-}2)$$

This transition, written in shorthand as

$$abs^2 \times cex, \qquad (7\text{-}3)$$

can occur in any of three possible ways due to the three initial π^os and therefore has a multiplicative factor before it in the Rescattering Transition column.

Table 7-1 assumes that only one, two, or three pion initial states can be corrupted so as to yield apparent zero, one, or two pion final states. Furthermore, the assumption is made that an initial state pion can undergo a single transition (charge exchange or absorption) or remain unperturbed; that is, a charge exchanged pion cannot subsequently be absorbed. Transitions involving a pion reacting with more than one nucleon are neglected.

In addition to charge legal final states, Table 5-3 lists one single-pion charge-illegal final state. Since this state is clearly the result of either charge exchange or pion absorption, Table 7-2 lists the initial states and transitions which could have produced the final state $\mu^- \pi^- p$.

7.3 Data Fitting

From phenomenological charge exchange and absorptive transitions of Tables 7-1 and 7-2, constraint equations can be formulated for the purpose of determining overall process rates. These constraint equations treat charge exchange and absorptive transition probabilities as variables

TABLE 7-2

CHARGE-ILLEGAL FINAL STATE RESULTING FROM CHARGE EXCHANGE- AND PION ABSORPTION-ALTERED INITIAL STATES

Final State	Initial State	Rescattering Transition
$\mu^-\pi^-p$	$\mu^-\pi^\circ\pi^\circ\pi^\circ p$	$3(abs^2 \times cex)$
	$\mu^-\pi^+\pi^\circ\pi^\circ p$	$(abs^2 \times cex)$
	$\mu^-\pi^+\pi^-\pi^\circ p$	(abs^2)
	$\mu^-\pi^+\pi^-\pi^\circ p$	$(abs^2 \times cex)$
	$\mu^-\pi^+\pi^+\pi^- p$	(abs^2)
	$\mu^-\pi^\circ\pi^\circ p$	$2(abs \times cex)$
	$\mu^-\pi^+\pi^\circ p$	$(abs \times cex)$
	$\mu^-\pi^+\pi^- p$	(abs)
	$\mu^-\pi^\circ p$	(cex)

to be fitted. Factors multiplying these variables are determined from the initial state and are listed in Table 7-3.

To illustrate our technique, the first three processes of Table 7-1 are parameterized below:

Phenomenology		Parameterization	
$\mu^-\pi^+\pi^\circ\pi^\circ p$	(abs)	pi3 x abs	
$\mu^-\pi^\circ\pi^\circ\pi^\circ p$	$3(abs^2 \times cex)$	$3 \times pi3 \times abs^2 \times cex$	(7-4)
$\mu^-\pi^+\pi^\circ\pi^\circ p$	$2(abs^2 \times cex)$	$2 \times pi3 \times abs^2 \times cex$	
Subtotal		$pi3 \times (5 \times abs^2 \times cex + abs)$	

All transitions contributing to a final state are parameterized and summed to arrive at one constraint equation. Since Table 7-1 and 7-2 jointly yield ten constraint equations in two variables, the problem of solving for the two process rates appears to be overdetermined. These ten equations are listed in Table 7-4.

Table 7-5 lists the ten relevant reaction channel population fractions for the deuterium and neon data as taken from Tables 5-2 and 5-3. Unfortunately, two considerations with regard to data quality require that half of the constraint equations be disregarded. Firstly, we require that the equations include some 3C final states. Secondly, we require that the final state being constrained must represent a signifcant fraction of the data. With these two criteria imposed, there remain five observed final states to be fitted:

TABLE 7-3

DEFINITION OF MULTIPLICATIVE FACTORS
FOR CONSTRAINING EQUATIONS

Three pion population fraction	pi3
Two pion population fraction	pi2
Pi-plus proton population fraction	pip
Pi-zero proton population fraction	pi0p
Pi-plus neutron population fraction	pin

TABLE 7-4

TRANSLATED CHARGE-LEGAL AND CHARGE-ILLEGAL
FINAL STATE CONSTRAINT EQUATIONS

Final State	Constraint Equation
$\mu^-\pi^+p$	$pi3(6abs^2 \times cex + 4abs^2) + pi2(3abs \times cex + 2abs) + (pi0p \times cex) + pip(1 - cex - abs)$
$\mu^-\pi^+\pi^\circ p$	$pi3(3abs \times cex^2 + 13abs \times cex + 3abs) + pi2(cex + cex^2) + pi2(1 - 2abs - abs^2 - 2cex - cex^2 - 2abs \times cex)$
$\mu^-\pi^+\pi^+n$	$pi3(abs \times cex^2 + 4abs \times cex + 2abs) + (pi2 \times cex) + pi2(1 - 2abs - abs^2 - 2cex - cex^2 - 2abs \times cex)$
μ^-p	$(pi3 \times 4abs^3) + (pi2 \times 3abs^2) + abs(pip + pin + pi0p) + 0.49^*$
$\mu^-\pi^\circ p$	$pi3(6abs^2 \times cex + 6abs^2) + pi2(3abs \times cex + 3abs) + (pi \times cex) + pi0p(1 - cex - abs)$
$\mu^-\pi^\circ\pi^\circ p$	$pi3(5abs \times cex^2 + 6abs \times cex + 4abs) + pi2(cex^2 + cex) + pi2(1 - 2abs - abs^2 - 2cex - cex^2 - 2abs \times cex)$
$\mu^-\pi^+n$	$pi3(3abs^2 \times cex + 5abs^2) + pi2(abs \times cex + 3abs) + pip(1 - abs - cex)$
$\mu^-\pi^+\pi^\circ n$	$pi3(2abs \times cex^2 + 8abs \times cex + 4abs) + (pi2 \times 2cex) + pi2(1 - 2abs - abs^2 - 2cex - cex^2 - 2 abs \times cex)$
$\mu^-\pi^+\pi^-p$	$pi3(8abs \times cex^2 + 4abs \times cex + 3 abs) + pi2(cex + cex^2) + pi2(1 - 2abs - abs^2 - 2cex - cex^2 - 2abs \times cex)$
$\mu^-\pi^-p$	$pi3(6abs^2 \times cex + 2abs^2) + pi2(3abs \times cex + abs) + (pi0p \times cex)$

*The additive factor of 0.49 reflects the deuterium reaction channel population fraction.

TABLE 7-5

DEUTERIUM AND NEON DATA WEIGHTED TO ATMOSPHERIC: FRACTIONAL POPULATION DISTRIBUTION

Reaction	Fractional Population Deuterium	Neon
$\nu p \rightarrow \mu^- \pi^+ p$	0.19 ± 0.02	0.14 ± 0.02
$\nu p \rightarrow \mu^- \pi^+ (\ell\pi^\circ) p$, $\ell \geq 1$	0.01 ± 0.01	0.02 ± 0.01
$\nu p \rightarrow \mu^- \pi^+ \pi^+ (m\pi^\circ) n$, $m \geq 0$	0.01 ± 0.01	0.02 ± 0.01
$\nu n \rightarrow \mu^- p$	0.49 ± 0.03	0.58 ± 0.02
$\nu n \rightarrow \mu^- \pi^\circ p$	0.09 ± 0.01	0.05 ± 0.02
$\nu n \rightarrow \mu^- \pi^\circ \pi^\circ p$	0.01 ± 0.01	0.04 ± 0.02
$\nu n \rightarrow \mu^- \pi^+ n$	0.14 ± 0.02	0.07 ± 0.01
$\nu n \rightarrow \mu^- \pi^+ (\ell\pi^\circ) n$	-	0.01 ± 0.01
$\nu n \rightarrow \mu^- \pi^- \pi^+ p$	0.02 ± 0.01	0.03 ± 0.01
$\nu N \rightarrow \mu^- +$ (Q=-1,+3,+4)	-	0.03 ± 0.01
$\nu p \rightarrow \mu^- \pi^- p$	-	0.01 ± 0.01

$$\mu^-\pi^+p$$

$$\mu^-p$$

$$\mu^-\pi^+\pi^+n \qquad (7\text{-}5)$$

$$\mu^-\pi^-\pi^+$$

$$\mu^-\pi^-p.$$

The constraining equations for these five final states, together with the data listed in Table 7-5, define five straight-line "trajectories" of possible (abs, cex) values as depicted in Figure 7-1. The constraint equations for the five selected final states were combined in a chi-squared fit which was carried out using the MINUIT fitting program. Using deuterium data values for initial state population fractions and associated errors, the MINUIT program computed a best fit for the absorptive and charge exchange rates. The fit yielded 0.23 ± 0.08 for absorption and 0.05 ± 0.09 for charge exchange. The fitted values and their associated errors are also shown in Figure 7-1.

Bounds on the charge exchange and absorption rates can be obtained by using the ratio of these rates as determined from the cross-section decomposition of experimental data of Figure 6-2b). The ratio of pion absorption to charge exchange, R, as a function of energy was computed and compared with the deuterium π^+ and π^- inclusive energy distributions on a bin-by-bin basis. In this way, an "average" ratio value for π^+, $R_{\pi+}$, is computed to be 2.56 ± 0.17, and for π^-, $R_{\pi-}$, a value of 1.85 ± 0.17 is obtained. The values are also shown in Figure 7-1. Utilizing the constraining equations, the MINUIT fit result, and the cross-section ratio values for pion charge exchange and absorption, the average rate of pion

FIGURE 7-1

ABSORPTION vs CHARGE EXCHANGE RATES

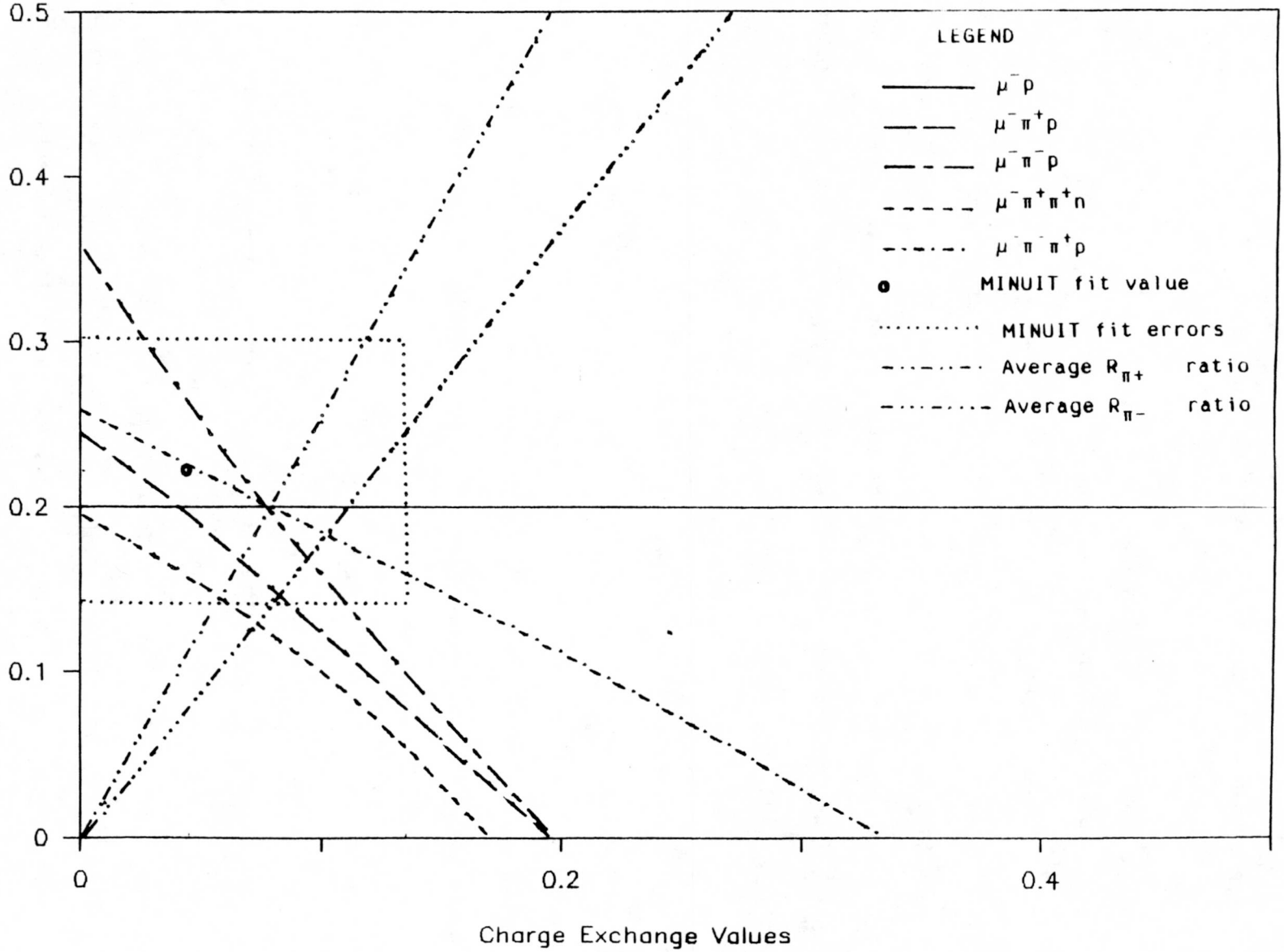

absorption in neon is between 0.15 and 0.23, and the average rate of pion charge exchange in neon is between 0.04 and 0.10.

7.4 Pion Absorption in the Quasi-Elastic Final State

The observed final state

$$\nu Ne \rightarrow \mu^- p \qquad (7\text{-}6)$$

can be used to determine the amount of pion absorption in neon. As seen in Table 7-1, this final state reaction includes no charge exchange transitions, thus any difference between the deuterium and neon kinematic distributions would be indicative of pion absorption.

To search for such differences, we note that for quasi-elastic events, the proton-muon opening angle, θ, is peaked about 90 degrees. This can be seen in Figure 7-2 where the deuterium and neon $\cos\theta$ distributions have been normalized to the same area. While the deuterium data shows the expected peak at $\cos\theta = 0$, the neon distribution is more isotropic, suggesting non-quasi-elastic production; i.e., pion absorption.

Figure 7-3 shows the $\cos\theta$ distribution for single pion production in deuterium (π^+ and π°) and in neon (π^+ only). These deuterium and neon distributions are more isotropic than the deuterium quasi-elastic distribution and support the idea that the neon quasi-elastic sample contains examples of pion absorption. However, the nucleons within neon are also subject to Fermi motion; this effect can also serve to smear the $\cos\theta$ distribution. This latter effect is examined by comparing the proton-muon opening angle distributions for deuterium quasi-elastic events with and

FIGURE 7-2

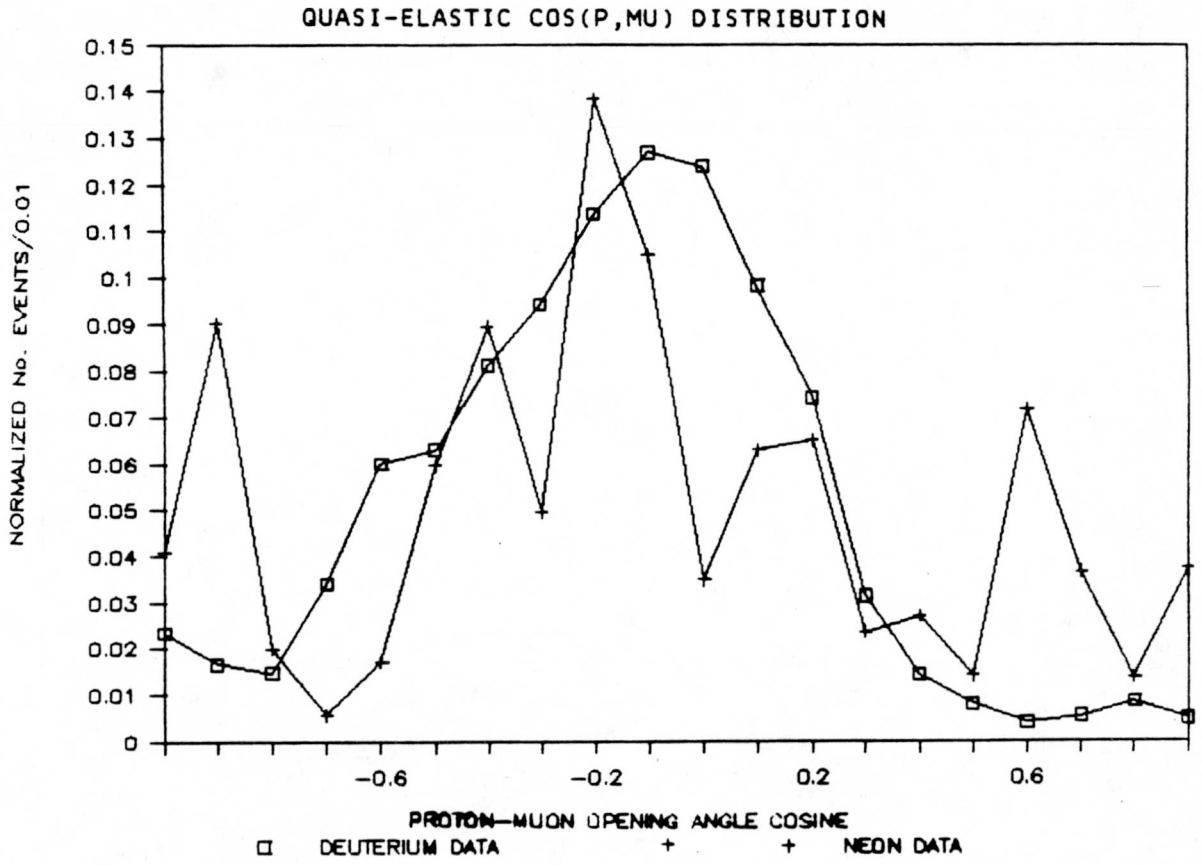
QUASI-ELASTIC COS(P,MU) DISTRIBUTION
NORMALIZED No. EVENTS/0.01
0.15
0.14
0.13
0.12
0.11
0.1
0.09
0.08
0.07
0.06
0.05
0.04
0.03
0.02
0.01
0
-0.6
-0.2
0.2
0.6
PROTON-MUON OPENING ANGLE COSINE
DEUTERIUM DATA
NEON DATA

FIGURE 7-3

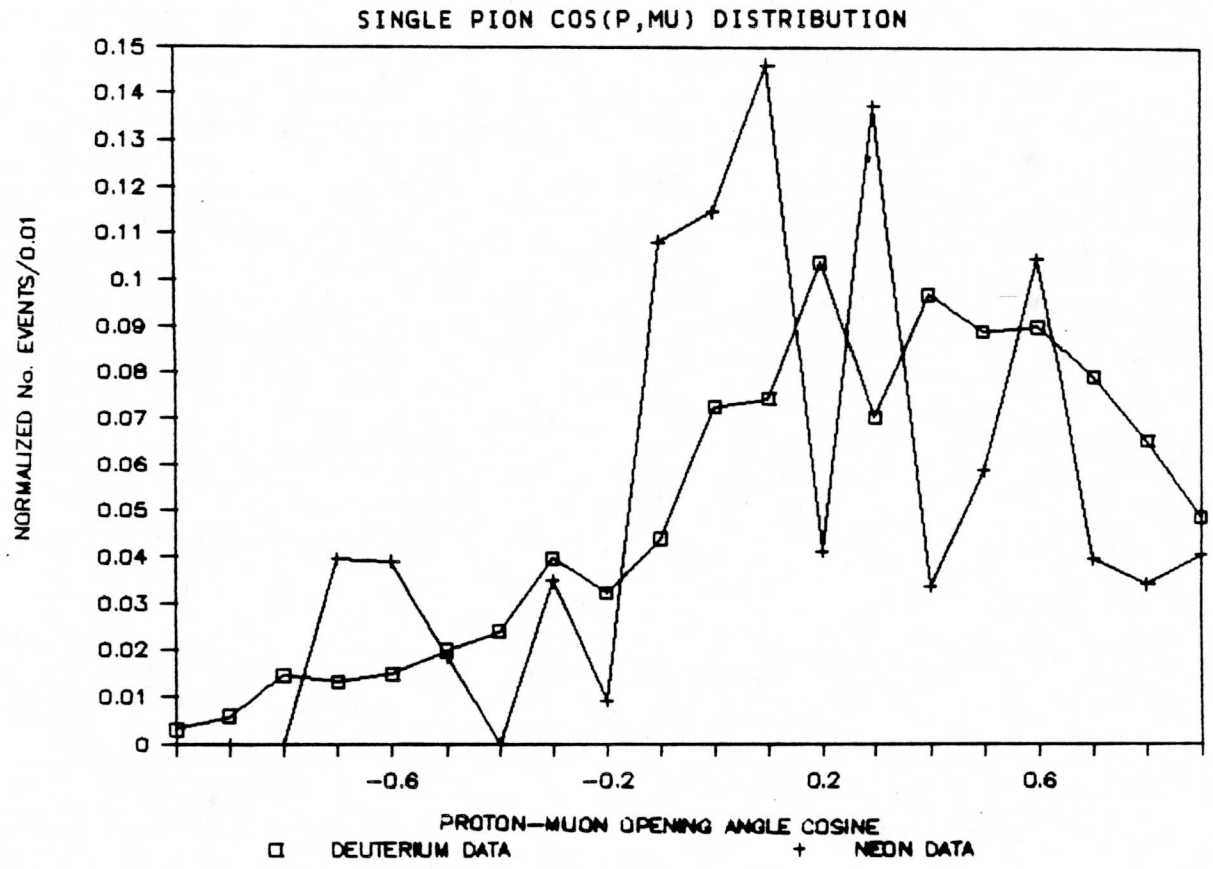
SINGLE PION COS(P,MU) DISTRIBUTION
NORMALIZED No. EVENTS/0.01
0.15
0.14
0.13
0.12
0.11
0.1
0.09
0.08
0.07
0.06
0.05
0.04
0.03
0.02
0.01
0
-0.6
-0.2
0.2
0.6
PROTON-MUON OPENING ANGLE COSINE
DEUTERIUM DATA
NEON DATA

without a visible spectator proton. These distributions, area normalized, are shown in Figure 7-4. The events with a visible spectator proton, that is, events with Fermi motion more nearly approximating that within neon nuclei, have a more isotropic $\cos\theta$ distribution than do events without a visible spectator proton.

As a result of limited statistics and competing effects (Fermi motion and pion production), the opening angle distribution of the neon quasi-elastic channel cannot provide an unambiguous estimate for the exclusive pion absorption rate. If Fermi smearing is ignored, then a crude absorption estimate is obtained by comparing the number of neon quasi-elastic events outside the region $|\cos\theta| > 0.5$ to the number within this area. In effect, we ascribe all the events outside the $\cos\theta = 0$ region to pion absorption and ignore the effect of Fermi smearing in these regions. Furthermore, the method assumes that all the events near the $\cos\theta = 0$ region are quasi-elastic, an incorrect assumption as can be seen from Figure 7-4. Using this crude method, a value of 0.33 ± 0.14 is deduced for the rate of pion absorption in the neon quasi-elastic channel. This value should be regarded as an upper bound on the true pion absorption rate.

7.5 Summary

To determine the rates of pion absorption and pion charge exchange within the nucleus, we have "mapped" the final state populations of the deuterium sample to the populations observed with neon targets. Starting with a list of legal initial states for neon, we showed how these states can

FIGURE 7-4

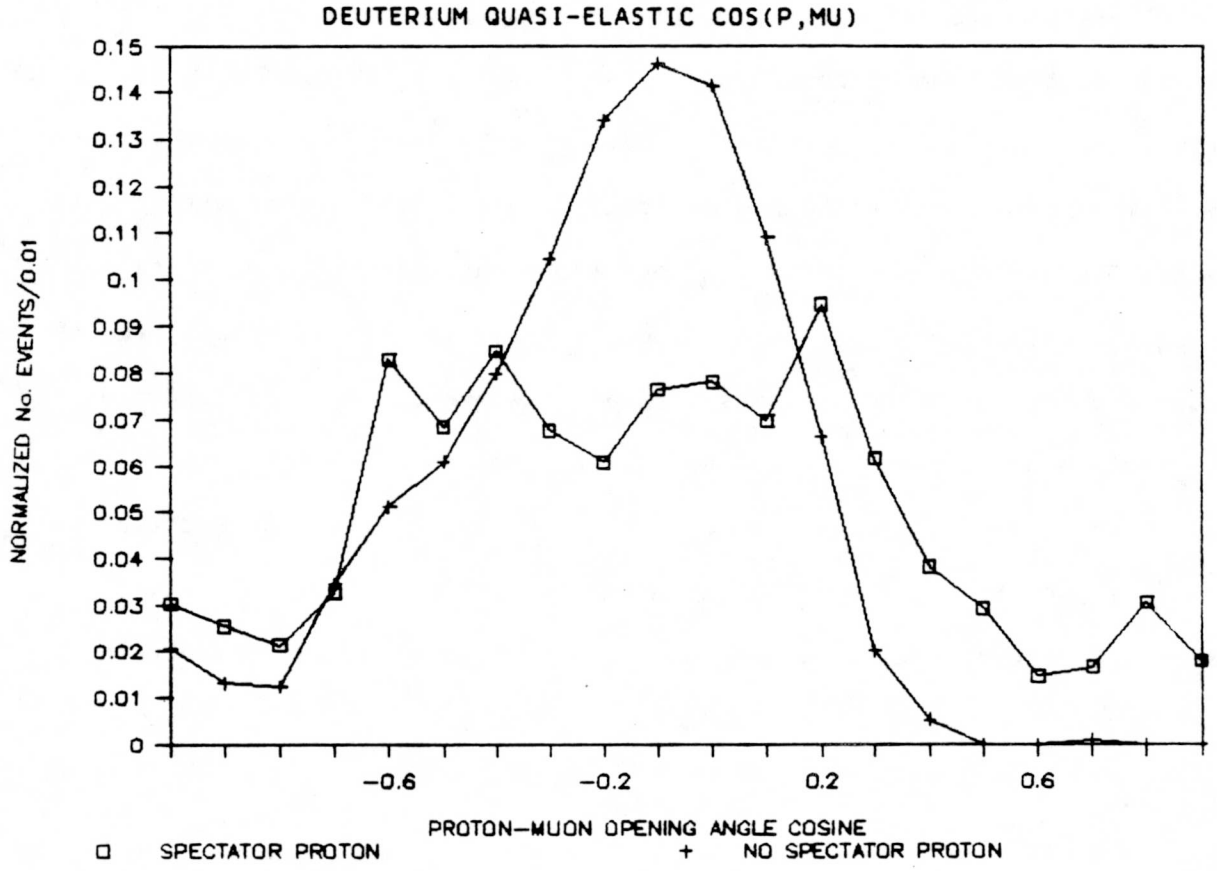
DEUTERIUM QUASI-ELASTIC COS(P,MU)
NORMALIZED No. EVENTS/0.01
0.15
0.14
0.13
0.12
0.11
0.1
0.09
0.08
0.07
0.06
0.05
0.04
0.03
0.02
0.01
0
-0.6
-0.2
0.2
0.6
PROTON-MUON OPENING ANGLE COSINE
□ SPECTATOR PROTON
+ NO SPECTATOR PROTON

be transformed into charge legal and illegal final states via the charge exchange and absorptive processes. Constraint equations were derived from these process models using deuterium reaction channel population fractions for data values. These constraint equations were plotted using deuterium and neon data values. In addition, a chi-squared fit of the data was made using the MINUIT fitting program. The fit resulted in values of 0.23 ± 0.08 and 0.05 ± 0.09 for the pion absorptive and charge exchange process rates, respectively.

Bounds on the charge exchange and absorption rates were also obtained by decomposing the pion cross-section into its scattering components. The ratio of pion absorption to charge exchange as a function of pion momentum was then computed and compared with the deuterium charged pion distributions on a bin-by-bin basis. This yielded a momentum averaged ratio (abs/cex) of 2.56 ± 0.17 for π^+s and 1.85 ± 0.17 for π^-s. Using the constraining equations, the MINUIT fit result, and the cross-section ratio values, the average rate of pion absorption in neon is between 0.15 and 0.23, and the average rate for pion charge exchange in neon is between 0.04 and 0.10.

A crude check of the neon pion absorption rate was extracted from the quasi-elastic final state. With comparison of the proton-muon opening angle distributions for both data sets, the neon distribution appears to be more isotropic than the deuterium distribution. This isotropy may be caused by single pion production (and subsequent absorption) in neon, or it may be due to Fermi motion within the more extensive neon nucleus. Assuming the difference between the deuterium and neon opening angle distributions are

caused solely by pion absorption and ignoring Fermi motion effects,a crude estimate of the pion absorption rate in the neon quasi-elastic channel is 0.33 ± 0.14. The neon data shows evidence for pion absorption or charge exchange occurring in 19 to 33 percent of all ν_μNe interactions, with absorption occurring approximately 4.5 times more frequently than charge exchange.

References

1. J.Bartlett, et al., ANL-HEP-PR-81-12, 91 (1981).

2. D.Ashery, et al., Phys. Rev. C23, 2173 (1981).

CHAPTER 8

INELASTIC INTRANUCLEAR PION RESCATTERING

8.1 Introduction

Having examined intranuclear pion absorption and charge exchange, we now consider inelastic and elastic scattering within the neon nucleus. The signatures for these latter processes are harder to resolve than are those of pion absorption and charge exchange; examination of pion, proton, and delta resonance kinematic distributions is required. By comparing the (weighted) neon to deuterium distributions, the effects of pion inelastic and elastic rescattering in nucleon decay experiments can (hopefully) be estimated, or at least constrained.

The effects of inelastic and elastic rescattering are analysed by comparing the momentum and production angle distributions for charged pions in the two ν_μ data sets. Section 8-2 examines the inclusive distribution while Section 8.3 examines exclusive channel distributions. These comparisons of observed final state pion distributions provide information about pion reinteraction in the two distinctly different nuclear environments. Section 8.4 summarizes the chapter.

8.2 Inclusive Pion Distributions

Inelastic and elastic scattering are expected to have different effects on final state pions. Inelastically scattered pions undergo momentum degradation as well as change in direction, whereas elastically scattered pions suffer only mild angular deflections. Thus, while both processes may result in an angular deflection, only inelastic scattering can alter the pion momentum distribution. The effects of these processes on pion kinematics can in principle be discerned by comparing distributions of the neon ν_μ-π angle, θ, and of the pion momentum, to the corresponding distributions in deuterium. Since pion inelastic rescattering, as opposed to elastic rescattering, may extensively alter neutrino final states, delineation of rates for the former process is of greater concern to nucleon decay searches - and to this Thesis.

Kinematic signatures for pion inelastic rescattering are, however, affected by pion absorption. As seen in Figure 6-2b), pion intranuclear absorption is momentum-dependent, with the greatest amount of absorption occurring around 300 MeV/c. Thus, the absorption process preferentially depletes low momentum pions. Inelastic rescattering on the other hand is roughly momentum-independent, and it can be expected to degrade higher momentum pions into the (depleted) low momentum regions.

A complete comparison of pions produced in the two data sets would include neutral as well as charged pions. Unfortunately, pi-zeros were treated differently in the two data sets during the initial data reduction due to differences in the radiation lengths of the two bubble chamber fills.

Since the neon events are not kinematically fitted, a π^o is observed only if two observed photons combine to form an invariant mass of $80 < m(\gamma\gamma) < 160$ MeV/c^2 during data analysis. Conversely, initial analysis of the deuterium data required kinematical fitting of all events. A large population of the fits attempted included zero-constraint fits with a final state π^o. As reported in Chapter 3, many of these fits were removed in favor of three-constraint topologies. Because of these differences in the treatment of neutral pions in the two data sets, comparison of the D- and Ne-produced π^os is dominated by uncertainties and has been found to be uninformative.

However, such problems do not arise with the charged pions. For both data sets, each event receives a weight which reflects the relative probability that the event's reconstructed neutrino energy occurs in an atmospheric neutrino spectrum. After atmospheric flux weighting, we have 1446 weighted events in the deuterium data and 524 weighted events in the neon sample. As shown in Chapters 5, 6, and 7, normalization of the total event populations to each other reveals channel-to-channel population differences; these presumably originate with absorption and charge exchange processes. On the other hand, differences between shapes of kinematical distributions extracted from the two data sets (which may reflect pion inelastic and elastic rescattering) are revealed by area-normalizing distributions to be compared. To facilitate our pion inelastic rescattering analysis, the distributions in the following sections are normalized to their respective total weighted event populations. This normalization, refered to as Data Set Normalization, allows both channel-to-channel population differences and shape differences in kinematic distributions to

Since the neon events are not kinematically fitted, a π° is observed only if two observed photons combine to form an invariant mass of $80 < m(\gamma\gamma) < 160$ MeV/c^2 during data analysis. Conversely, initial analysis of the deuterium data required kinematical fitting of all events. A large population of the fits attempted included zero-constraint fits with a final state π°. As reported in Chapter 3, many of these fits were removed in favor of three-constraint topologies. Because of these differences in the treatment of neutral pions in the two data sets, comparison of the D- and Ne-produced π°s is dominated by uncertainties and has been found to be uninformative.

However, such problems do not arise with the charged pions. For both data sets, each event receives a weight which reflects the relative probability that the event's reconstructed neutrino energy occurs in an atmospheric neutrino spectrum. After atmospheric flux weighting, we have 1446 weighted events in the deuterium data and 524 weighted events in the neon sample. As shown in Chapters 5, 6, and 7, normalization of the total event populations to each other reveals channel-to-channel population differences; these presumably originate with absorption and charge exchange processes. On the other hand, differences between shapes of kinematical distributions extracted from the two data sets (which may reflect pion inelastic and elastic rescattering) are revealed by area-normalizing comparative distributions. To facilitate our pion inelastic rescattering analysis, the distributions in the following sections are normalized to their respective total weighted event populations. This normalization, refered to as Data Set Normalization, allows both channel-to-channel population differences and shape differences in kinematic distributions to

be displayed. For distributions normalized in this manner, differences in area reflect channel population differences, while distribution shape differences indicate kinematic variances.

The inclusive charged pion momentum distributions are shown in Figures 8-1. (For visual reference, the momentum-dependent pion-iron total cross section is also indicated in these figures.) In these distributions, each pion is represented by its complete events weight including processing and atmospheric flux weighting. As a result of the momentum dependence of pion absorption, the pion momentum distributions should not "match" in shape in the absence of inelastic rescattering. With inelastic rescattering only, the pion momentum distribution for neon nuclei should be "slower" than the pion momentum distribution from deuterium data. Thus the close shape match in the inclusive π^+ distribution (Figure 8-1a), occurring in the known presence of pion absorption, is consistent with the occurrence of inelastic intranuclear rescattering within the neon nucleus.

As a means to examine kinematic distributions quantitatively, we introduce the fraction $f_p(\pi^{\pm})$ as the number of pions having momenta below 300 MeV/c divided by the total weighted number of $\pi^{\pm}$s in the distribution. This fraction is to be specified separately for the (atmospheric flux weighted) ν_μ-D and ν_μ-Ne events samples. For inclusive pions, each fraction is normalized to the total weighted pion population. For final state π^+ mesons from interactions in deuterium, this fraction is found to be $f_p^D(\pi^+_{INC}) = 0.45 \pm 0.03$. For π^+ mesons from neon interactions, $f_p^{Ne}(\pi^+_{INC}) = 0.47 \pm 0.05$. Hereafter, we will refer to these distribution measures f_p as the "low momentum fractions".

FIGURE 8-1a

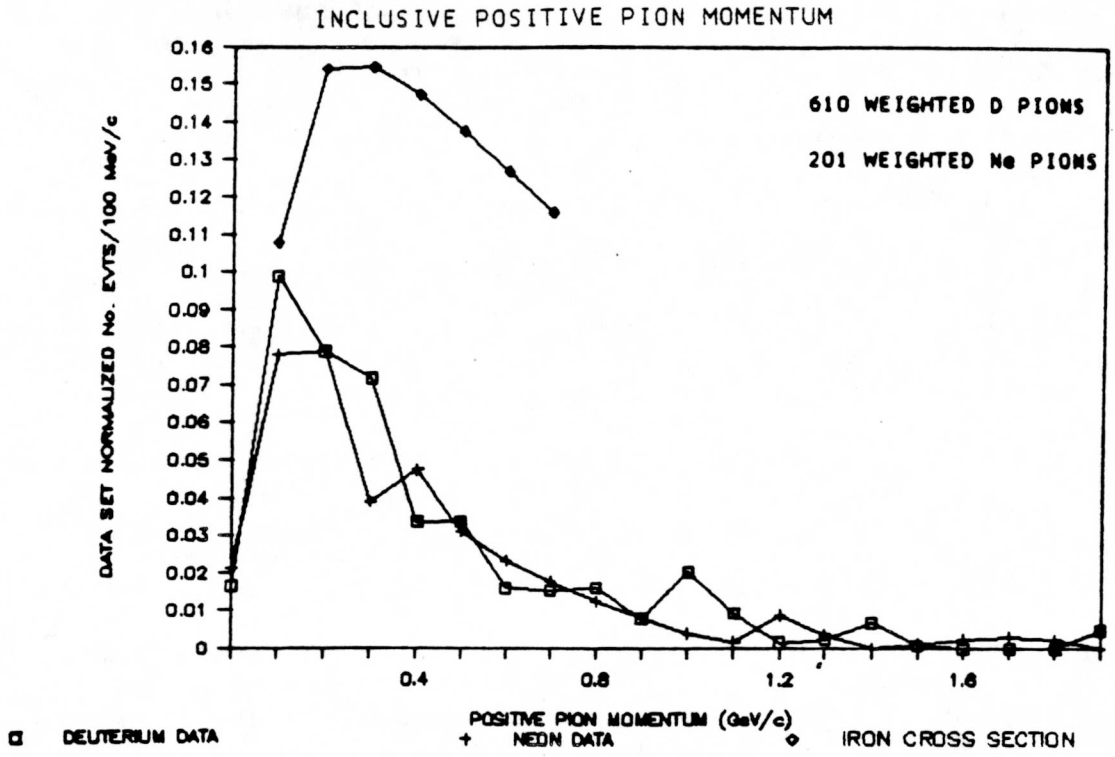

FIGURE 8-1b

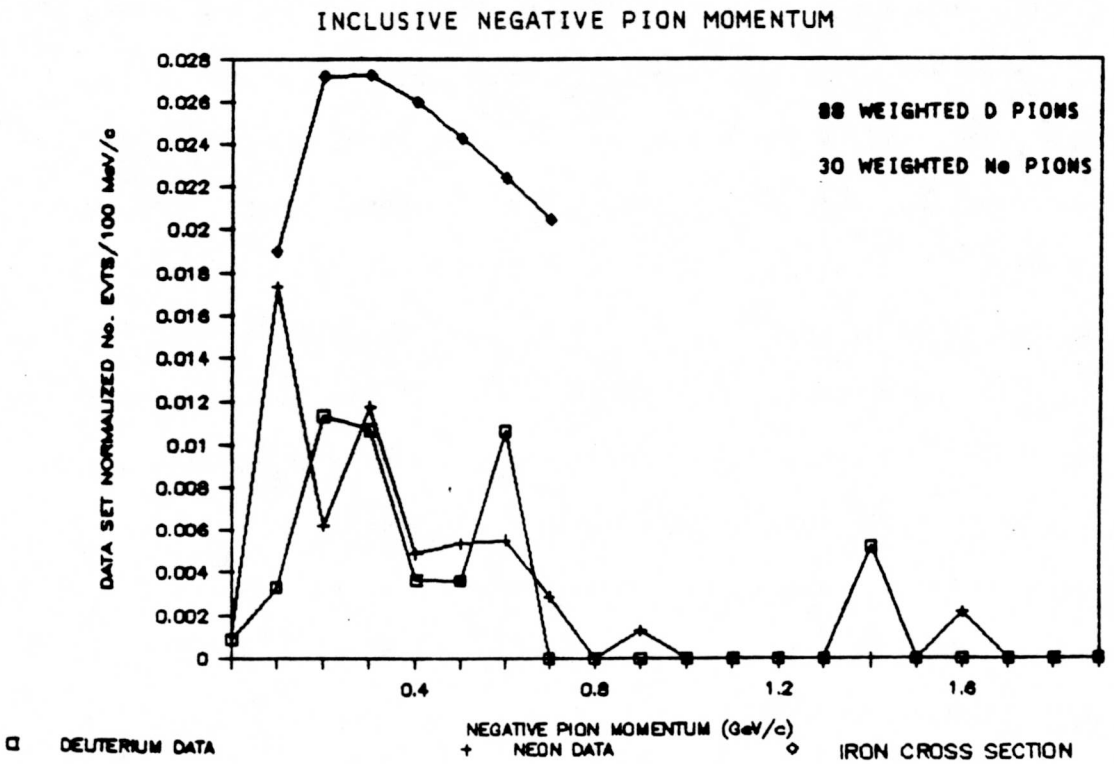

Interpretation of the inclusive π^- distribution is complicated by limited statistics resulting from the low neutrino energy and the double pion production threshold. However, as with the inclusive π^+ momentum distribution, Figure 8-1b) shows no dramatic shape differences, which is consistent with the presence of inelastic rescattering. For inclusive π^- mesons, the fractions of pions having momenta below 300 MeV/c are $f_p^{Ne}(\pi^-_{INC})$ = 0.42 ± 0.12, to be compared with $f_p^D(\pi^-_{INC})$ = 0.32 ± 0.05. These low momentum fractions indicate an excess Δ_p = 0.10 ± 0.13 of low momentum π^- mesons in the interactions in neon.

The inclusive pion production cosine distributions are shown in Figures 8-2 for positive and for negative pions. As with the momentum distributions, the production angle distributions represent each pion by its complete event weight. The distributions are subsequently Data Set Normalized to reveal both channel-to-channel population and kinematic differences. The deuterium to neon comparison of the π^+ cosine distribution (Figure 8-2a) shows little difference in the profiles of the two data sets. However, differences are apparent in the π^- cosine distributions.

As noted in Chapter 6, excessive backward scattering is evidence for inelastic rescattering. A lower bound on the amount of inelastic rescattering can be estimated by comparing the fraction of pions in each data set data set with $\cos\theta < 0.0$; i.e., in the backward hemisphere. These "backscatter fractions" are $f_\theta^D(\pi^+_{INC})$ = 0.17 ± 0.02 and $f_\theta^D(\pi^-_{INC})$ = 0.10 ± 0.03 for the deuterium inclusive π^+ and π^- distributions, and $f_\theta^{Ne}(\pi^+_{INC})$ = 0.20 ± 0.03 and $f_\theta^{Ne}(\pi^-_{INC})$ = 0.22 ± 0.01 for the neon inclusive π^+ and π^-

FIGURE 8-2a

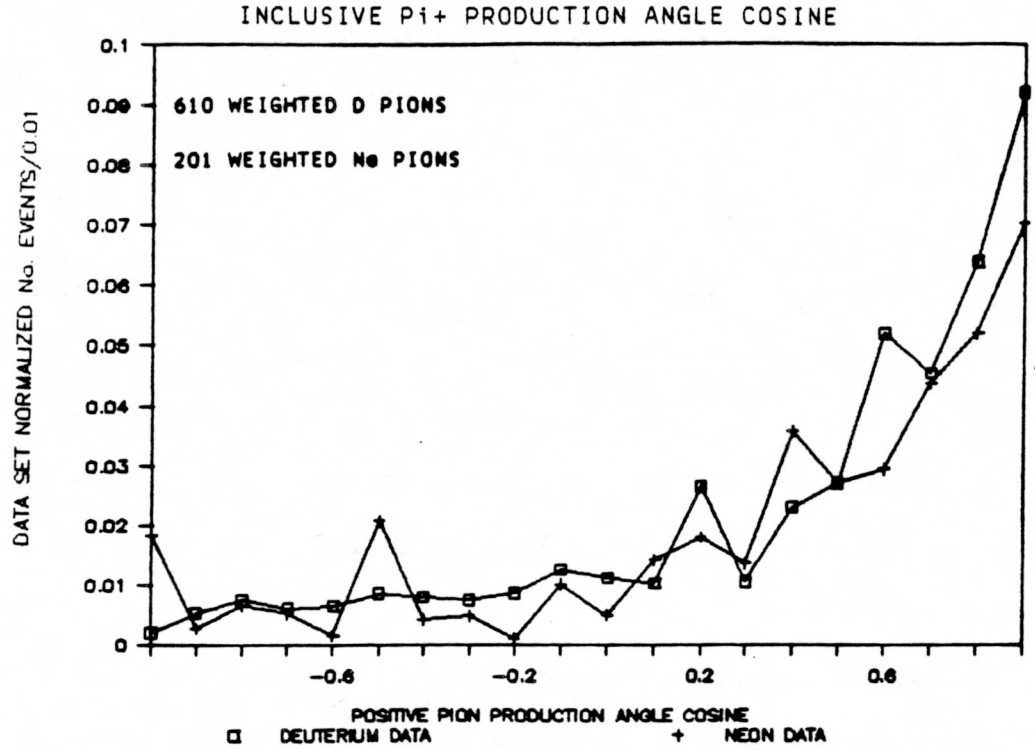

FIGURE 8-2b

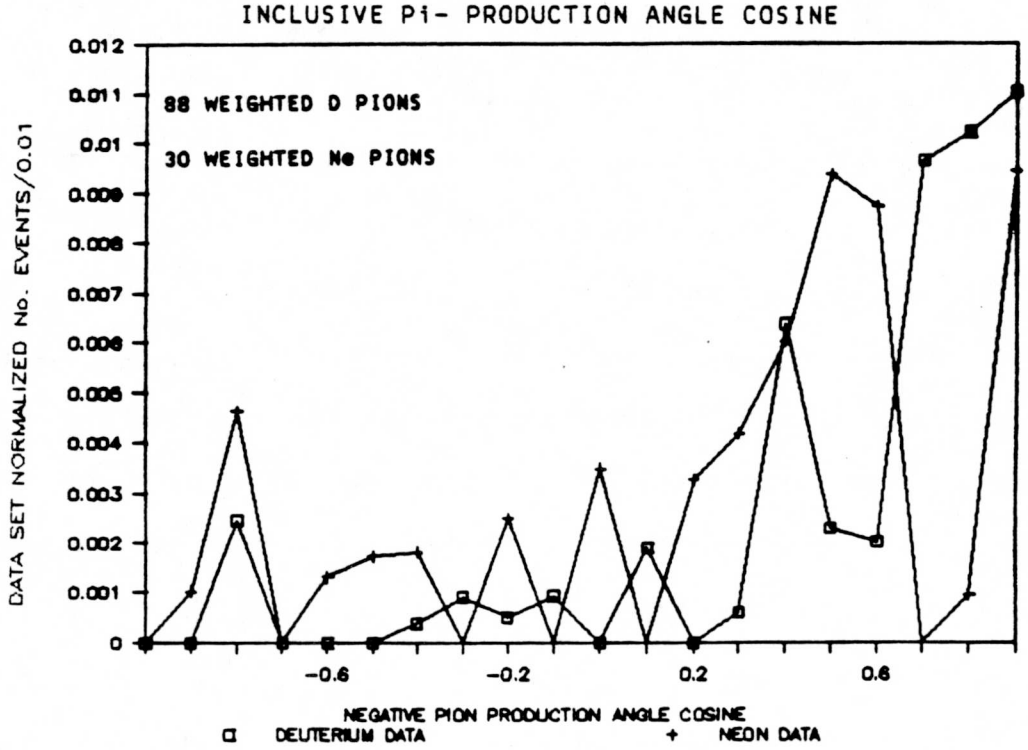

distributions. While the (weighted) deuterium and neon pion samples have similar fractions for the backscattered π^+ mesons, the neon backscatter fraction for π^- mesons exceeds the corresponding fraction in deuterium by $\Delta_\theta = 0.12 \pm 0.03$.

Since muons are not strongly interacting, their distributions are unaffected by intranuclear rescattering. Consequently, they provide a nonrescattering calibration for interpreting the low momentum and backscatter fractions which we use to characterize pion production. These fractions are $f_p^D(\mu^-_{INC}) = 0.43 \pm 0.02$ and $f_\theta^D(\mu^-_{INC}) = 0.12 \pm 0.01$ for the deuterium interactions, and $f_p^{Ne}(\mu^-_{INC}) = 0.43 \pm 0.02$ and $f_\theta^{Ne}(\mu^-_{INC}) = 0.06 \pm 0.01$ for the neon interactions. The values indicate no difference between the neon and deuterium low momentum fractions for muons, while a six percent variation is observed in the muon backscatter fractions from the two sample. This implies that an overall uncertainty of 0.06 should be applied to interpretation of f_θ differences, due to Fermi smearing.

While inelastically rescattered pions suffer both momentum degradation and angular deflection, complete determination of an inelastic rescattering rate would require assessing the number of pions (charged and neutral) which rescatter into the four kinematic regions:

i) $p_\pi > 300$ MeV/c and $\cos\theta > 0.0$,

ii) $p_\pi > 300$ MeV/c and $\cos\theta < 0.0$,

iii) $p_\pi < 300$ MeV/c and $\cos\theta > 0.0$, and

iv) $p_\pi < 300$ MeV/c and $\cos\theta < 0.0$.

Of these four kinematic regions, enhanced rates into region (iv) would provide the strongest evidence for inelastic rescattering, particularly

since pion absorption is expected to deplete the low momentum pion population. Using the neon and deuterium data, we can determine a lower limit for inelastic rescattering based on charged pions within kinematic region (iv). Table 8-1 lists the low momentum fractions, the backscatter fractions, and the population fraction which is both backward and momentum degraded, $f_{p\cap\theta}$, for the muons and pions in the neon and deuterium data sets.

From Table 8-1, the muon distributions for the deuterium and neon interaction sets both show a 0.06 ± 0.01 correlation (e.g., $f_{p\cap\theta}$ value) between low momentum and backward direction. This indicates that, for particles not susceptible to intranuclear rescattering, there is no statistical difference between the two data sets, and we can use thus use $f_{p\cap\theta}$ to measure a component of intranuclear rescattering. As seen in Table 8-1, when we apply this analysis to the inclusive charged pion samples, there is fractionally 0.03 ± 0.04 (0.11 ± 0.10) more slow backward π^+s (π^-s) in the neon data than there are in the deuterium data.

8.3 Exclusive Pion Distributions

Pion rescattering effects can be further explored using exclusive pion reaction channels. Figures 8-3 show the comparative momentum and π^+-production angle cosine distributions for the deuterium and neon single pion reaction channel $\mu^-\pi^+p$. This channel contains 45 percent of all positive pions in the ν_μ-neon data. Slow momentum fractions for the momentum distributions are $f_p^D(\pi^+_{SINGLE}) = 0.55 \pm 0.05$ and $f_p^{Ne}(\pi^+_{SINGLE}) = 0.57 \pm 0.09$ for the deuterium and neon data, respectively. Here, the fraction $f_p(\pi^+_{SINGLE})$

TABLE 8-1

MEASURED FRACTIONS OF PION SAMPLES HAVING PARTICLES WITH KINEMATICS FAVORED BY INELASTIC RESCATTERING

	Deuterium	Neon	Δ(Ne-D)
$f_p(\mu^-_{INC})$	0.43 ± 0.02	0.43 ± 0.02	0.00 ± 0.03
$f_\theta(\mu^-_{INC})$	0.12 ± 0.01	0.06 ± 0.01	-0.06 ± 0.01
$f_{p\cap\theta}(\mu^-_{INC})$	0.06 ± 0.01	0.06 ± 0.01	0.00 ± 0.01
$f_p(\pi^+_{INC})$	0.45 ± 0.03	0.47 ± 0.05	0.02 ± 0.06
$f_\theta(\pi^+_{INC})$	0.17 ± 0.02	0.20 ± 0.03	0.03 ± 0.04
$f_{p\cap\theta}(\pi^+_{INC})$	0.15 ± 0.02	0.18 ± 0.03	0.03 ± 0.04
$f_p(\pi^-_{INC})$	0.32 ± 0.05	0.42 ± 0.12	0.10 ± 0.13
$f_\theta(\pi^-_{INC})$	0.10 ± 0.03	0.22 ± 0.06	0.12 ± 0.07
$f_{p\cap\theta}(\pi^-_{INC})$	0.09 ± 0.04	0.20 ± 0.09	0.11 ± 0.10

FIGURE 8-3a

EXCLUSIVE SINGLE Pi+ MOMENTUM FROM $\mu^-\pi^+p$

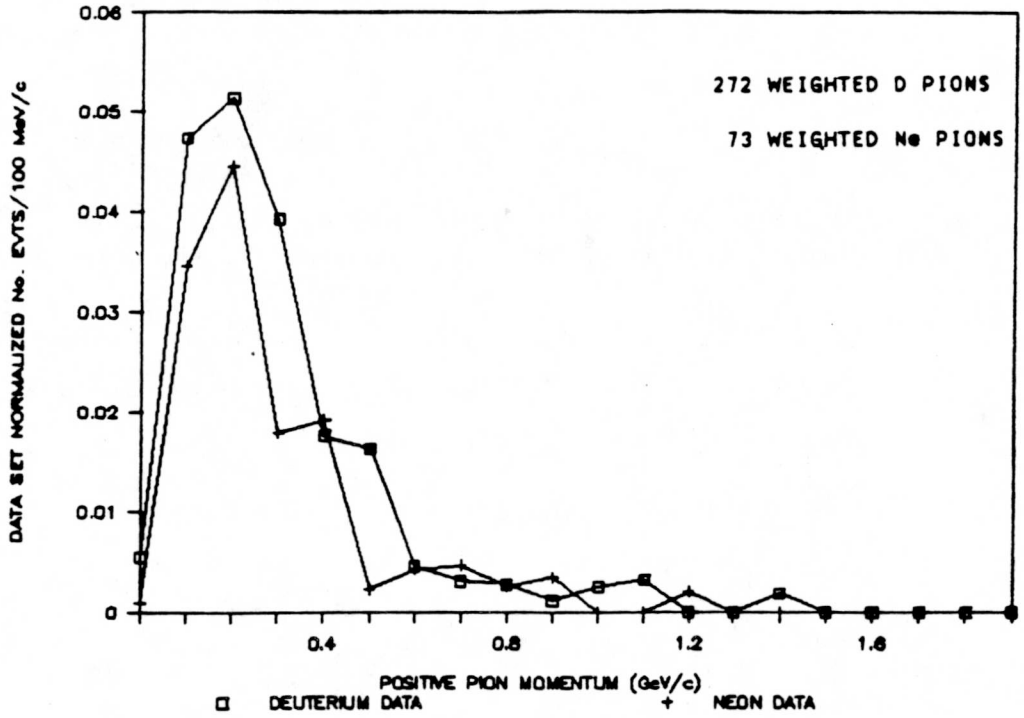

FIGURE 8-3b

EXCLUSIVE SINGLE Pi+ PRODUCTION COSINE FROM $\mu^-\pi^+p$

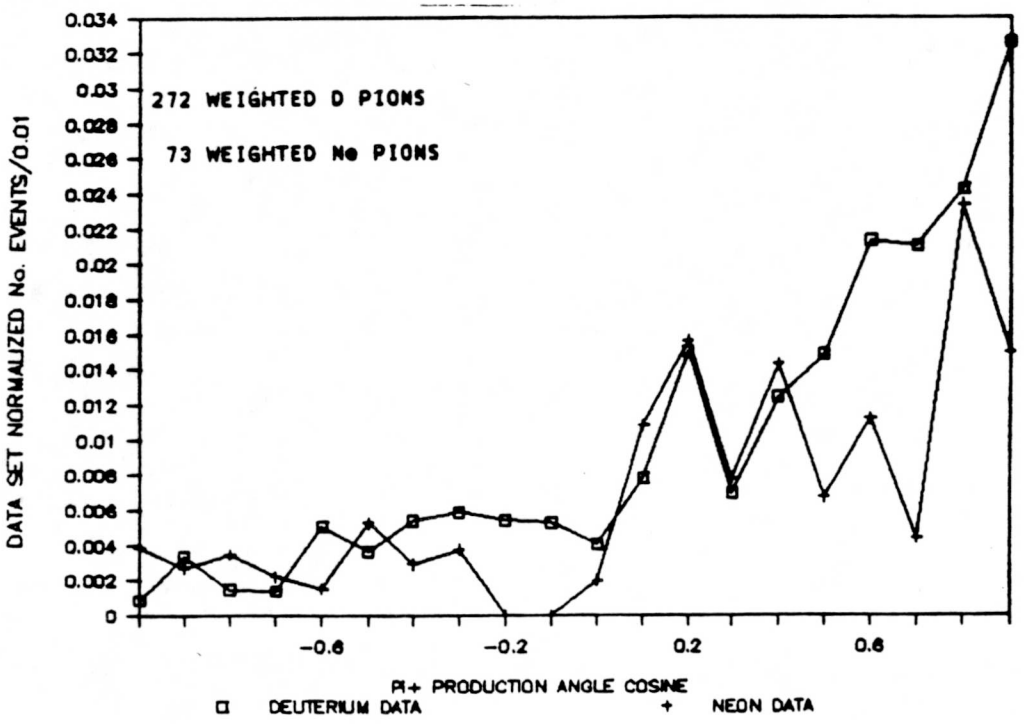

is the weighted number of π^+ from the $\nu_\mu N \rightarrow \mu^- p \pi^+$ reaction channel having momentum below 300 MeV/c divided by the total weighted number of pions in the reaction channel. Similarly, the backscatter fractions corresponding to the cosθ distributions are found to be $f_\theta^D(\pi^+_{SINGLE}) = 0.22 \pm 0.03$ and $f_\theta^{Ne}(\pi^+_{SINGLE}) = 0.20 \pm 0.05$.

The degree of similarity in the exclusive channel $\mu^-\pi^+p$ between the neon and deuterium data is however most striking in the fraction $f_{p\cap\theta}$ of pions both slow and backward. These are $f^D_{p\cap\theta}(\pi^+_{SINGLE}) = 0.17 \pm 0.03$ and $f^{Ne}_{p\cap\theta}(\pi^+_{SINGLE}) = 0.17 \pm 0.05$.

The two-pion exclusive final state $\mu^-\pi^-\pi^+p$ is also examined for effects of intranuclear rescattering; this channel is the major contributor of π^- mesons in both data sets. Figures 8-4 show the comparative momentum and pion production angle distributions for the deuterium and neon positive pions, while Figures 8-5 show the same distributions for negative pions. The positive pions in this exclusive channel represent six percent of the total inclusive π^+ neon data sample. The low momentum pion fractions from the momentum distributions are $f_p^D(\pi^+_{DOUBLE}) = 0.80 \pm 0.16$ and $f_p^{Ne}(\pi^+_{DOUBLE}) = 0.56 \pm 0.17$. Backscatter fractions from the cosθ distributions are $f_\theta^D(\pi^+_{DOUBLE}) = 0.44 \pm 0.12$ and $f_\theta^{Ne}(\pi^+_{DOUBLE}) = 0.31 \pm 0.14$.

Low momentum fractions from the π^- momentum distributions are $f_p^D(\pi^-_{DOUBLE}) = 0.36 \pm 0.12$ and $f_p^{Ne}(\pi^-_{DOUBLE}) = 0.17 \pm 0.10$. In Figure 8-5b), neon exclusive π^- population is depleted in the forward direction (cos$\theta > 0.7$) relative to deuterium (0.56 ± 0.19 exclusive D events as compared with 0.07 ± 0.03 exclusive Ne events) even though backscatter fractions for the two distributions are within errors: $f_\theta^D(\pi^-_{DOUBLE}) =$

FIGURE 8-4a

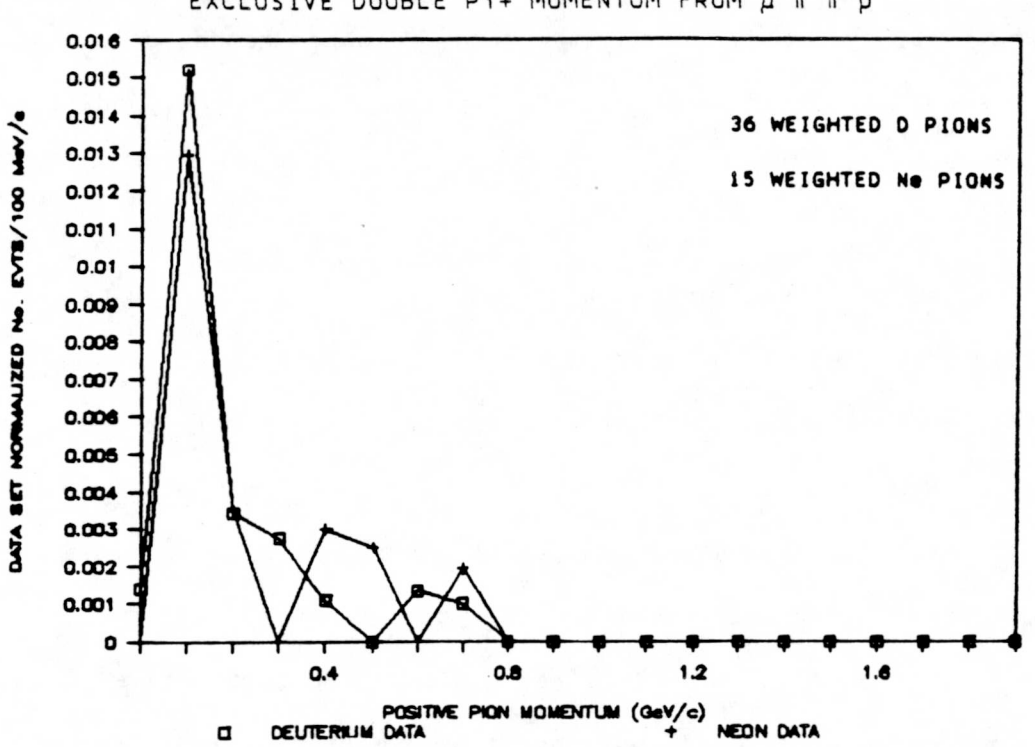

FIGURE 8-4b

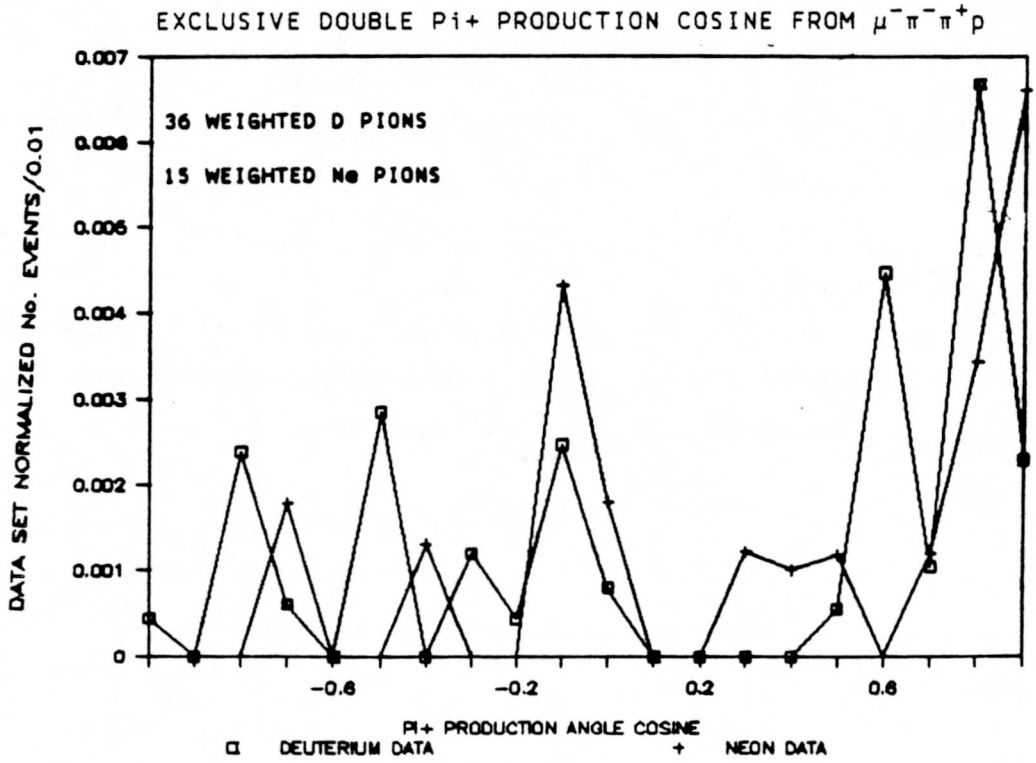

FIGURE 8-5a

EXCLUSIVE DOUBLE Pi- MOMENTUM FROM $\mu^-\pi^-\pi^+p$

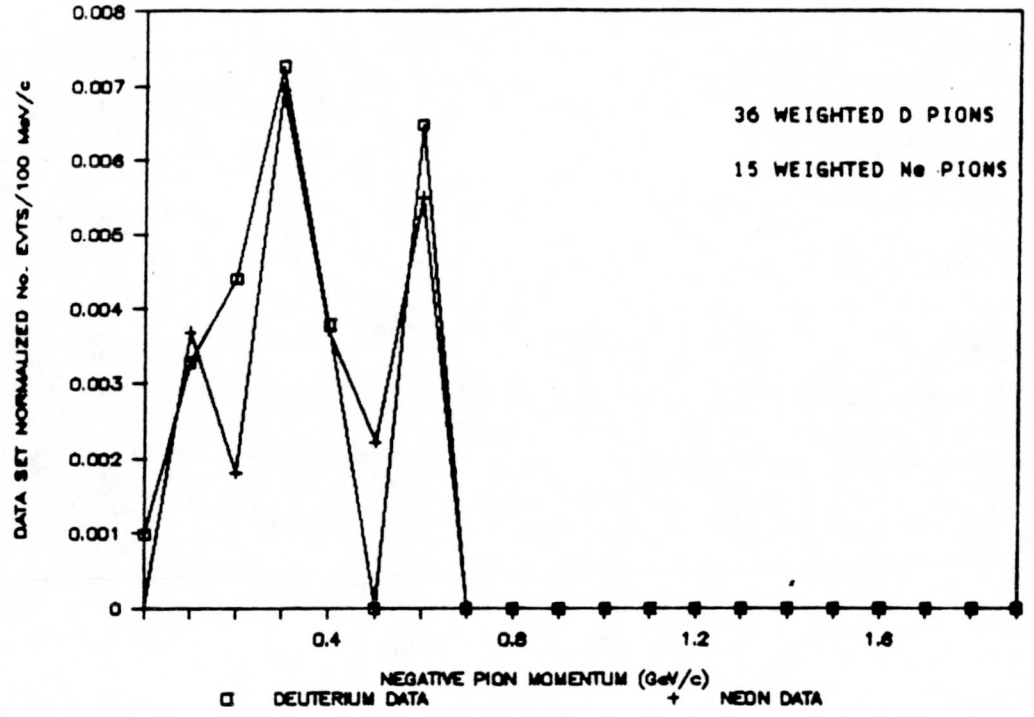

FIGURE 8-5b

EXCLUSIVE DOUBLE Pi- PRODUCTION COSINE FROM $\mu^-\pi^-\pi^+p$

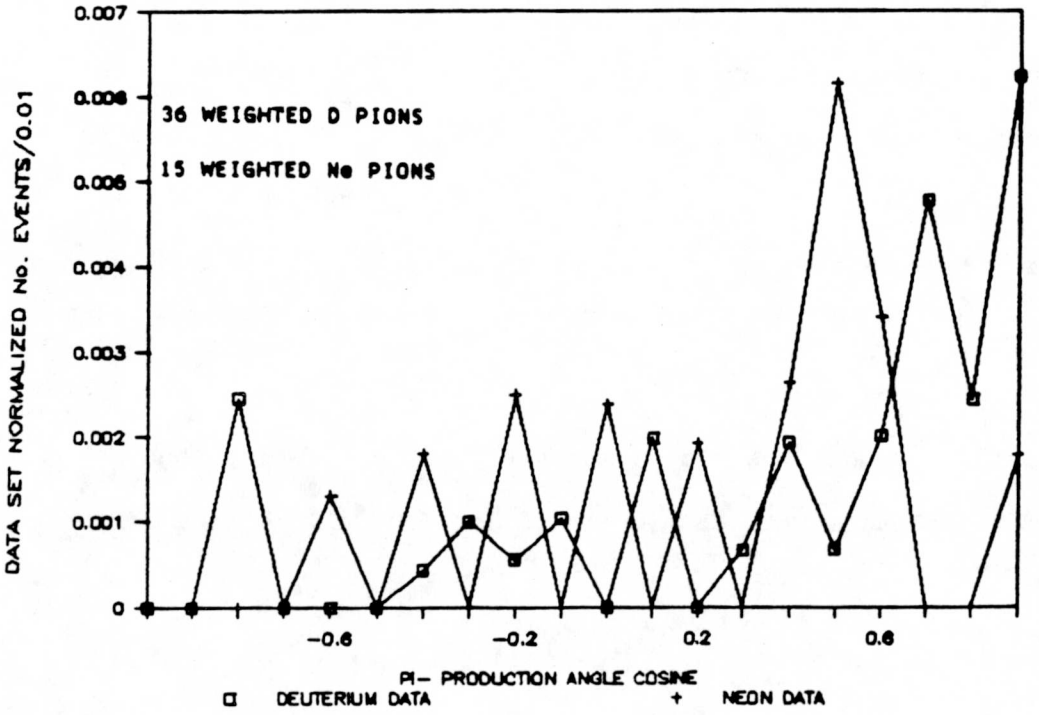

0.24 ± 0.08 and $f_{\theta}^{Ne}(\pi^{-}_{DOUBLE}) = 0.28 \pm 0.14$ for the deuterium and neon data respectively. Given the limited statistics and the fact that the nuclear Fermi motion is not identical in the two nuclei, we are reluctant to draw conclusions from this two-pion exclusive channel comparison.

8.4 Summary

The four intranuclear rescattering processes affect pion kinematic distributions differently. Pion absorption depletes the low momentum population without regard to angular distribution, inelastic rescattering and charge exchange affects only both particle momentum and direction, while elastic scattering affects pion direction, primarily as small deflections about the original direction of travel. By simultaneously comparing the neon and deuterium pion momentum and angular distributions, evidence for inelastic rescattering can be obtained. This comparison is complicated by the presence of the other three processes; by constraining our analysis to low momentum pions (in the absorption depleted region) produced in the backward hemisphere (to reduce elastic scattering contamination), only charge exchange remains as a significant contaminant of our population sample. However, as noted in Chapter 7, the charge exchange rate is approximately five percent and therefore affects the delineated region at a known rate.

The momentum degradation present in inelastic rescattering can yield changes throughout the entire momentum spectrum, while angular deflections can cause events to migrate to and from all regions of the $\cos\theta_{\pi}$

distribution. Thus the delineated low momentum, backward kinematic region captures only a fraction of the true inelastically rescattered pions. Hence, any measurements of inelastic rescattering based on this reduced population is a lower limit of the true measure, due both to kinematic constraints and contamination from other processes.

The validity of using the low momentum, backward kinematic region was tested by comparing the deuterium and neon muon populations, particles which are not subject to intranuclear rescattering. We computed the fraction, $f_{p\cap\theta}$, by determining the number of weighted muons in each data set with momentum below 300 MeV/c and $\cos\theta_\mu < 0.0$ and divided this number by the total weighted number of muons. These results are listed in Table 8-2. The neon fractional population in this kinematic region is equal to the deuterium population fraction, indicating no rescattering effects and validating the use of $f_{p\cap\theta}$ as a discriminator.

Similar analysis in the deuterium and neon inclusive charged pion samples produce a different result. As seen in Table 8-2, the neon fractional populations in the $p < 300$ MeV/c, $\cos\theta_\pi < 0.0$ kinematic region are 0.03 ± 0.04 and 0.11 ± 0.10 greater than the deuterium populations for the π^+ and π^- distributions, respectively. From these results, a lower limit for charged pion inelastic rescattering is determined to be 0.03 ± 0.04 by combining the two charged pion results.

To further explore pion inelastic rescattering, we examined the $\mu^-\pi^+p$ final state reaction. Examining the slow backward produced pions in this final state yields the measurements listed in Table 8-2. The

TABLE 8-2

SUMMARY OF $f_{p \cap \theta}$ MEASUREMENTS FOR PIONS

Data Sample	Deuterium	Neon	Δ(Ne-D)
Inclusive Muons (Non-rescattering calibration)			
$f_{p \cap \theta}(\mu_{INC})$	0.06 ± 0.01	0.06 ± 0.01	0.00 ± 0.01
Inclusive π^+ mesons			
$f_{p \cap \theta}(\pi^+_{INC})$	0.15 ± 0.02	0.18 ± 0.03	+0.03 ± 0.04
Inclusive π^- mesons			
$f_{p \cap \theta}(\pi^-_{INC})$	0.09 ± 0.04	0.20 ± 0.09	+0.11 ± 0.10
Inclusive $\pi^\pm$ mesons			
$f_{p \cap \theta}(\pi^\pm_{INC})$	0.15 ± 0.02	0.18 ± 0.03	+0.03 ± 0.04
Exclusive $\mu^-\pi^+p$ mesons			
$f_{p \cap \theta}(\pi^+_{SINGLE})$	0.17 ± 0.03	0.17 ± 0.05	0.00 ± 0.06
Inclusive π^+ without $\mu^-\pi^+p$ mesons			
$f_{p \cap \theta}(\pi^+_{INC-SINGLE})$	0.14 ± 0.02	0.19 ± 0.04	+0.05 ± 0.04

values for $f_{p\cap\theta}(\pi^+_{SINGLE})$ for the deuterium and neon data sets are equal, indicating that in this reaction channel, inelastic rescattering is absent. As we will discuss in Chapter 9, pions generated in this final state are primarily the result of Δ^{++} disassociation. This delta production may serve to suppress the rescattering of final state pions.

To check this hypothesis, we compute $f_{p\cap\theta}(\pi^+)$ for all positive pions except those contained in the final state $\mu^-\pi^+p$. If delta production is suppressing π^+ inelastic rescattering, then Δ(Ne-D), the difference $f^{Ne}_{p\cap\theta}(\pi^+_{INC-SINGLE})-f^{D}_{p\cap\theta}(\pi^+_{INC-SINGLE})$, will be larger than the difference for inclusive charged pion measures of $f_{p\cap\theta}$. From Table 8-2, we see that this is the case: by examining all π^+ events except those contained in the reaction $\mu^-\pi^+p$, the difference in the fractional population both slow and backward is two percent greater than the inclusive π^+ distribution. Our hypothesis, that delta production is suppressing inelastic rescattering, is thus plausible. In the next chapter, we directly examine delta kinematics for evidence of inelastic rescattering.

CHAPTER 9

SEARCH FOR INELASTIC RESCATTERING IN FINAL STATE PROTON AND DELTA DISTRIBUTIONS

9.1 Introduction

It is possible that intranuclear rescattering may be observable in final state proton kinematic distributions. For interaction protons, the effects of inelastic and elastic scattering may be searched for in the same manner as with pions; that is, inelastic scattering alters the momentum distribution, while both processes affect the cosθ distribution. The spectator proton distributions, however, may show distortions in both kinematic quantities as a result of recoils from intranuclear collisions. Unlike the pion distributions, however, the proton distributions from neon are not depleted by absorption. These distributions are examined in Section 9.2.

Analysis of low energy pion and proton interactions within the nucleus is complicated by the presence of Nπ resonances, particularly the Δ (1232 MeV/c^2) system. If a sizable fraction of the events at these neutrino energies contains delta production, then evidence for intranuclear rescattering may be primarily in delta kinematic distributions, and only secondarily in the pion and proton distributions. Section 9.3 presents

determinations of the rates of delta production in the two data sets, and examines the delta kinematic distributions for evidence of intranuclear rescattering. Section 9.4 summarizes the chapter.

9.2 Proton Distributions

In processing of the deuterium and neon data sets, the methods used to identify final state protons were somewhat different. In deuterium, protons represent the best fit to positive charged tracks, compatible with ionization, while protons in the neon sample are identified entirely using ionization. For both data, kinematic selections differentiate spectator and interaction protons. To avoid biasing comparative spectator distributions in favor of low energy deuterium protons (those which were fitted to the event but not observed), only protons which have been measured are used in this analysis.

Momentum comparisons between the deuterium and neon spectator protons are further complicated by the difference in the Fermi momentum between the two nuclei. The Fermi momentum distribution for oxygen (which presumably approximates the neon distribution) and the Hulthen distribution for deuterium are shown in Figure 9-1.

Figures 9-2 show the weighted momentum distributions for the deuterium and neon interaction and spectator protons. A close match in momentum distribution shapes is observed for the interaction protons.

FIGURE 9-1

FERMI MOMENTUM DISTRIBUTIONS

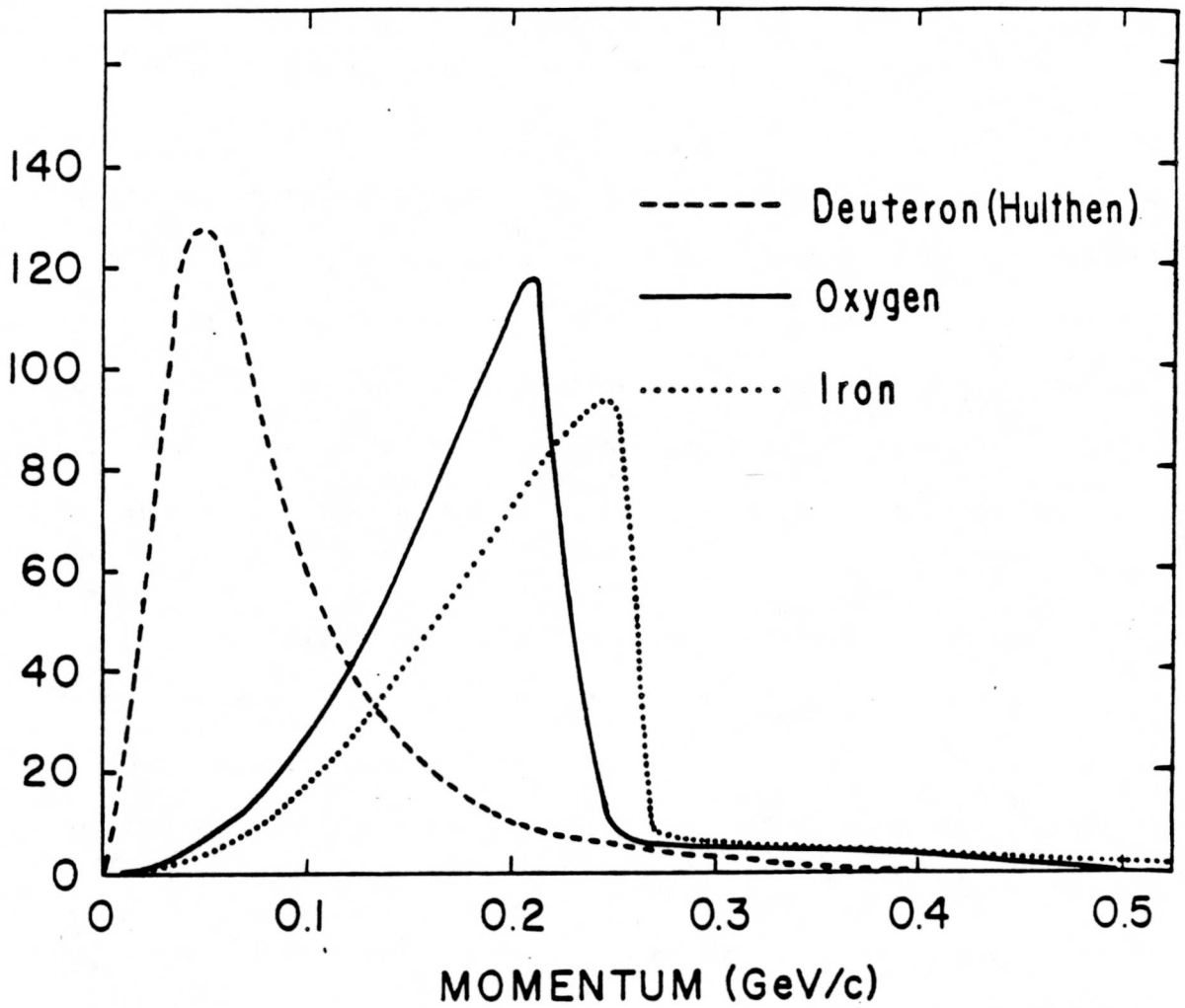

FIGURE 9-2a

INCLUSIVE INTERACTION PROTON MOMENTUM

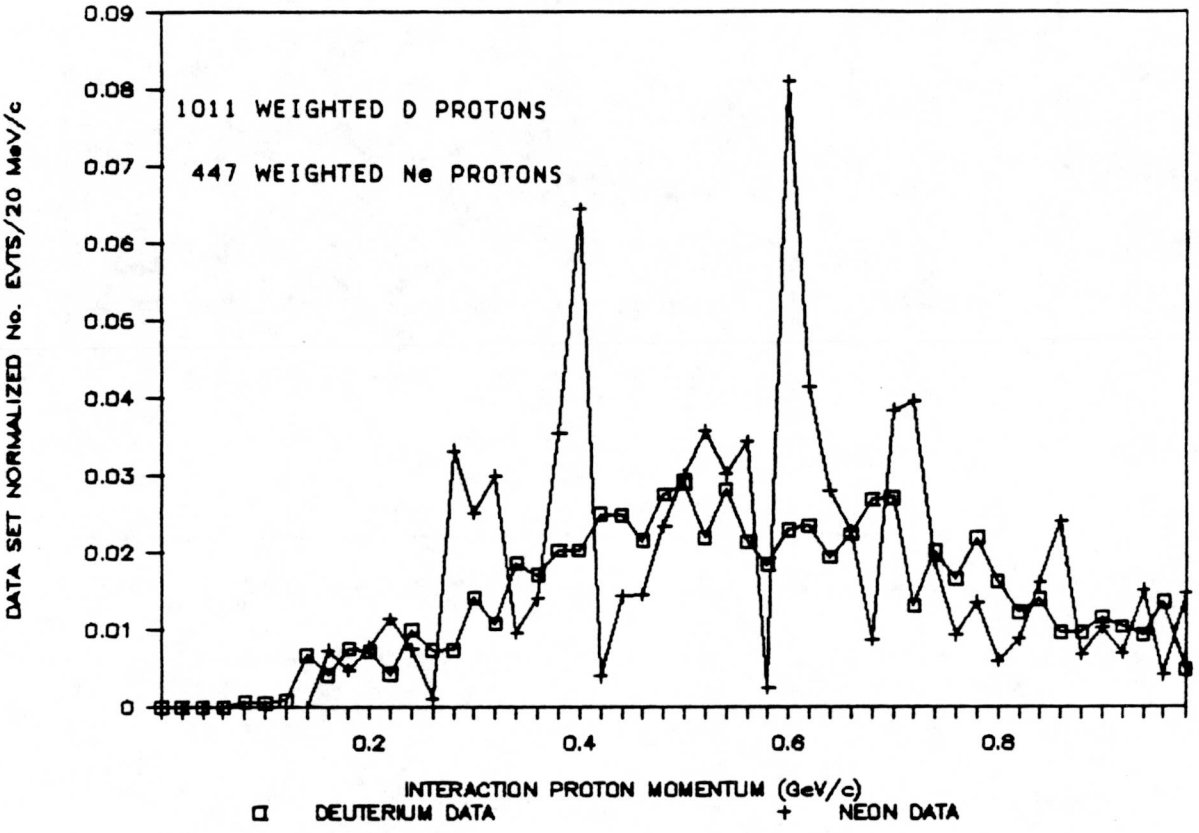

FIGURE 9-2b

INCLUSIVE D SPECTATOR PROTON MOMENTUM

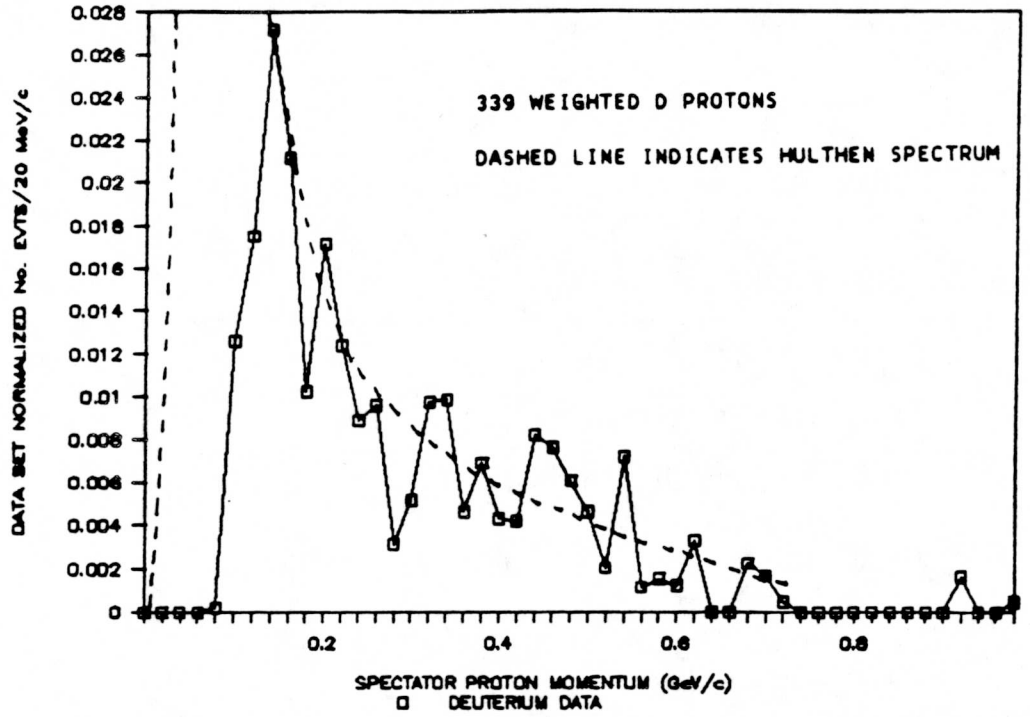

FIGURE 9-2c

INCLUSIVE Ne SPECTATOR PROTON MOMENTUM

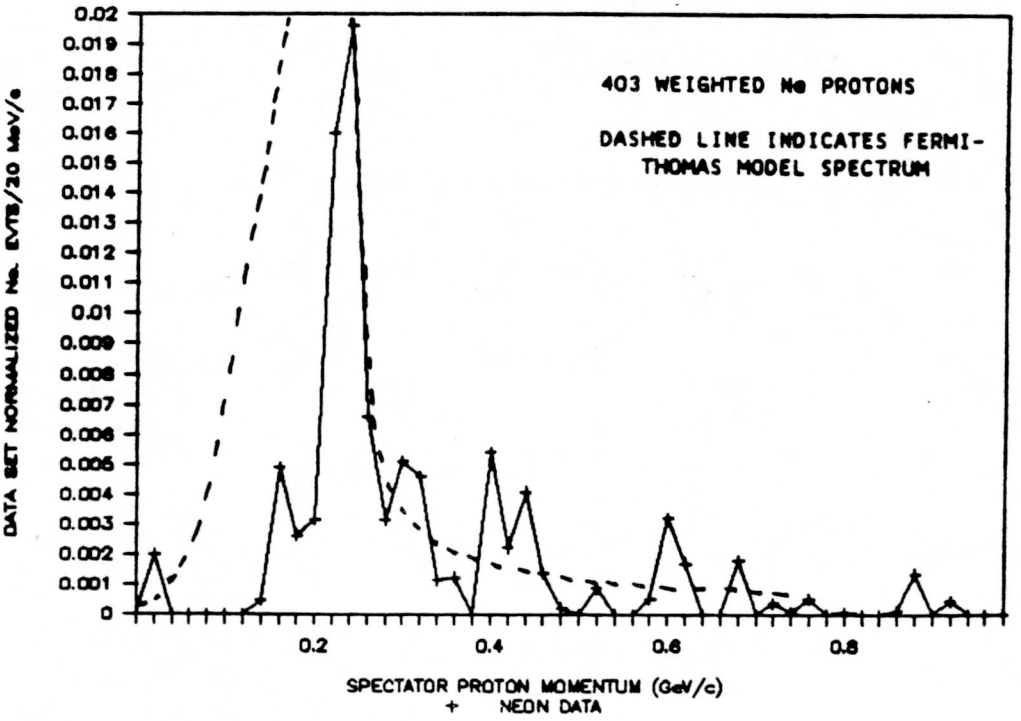

Figure 9-3a) shows the interaction proton production angle distributions for both the deuterium and neon events. These distributions are also closely matched in shape.

Figure 9-2b) and c) show the spectator momentum distributions for the deuterium and neon data fitted to the Hulthen and Fermi momentum spectra. The deuterium distribution closely matches the Hulthen spectrum above 140 MeV/c. Below this momentum, protons were not consistently identified and measured. The neon spectator momentum distribution has similar difficulties with a momentum threshold of 240 MeV/c. Above this momentum, the Fermi-Thomas momentum model of Bodek and Ritchie[1] reproduces the observed neon distribution. No gross evidence of elastic or inelastic scattering in the neon nucleus is apparent in these spectator momentum distributions.

Figure 9-3b) shows the proton production angle cosine distribution for the D- and Ne-data spectator protons. The distribution profiles for the data sets match, indicating the absence of abundant scattering by these particles within the neon nucleus.

The lack of clear signatures for inelastic rescattering in the proton samples is also apparent from an examination of the differences in population fractions of backward, slow protons in the deuterium and neon data. Table 9-1 presents the proton sample fractions f_p, f_θ, and $f_{p\cap\theta}$ from the deuterium and neon interaction and spectator protons. (Momentum thresholds for computing $f_p(p_{INTER})$ and $f_p(p_{SPECT})$ are 400 MeV/c and 300 MeV/c, respectively.) These fractions, in particular the $f_{p\cap\theta}$ fractions, do not indicate the presence of substantial inelastic rescattering; the small

FIGURE 9-3a

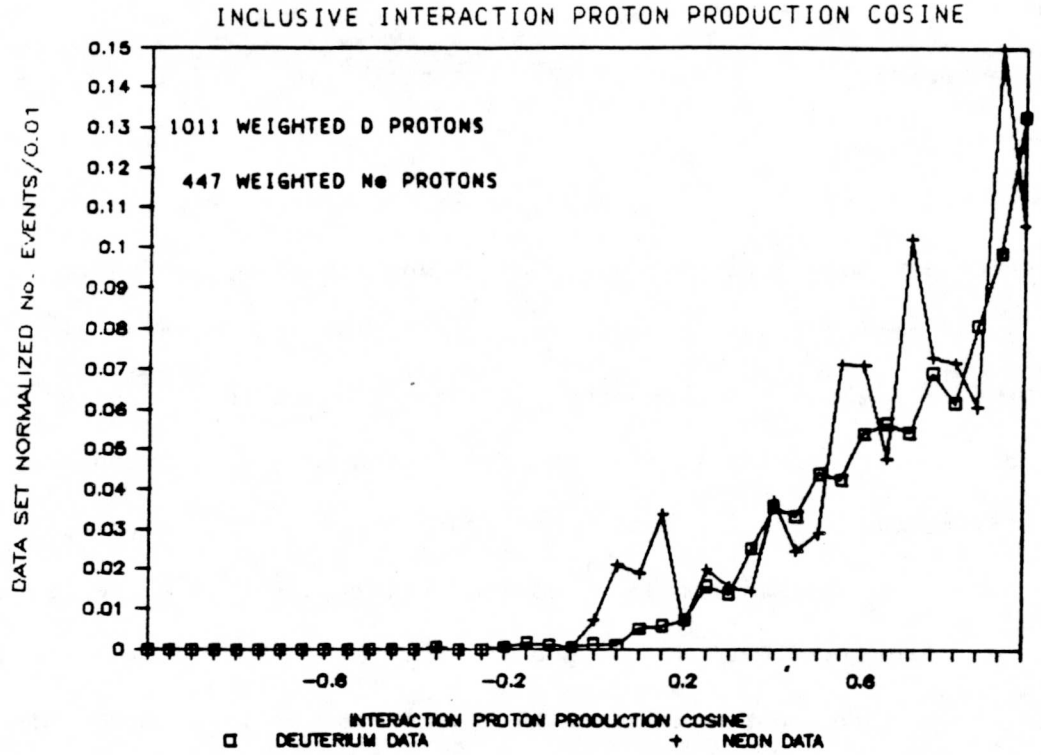

FIGURE 9-3b

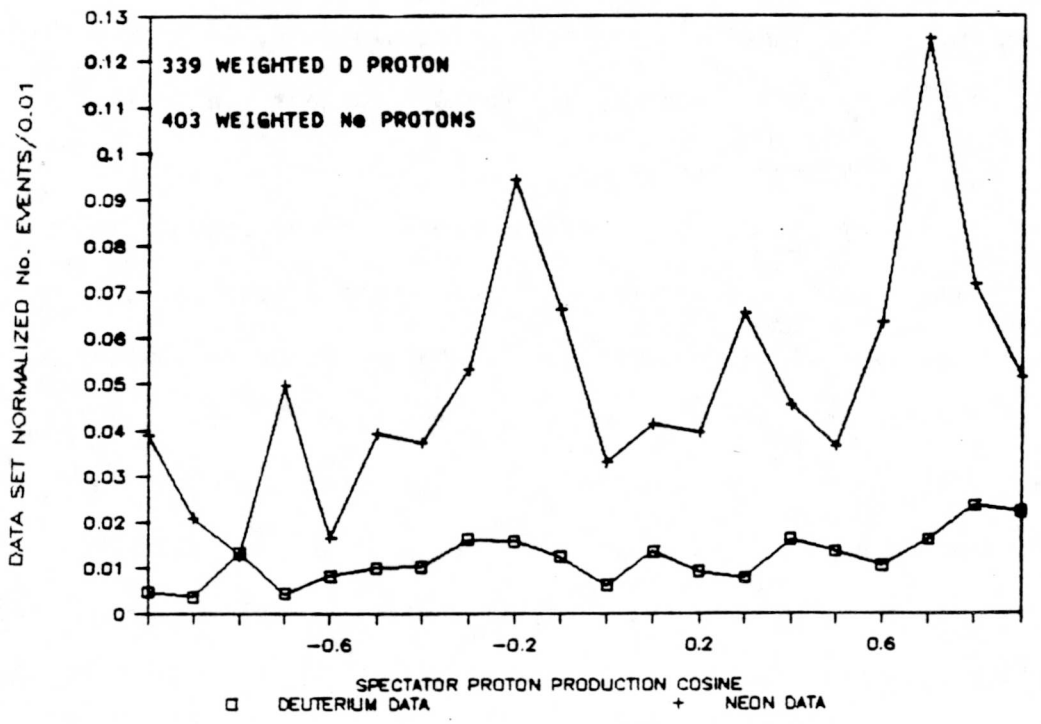

TABLE 9-1

MEASURED FRACTIONS OF PROTON SAMPLES HAVING KINEMATICS FAVORED BY INELASTIC RESCATTERING

	Deuterium	Neon	Δ(Ne-D)
$f_p(P_{INTER})$	0.20 ± 0.03	0.36 ± 0.07	0.16 ± 0.08
$f_\theta(P_{INTER})$	0.00 ± 0.01	0.00 ± 0.01	0.00 ± 0.01
$f_{p\cap\theta}(P_{INTER})$	0.01 ± 0.01	0.00 ± 0.01	-0.01 ± 0.01
$f_p(P_{SPECT})$	0.60 ± 0.05	0.47 ± 0.07	-0.13 ± 0.09
$f_\theta(P_{SPECT})$	0.42 ± 0.07	0.43 ± 0.12	0.01 ± 0.14
$f_{p\cap\theta}(P_{SPECT})$	0.27 ± 0.04	0.22 ± 0.05	-0.05 ± 0.06

difference (-0.05 ± 0.06) in the slow, backward spectator distributions may reflect the greater Fermi motion present in the neon proton sample.

9.3 Delta Distributions

In studying intranuclear rescattering using low-energy neutrino reactions, we have commented on the possibility that pπ resonant systems may influence rescattering results. To examine this hypothesis, the exclusive three-constraint reaction channels $\mu^-\pi^+p$ and $\mu^-\pi^-\pi^+p$ are used to analyze the delta (1232 MeV/c^2) resonance.

9.3.1 Δ^{++} Production

The exclusive $\mu^-\pi^+p$ reaction channel is used to examine the kinematics of the Δ^{++} produced in single pion events for evidence of intranuclear rescattering. The unweighted and weighted invariant mass distributions for the deuterium data is shown in Figures 9-4, and in Figures 9-5 for the neon data. A clear Δ^{++} signal at 1.2 GeV/c^2 is observed in both data sets. To estimate the number of weighted deltas present, the unweighted $p\pi^+$ combinatorial background is approximated using a hand-drawn curve. The number of $p\pi^+$ events over this background is then computed and compared on a bin-by-bin basis to determine the average bin weight. Using this technique, 138 ± 14 weighted deltas (0.10 ± 0.01 of the total weighted event sample) are observed in the deuterium data and 37 ± 4 weighted deltas

FIGURE 9-4a

UNWEIGHTED D SINGLE PION (P Pi+) MASS

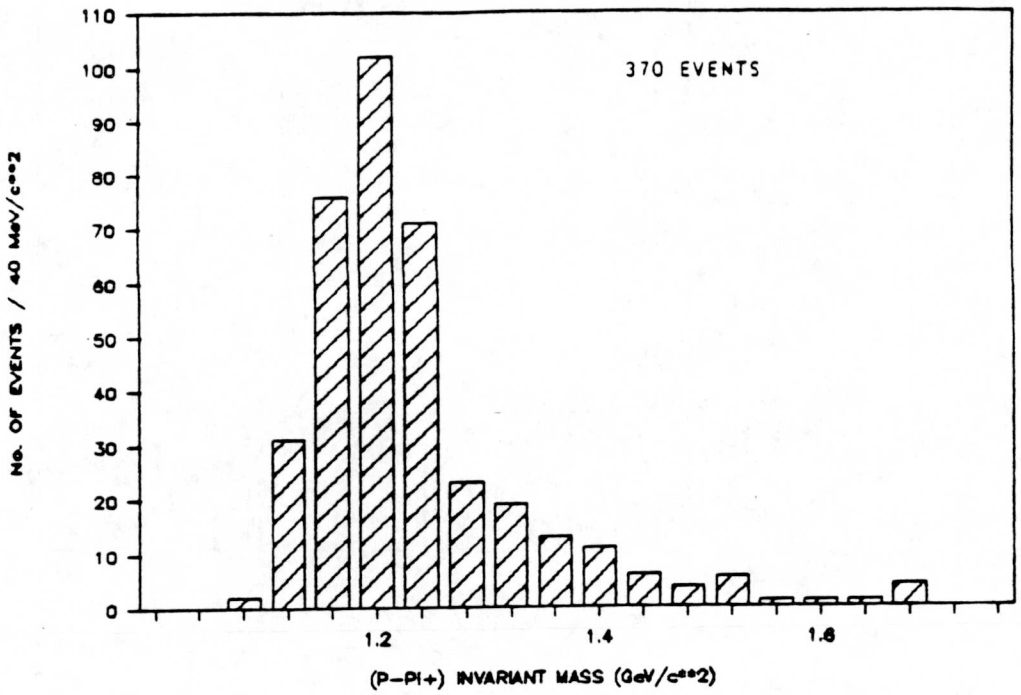

FIGURE 9-4b

WEIGHTED D SINGLE PION (P Pi+) MASS

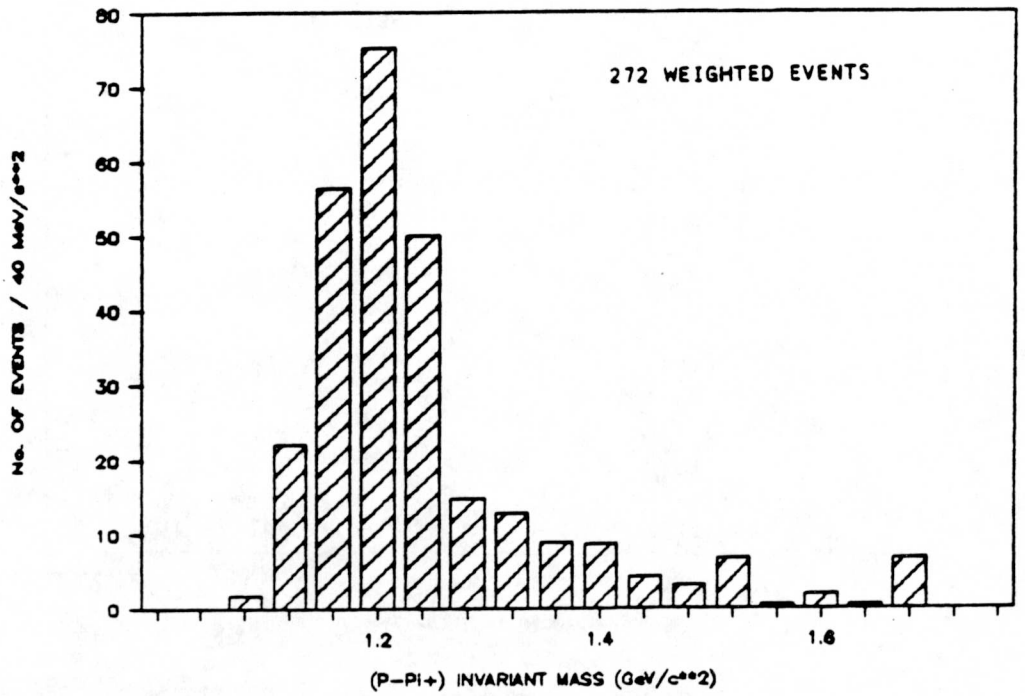

FIGURE 9-5a

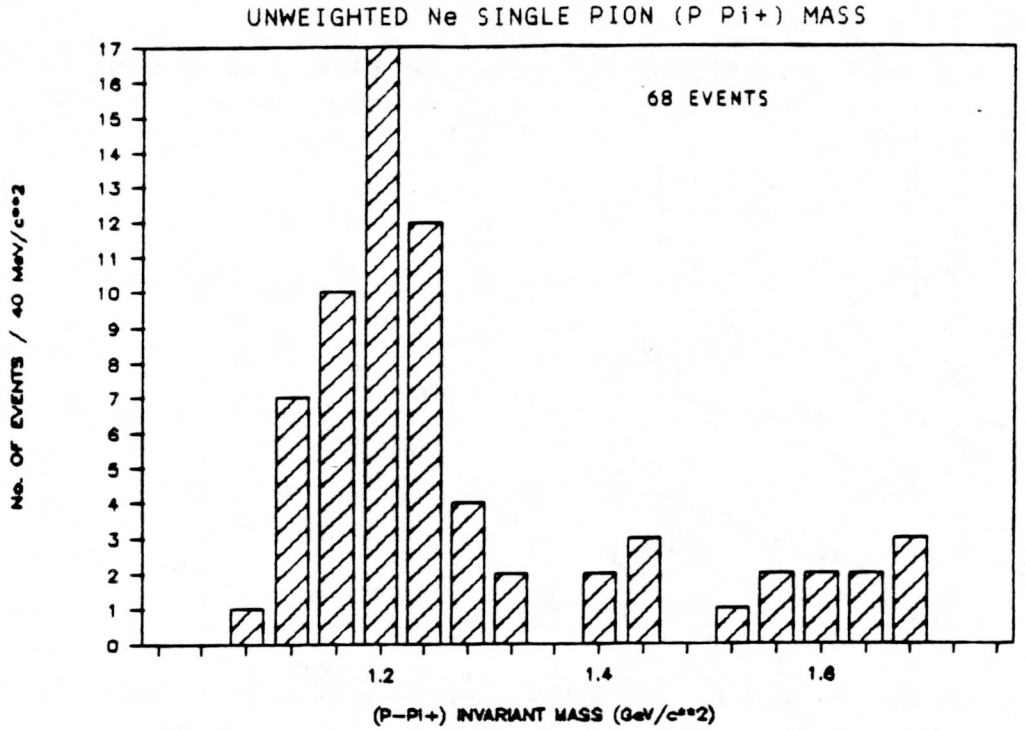

FIGURE 9-5b

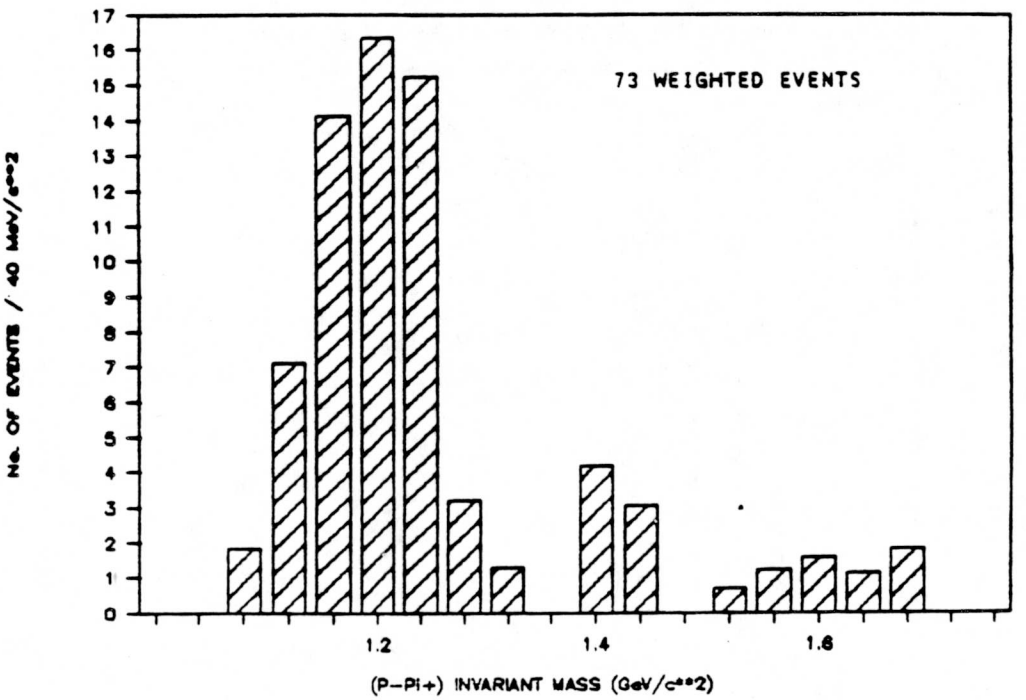

(0.07 ± 0.01 of the total weighted event sample) are observed in the neon data for this exclusive channel. Thus, 0.51 ± 0.05 of the single charged pion events in both the deuterium and neon events result from Δ^{++} disassociation. Hence, the single pion channel is dominated by delta production.

The weighted $p\pi^+$ invariant mass distributions from the two event samples are shown superimposed in Figure 9-6. A broadening of the neon Δ^{++} signal relative to the deuterium peak is discernable. The deuterium Δ^{++} peak has a FWHM of 117 MeV/c^2, while the neon Δ^{++} peak has a FWHM of 137 MeV/c^2. Since the invariant mass resolution in the neon-filled BEBC bubble chamber is likely comparable to the resolution of the D-filled 12-foot diameter bubble chamber at these energies, the broadening may reflect pion and proton rescattering in neon. Unfortunately, we are unable to quantify this observation. We note here the apparent decrease in the neon Δ^{++} population (seven percent of weighted neon events) relative to deuterium Δ^{++} (ten percent of events). The depletion suggests that Δ-resonances as well as pions participate in the absorption and charge exchange processes measured in Chapter 7.

Little information can be gained from the Δ^{++} momentum distributions (Figure 9-7a), owing to the limited statistics of the neon data. The fraction of Δ^{++}s (relative to the total weighted event sample) with momentum below 1 GeV/c is $f_p^D(\Delta^{++}_{SINGLE}) = 0.21 \pm 0.03$ and $f_p^{Ne}(\Delta^{++}_{SINGLE}) = 0.25 \pm 0.06$ for the deuterium and neon data. The cosine distributions in Figure 9-7b) suggest a depletion of forward neon Δ^{++} events in the neon data; for events with $\cos\theta > 0.7$, the neon population is reduced by

FIGURE 9-6

SINGLE PION P Pi+ INVARIANT MASS

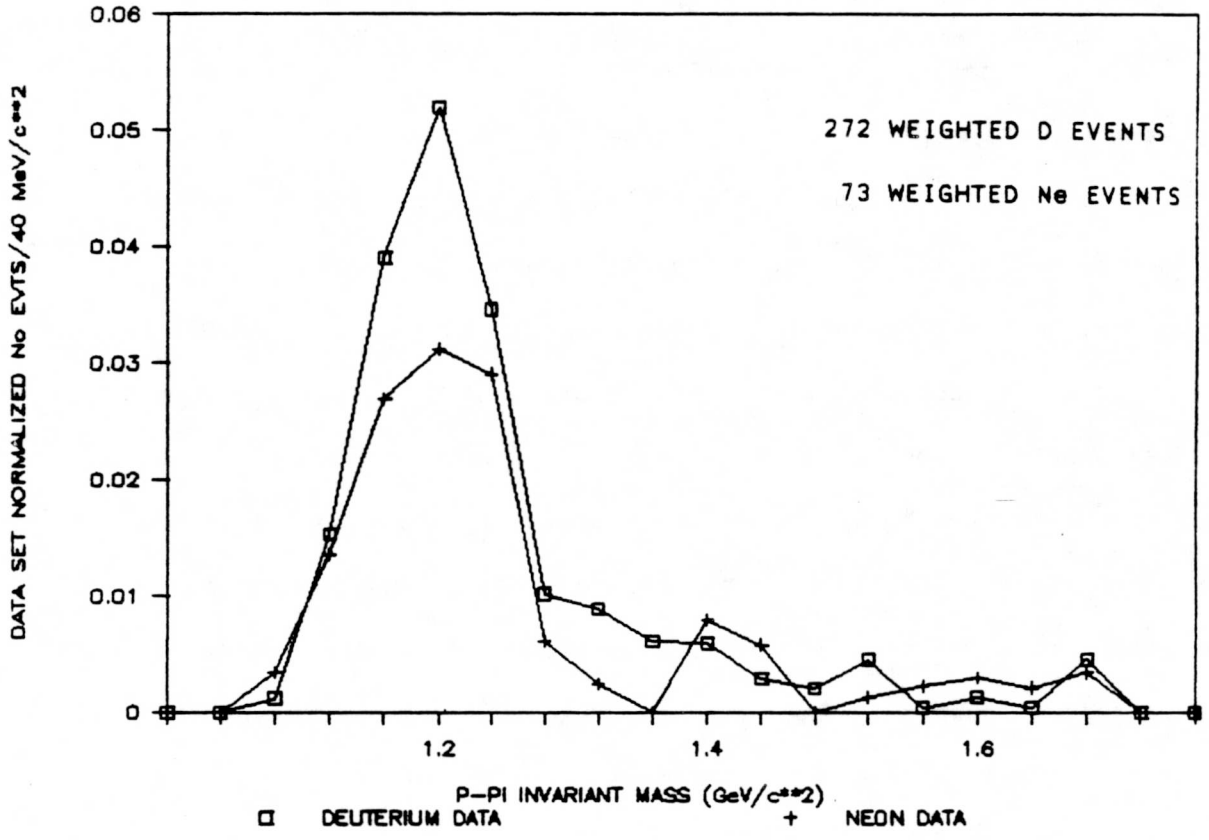

FIGURE 9-7a

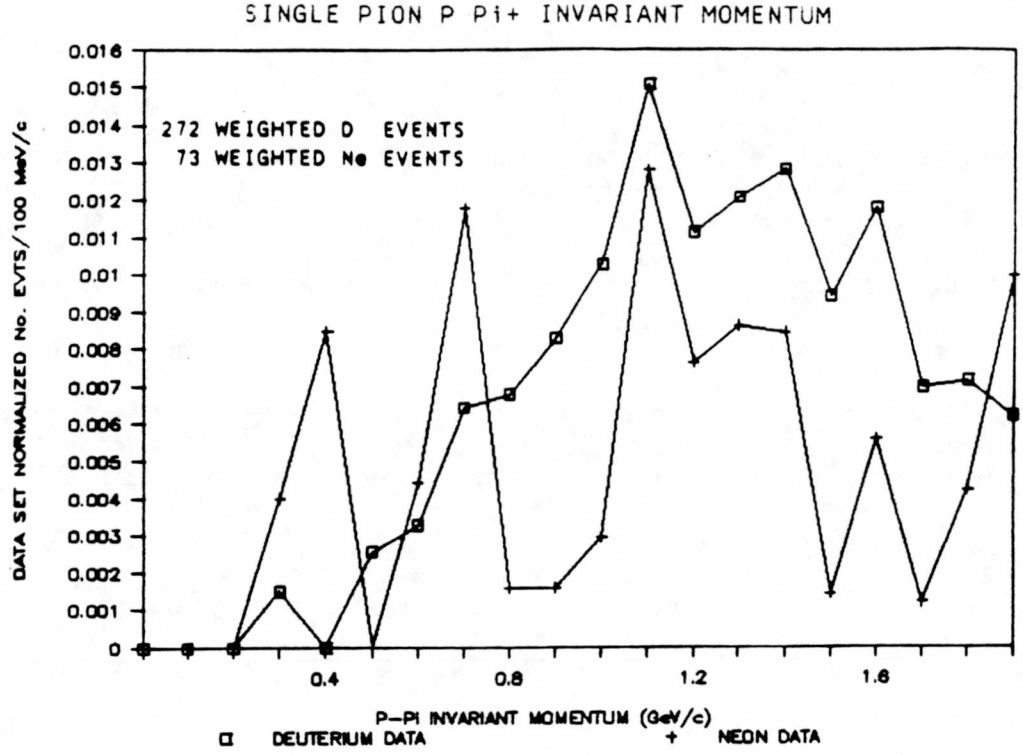

FIGURE 9-7b

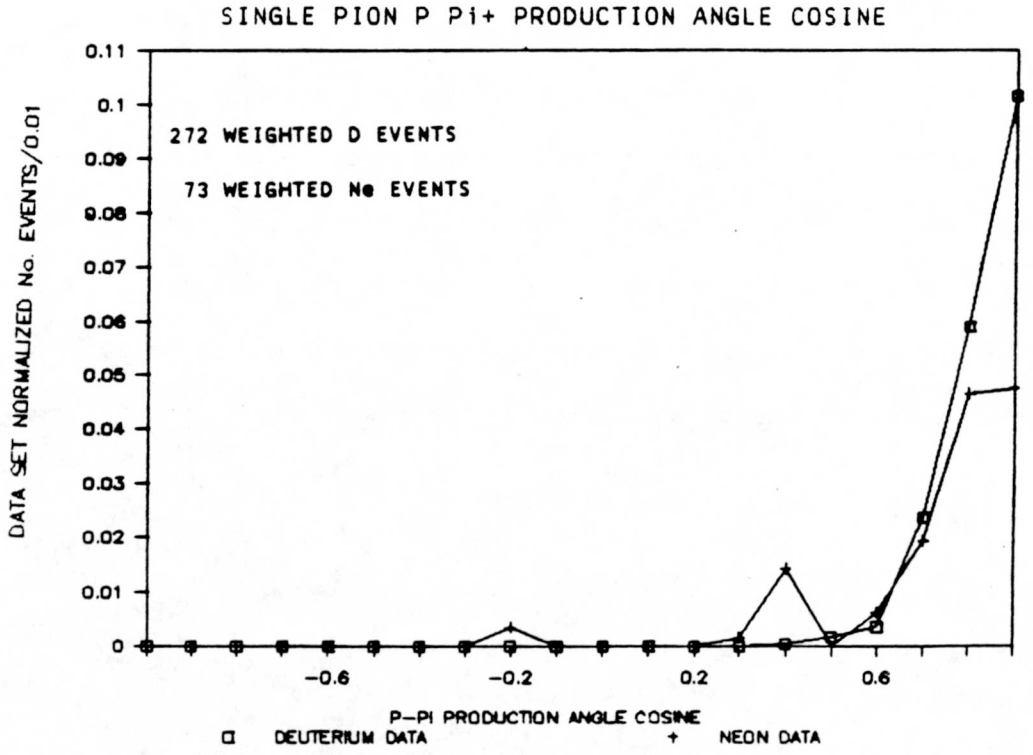

0.16 ± 0.16 relative to the deuterium data. This difference, however, may merely reflect the more violent Fermi motion within neon nuclei.

9.3.2 Delta Production in Two-Pion Events

Evidence for delta production in the two pion exclusive reaction channel $\mu^-\pi^-\pi^+p$ is complicated by Λ (1115 MeV/c^2) production. Although obvious displaced vertices were fit to a lambda hypothesis in the deuterium data, the lack of kinematic fitting of the neon data and the possible occurence of undetected secondary vertices necessitates treatment of all pions from both data sets uniformly, hence lambda removal needs to be based solely on kinematic criteria.

This exclusive channel is further complicated by the presence of rival delta production. Clearly, a single event cannot produce both a Δ^{++} and a Δ°. Thus, determination of the number of deltas produced requires examination of both the $p\pi^+$ and $p\pi^-$ invariant masses as well as assessing the resolving capability of each experiment.

In order to remove the lambda contamination in the data, the invariant $p\pi^-$ mass is required to be within 15 MeV/c^2 of the lambda mass, and the transverse momentum of the π^- relative to the lambda direction is required to be less than 104 MeV/c. This latter requirement can be deduced by considering two body decay kinematics in the lambda rest frame. From both conservation of energy and momentum, we write

$$P_p = P_\Lambda - P_\pi \qquad (9\text{-}1)$$

where P_i is the total four momentum of the i^{th} particle. We form the scalar product:

$$P_p \bullet P_p = P_\Lambda \bullet P_\Lambda - 2P_\Lambda \bullet P_\pi + P_\pi \bullet P_\pi . \qquad (9\text{-}2)$$

In the lambda rest frame, the lambda momentum is zero and its energy equals the lambda mass, while the proton and pion have equal but opposite vector momenta. Thus, Equation (9-2) can be written

$$\begin{aligned} m_p^2 &= m_\Lambda^2 - 2P_\Lambda \bullet P_\pi + m_\pi^2 \\ &= m_\Lambda^2 - 2E_\pi m_\Lambda + m_\pi^2 \end{aligned} \qquad (9\text{-}3)$$

so that

$$E_\pi = m_\Lambda^2 + m_\pi^2 - m_p \; / \; 2m_\Lambda^2 . \qquad (9\text{-}4)$$

Substituting $p_\pi = (E_\pi^2 - m_\pi^2)^{1/2}$, we obtain

$$p_\pi = \{[m_\Lambda^2-(m_\pi+m_p)^2][m_\Lambda^2-(m_\pi-m_p)^2]/4m_\Lambda^2\}^{1/2} . \qquad (9\text{-}5)$$

The equation implies that the maximum momentum for the pion is 104 MeV/c. Although this calculation is performed in the lambda rest frame, momentum transverse to the lambda direction of travel does not receive a Lorentz boost. Hence, the maximum pion transverse momentum in the laboratory frame is 104 MeV/c.

The invariant mass combinations in the data, consisting of 29 unweighted deuterium and 17 unweighted neon events, were examined by hand to identify unambiguous Λ events. A lambda hypothesis is accepted if the reconstructed mass is in the range

$$1.10 < m(p\pi^-) < 1.13 \text{ GeV/c}^2$$

and if

$$|\vec{p}_\pi| \times |\vec{p}_\Lambda| / |\vec{p}_\pi| \; |\vec{p}_\Lambda| < 0.1 \text{ GeV/c}.$$

Five deuterium and two neon events were found which satisfied these criteria and were removed from further analysis. The resulting weighted $p\pi^+$

invariant mass distributions are shown in Figures 9-8 for deuterium and neon, and the $p\pi^-$ invariant mass distributions for deuterium and neon are shown in Figures 9-9.

As with the single pion channel, the number of deltas produced in this two-pion channel is estimated by hand fitting a combinatorial background to the unweighted invariant mass distributions. The excess signal over background is then compared to the weighted distributions on a bin-by-bin basis to determine the number of weighted deltas. Using this technique, the $\mu^-\pi^-\pi^+p$ deuterium contains 20 ± 4 weighted Δ^{++} and 17 ± 5 Δ° events. These values for Δ^{++} and Δ° represent 0.63 ± 0.17 and 0.53 ± 0.18, respectively, of the total weighted events in this exclusive channel. In the neon data, 9 ± 2 weighted Δ^{++} and 2 ± 1 Δ° events are computed over background, representing 0.69 ± 0.25 and 0.15 ± 0.09 of the total weighted neon population in this channel.

The weighted invariant mass distributions, data set normalized, are shown in Figures 9-10 for the $p\pi^+$ and $p\pi^-$ combinations. The "shadowing" trends noted in D. Day, et al.[2] can be seen in these figures: the Δ^{++} signal is seen as a high mass buildup in the $p\pi^-$ distribution, while the Δ° signal is reflected as a low mass buildup in the $p\pi^+$ distribution.

The deuterium Δ^{++} has a FWHM of 80 MeV/c^2 and the neon distribution has a FWHM of 211 MeV/c^2; the Δ° distributions have a FWHM of 154 MeV/c^2 and and 91 MeV/c^2 for the D- and Ne-data, respectively. The broadening of the neon Δ^{++} signal relative to deuterium may indicate the presence of intranuclear scattering, while the broad Δ° signal reflects the Δ^{++} shadow. Owing to limited statistics, the momentum distributions, shown in Figures

FIGURE 9-8a

WEIGHTED D P Pi+ INVARIANT MASS

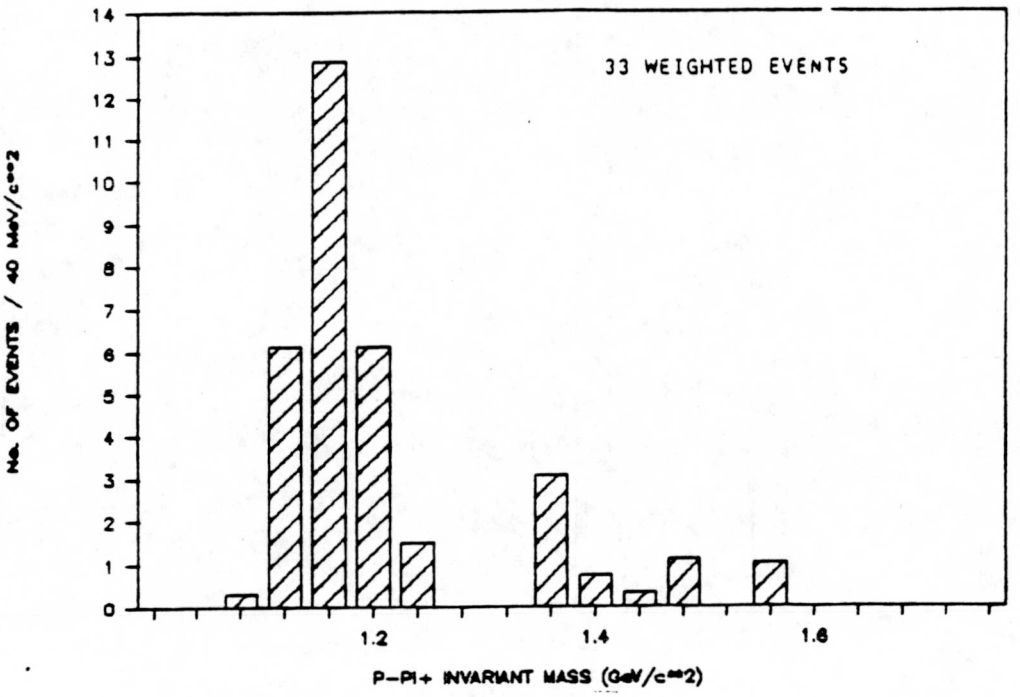

FIGURE 9-8b

WEIGHTED Ne P Pi+ INVARIANT MASS

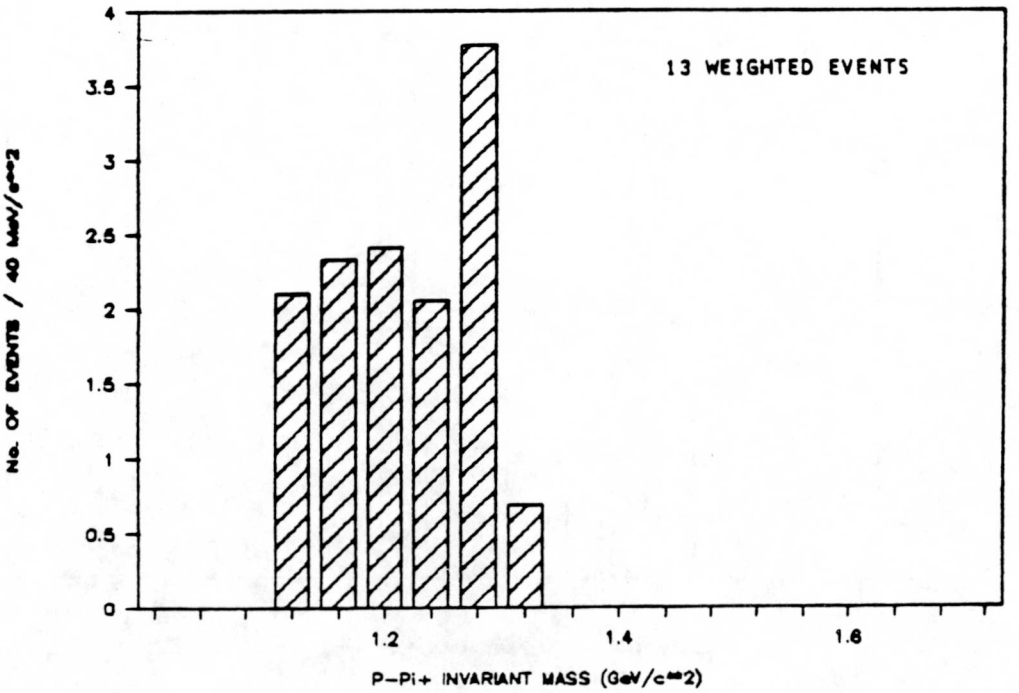

FIGURE 9-9a

WEIGHTED D P Pi- INVARIANT MASS

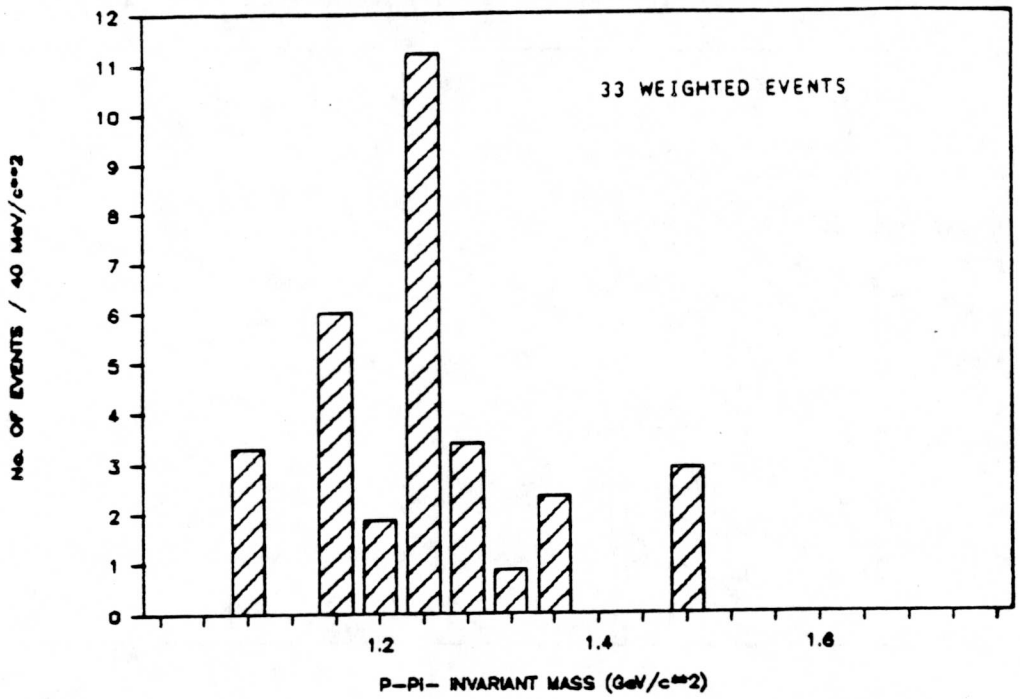

FIGURE 9-9b

WEIGHTED Ne P Pi- INVARIANT MASS

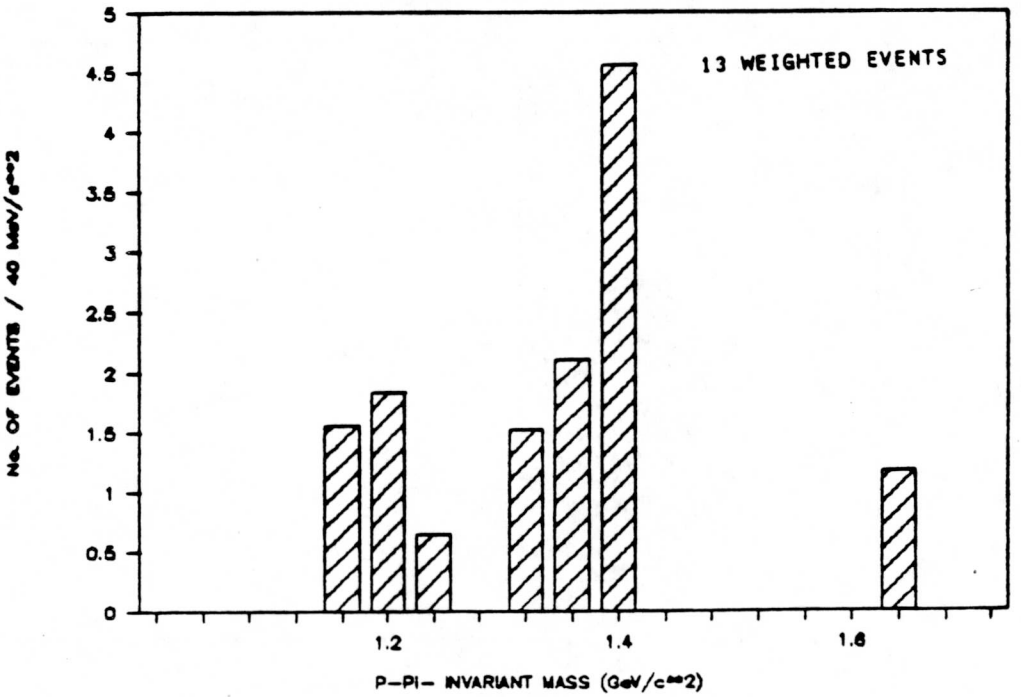

FIGURE 9-10a

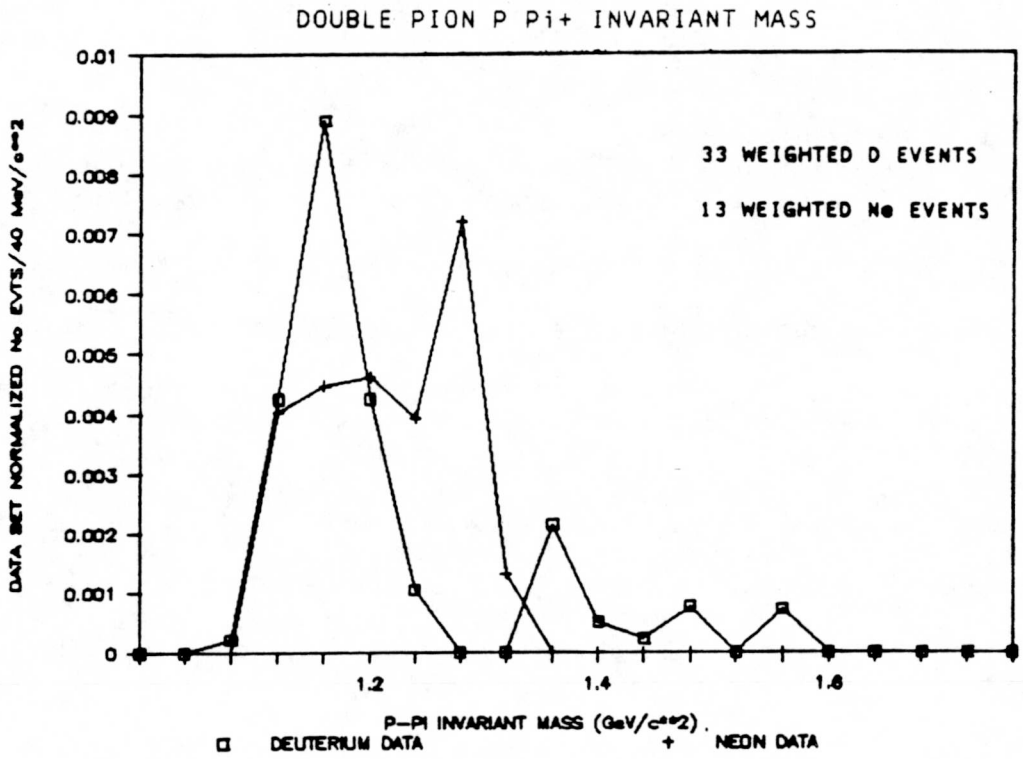

FIGURE 9-10b

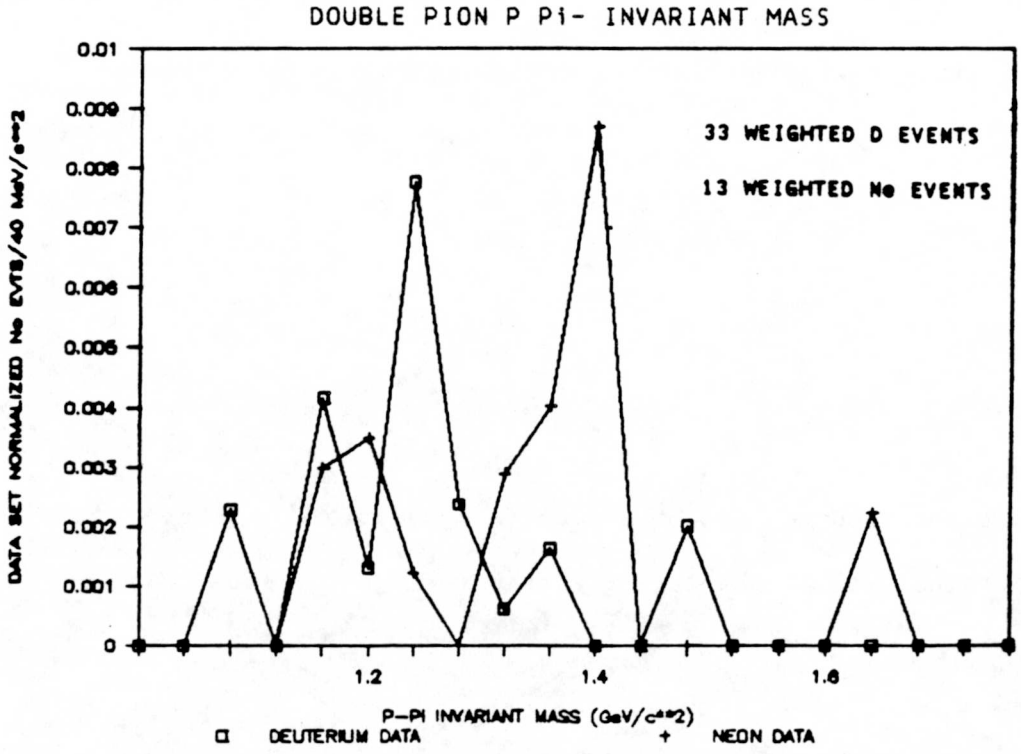

9-11, and the production angle cosine distributions, Figures 9-12, for the two data sets do not show unambiguous evidence of rescattering affecting the delta system.

9.3.3 Delta Decay Distance

The average delta momentum, using data from both exclusive channels, is 1.0 ± 0.3 GeV/c. From this momentum, the average delta decay distance can be computed and compared with the neon nuclear diameter. Starting from the Uncertainty Principle, the delta lifetime, τ, is related to its full width, Γ, by

$$\tau = h/2\pi\Gamma$$

$$= 5.73 \times 10^{-24} \text{sec.} \qquad (9\text{-}6)$$

This lifetime can be converted to a decay distance using the equation

$$\ell = \beta c \tau \qquad (9\text{-}7)$$

$$\beta^2 = 1/[1+(m/p)^2]. \qquad (9\text{-}8)$$

Using these equations and the average delta momentum, the average decay distance of the delta is 1.1 ± 0.2 fermi. Since the neon nucleus is 4.64 fermi in radius, the delta, on average, decays within the nuclear potential, although it may live long enough to get out of the dense central core.

9.4 Summary

We examined the proton and delta kinematic distributions for evidence of inelastic rescattering within the neon nucleus. The proton

FIGURE 9-11a

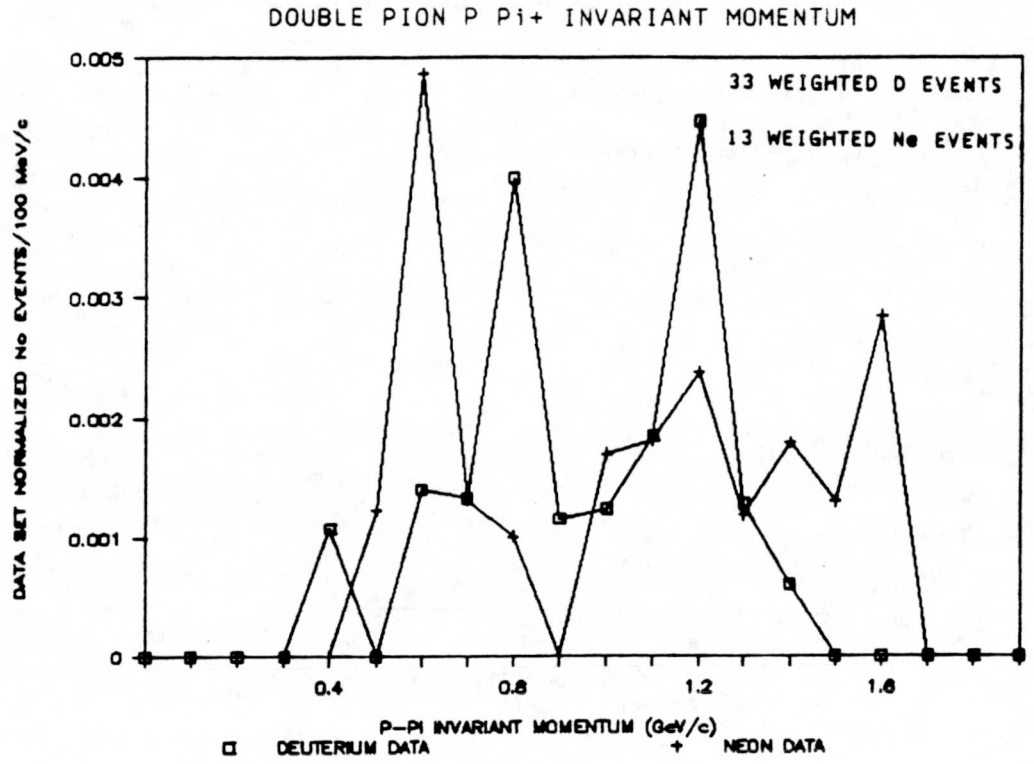

FIGURE 9-11b

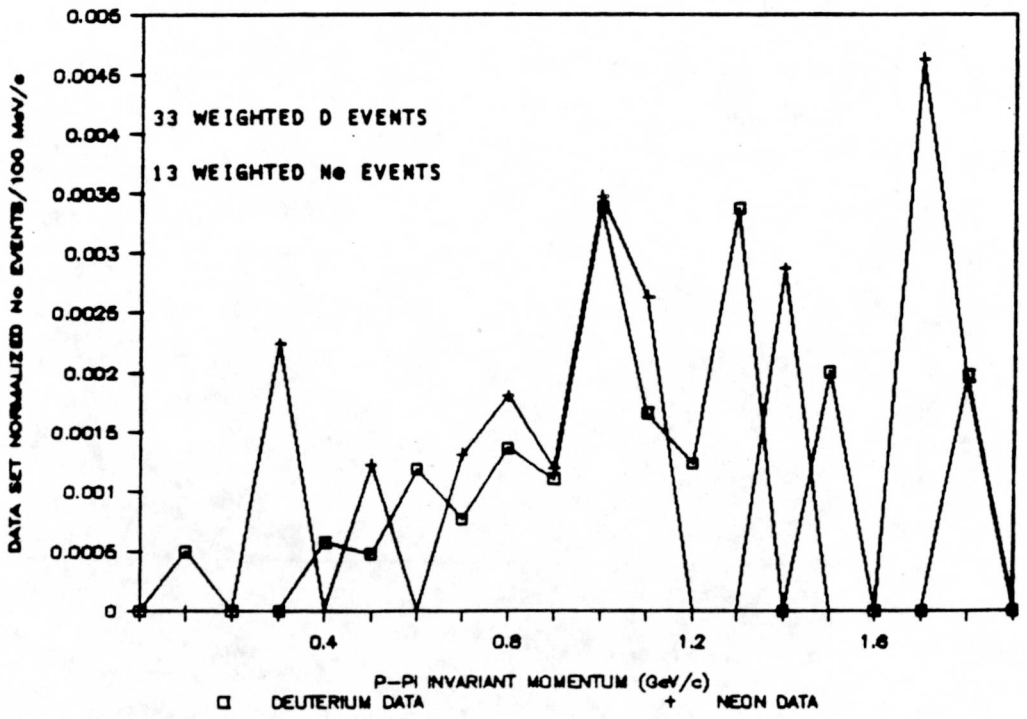

FIGURE 9-12a

DOUBLE PION P Pi+ PRODUCTION ANGLE COSINE

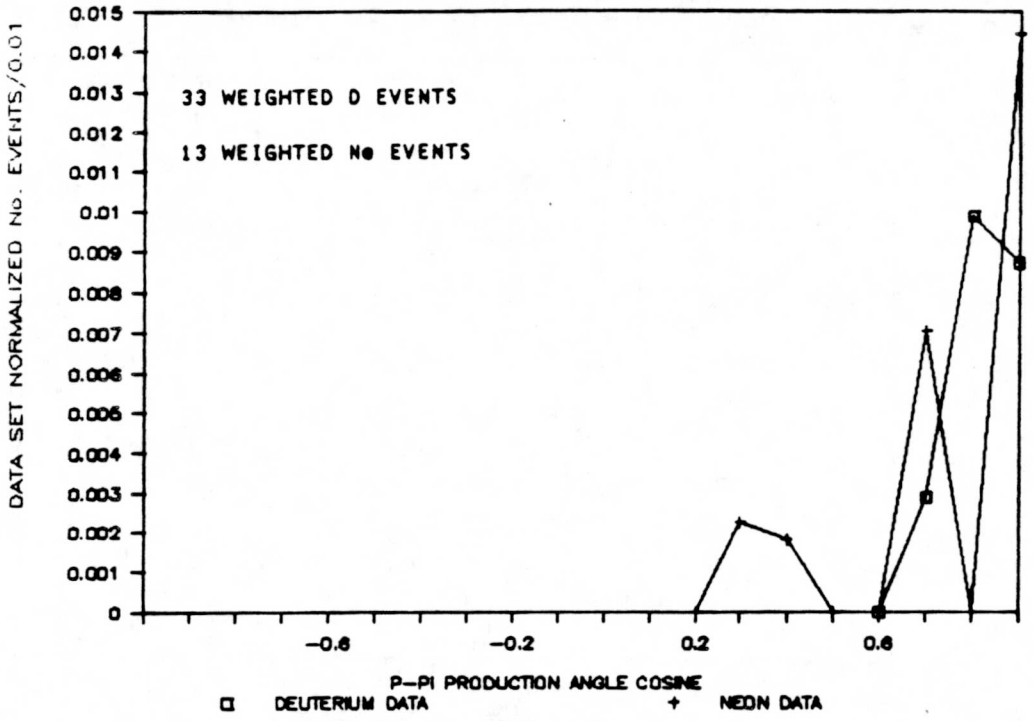

FIGURE 9-12b

DOUBLE PION P Pi- PRODUCTION ANGLE COSINE

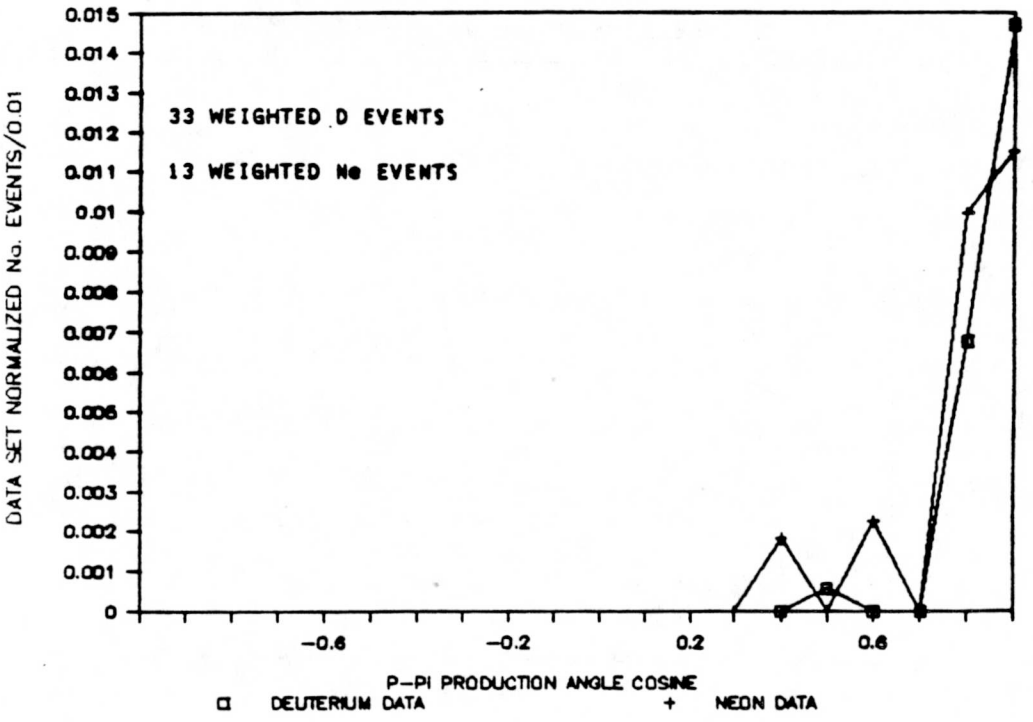

distributions show no clear evidence for intranuclear rescattering within the neon nucleus. We quantified this observation by comparing the fraction of slow, backward protons in the deuterium and neon data sets. The measured values of $f_{p \cap \theta}$ differ by -0.01 ± 0.01 and by -0.05 ± 0.06 for interaction and for spectator protons, respectively. These differences can be attributed to Fermi motion within the neon nucleus.

Examination of p-π systems revealed abundant Δ^{++} and Δ° production. Using exclusive three-constraint reaction channels, 0.51 ± 0.05 of both the D and Ne $\mu^{-}\pi^{+}p$ events result from Δ^{++} disassociation, 0.63 ± 0.17 (0.69 ± 0.25) of the D (Ne) $\mu^{-}\pi^{-}\pi^{+}p$ events result from Δ^{++} disassociation, and 0.53 ± 0.18 (0.15 ± 0.09) of the D (Ne) $\mu^{-}\pi^{-}\pi^{+}p$ events result from Δ° disassociation. In all distributions, the neon p-π invariant mass is broader in the Δ-resonance region than is the deuterium distribution. While this broadening may reflect pion scattering within the neon nucleus, it may merely reflect the poorer mass resolution of the neon experiment.

It is interesting to note that the wavelengths for pions versus delta states traversing the neon nuclei are different. The pions have de Broglie wavelengths of between 0.6 and 1.0 fermis, while the average delta has a de Broglie wavelength of 0.2 fermi. If the neon nucleus is modeled as a packed cluster of neutrons and protons, then the neon nuclear volume would be

$$V_N = 4/3\ \pi R_{Ne}^3 \qquad (9\text{-}9)$$
$$= 418.45\ f^3.$$

The spacing between nucleon in neon would thus be

$$\ell_{Ne} = (V_N/A)^{1/3}$$
$$= 2.75 \text{ f.} \qquad (9\text{-}10)$$

Thus, in this simple model, the lowest momentum pions could conceivably scatter coherently off more than one nucleon simultaneously. This effect has been reported in several low energy pion scattering experiments[3].

References

1. A.Bodek and J.L.Ritchie, Phys. Rev. D23, 1070 (1981).
2. D.Day, et al., Phys. Rev. D28, 2715 (1983).
3. D.Ashery, et al., Phys. Rev. C23, 2173 (1981).

CHAPTER 10

PION RESCATTERING WITHIN NEON: IMPLICATIONS FOR NUCLEON DECAY

10.1 Introduction

The goal of this Thesis is to measure the rates of pion intranuclear rescattering rates which can alter the final states of reactions recorded underground in massive nucleon decay search detectors. By comparing low energy neutrino interactions from neon versus deuterium targets, weighted to simulate the atmospherically-induced neutrino spectrum, the pion absorption rate and the pion charge exchange rate have been determined. For pion inelastic scattering, kinematic signatures have been observed for charged pions which set a lower limit on the inelastic rate. Only the pion elastic rescattering rate, expected to be approximately the same rate as inelastic rescattering[1], remains undetermined. The effects of pion elastic rescattering are not expected to be kinematically dramatic; the pion momentum magnitudes are unchanged and the angular deflections are small. As a result, elastic rescattering is regarded to be an unlikely final state mutilator, and so of lesser concern to nucleon decay experiments.

10.2 Summary of Rescattering Measurements

The charge exchange and absorption rescattering rates for pions were computed (Chapter 7) by matching the populations of weighted, exclusive, final state neon reaction channels to the populations of weighted, deuterium final states, using absorption and charge exchange probabilities as free parameters. A chi-squared fit of the data yielded values of 0.23 ± 0.08 and 0.05 ± 0.09 for the pion absorption and charge exchange rates, respectively.

Our measurement is in agreement with an earlier attempt to determine the pion charge exchange and absorption rate, undertaken with a much more complex nuclear medium. In a mixture containing predominantly carbon and fluorine nuclei, Lerche et al.[2] fitted the sum of pion absorption and charge exchange to be 0.36 ± 0.06. The latter result was obtained by the Gargamelle neutrino propane experiment; it corresponds to an incident neutrino spectrum which is more energetic than the atmospheric flux spectrum considered in this Thesis. Given their different neutrino spectrum, their different nuclear targets, and the more complicated character of their analysis, the Gargamelle result compares reasonably well with our determination of 0.28 ± 0.12.

The effects of inelastic rescattering were searched for by comparing low-momentum, backward-hemisphere kinematic distributions of pions, protons, and delta resonances in inclusive and exclusive reaction channels (Chapters 8 and 9). The utility of comparing this kinematic region in neon events to the same region in deuterium events was gauged by using the

muons distributions, reaction particles unaffected by intranuclear rescattering.

Muons from both the neon and deuterium data sets were represented by the total event weight (including processing and atmospheric flux weights). The fraction $f_{p\cap\theta}(\mu^-_{INC})$ was computed by determining the number of muons in each data set with $p_\mu < 300$ MeV/c and $\cos\theta_\mu < 0.0$, and dividing this number by the total number of weighted muons in the data set. The deuterium and neon values for $f_{p\cap\theta}(\mu^-_{INC})$ are equal, thereby supporting the use of this population fraction measurement as an indicator of intranuclear rescattering within nuclei.

The kinematic region constrained by the $f_{p\cap\theta}$ requirements was selected to maximize differences between the events samples which might plausibly originate with inelastic scattering effects. It must be noted that this constrained kinematic region contains only a subset of all inelastically rescattered pions; true inelastic rescattering is isotropically distributed and can degrade particle momenta throughout the momentum spectrum. Thus, any inelastic rescattering measurements made in this kinematic region are lower limits, due to both the limited constrained kinematic region and to obscuration from other processes.

With these limitations in mind, the values for the inclusive charged pion fractional population, $f_{p\cap\theta}(\pi^+_{INC})$ and $f_{p\cap\theta}(\pi^-_{INC})$ for both interaction sets were measured. The fractional population in the inclusive neon π^+ distribution is 0.03 ± 0.04 greater than in the inclusive deuterium π^+ sample, and the fractional population in the inclusive neon π^- distribution is 0.11 ± 0.10 greater than in the inclusive deuterium π^-

sample. By combining the data, we quote a lower limit for charged pion inelastic rescattering in neon of 0.03 ± 0.04.

To investigate the possibility that inelastic rescattering rates are effectively different for π^+s versus π^-s in our data, we examined π-mesons produced in the exclusive channel reaction $\mu^-\pi^+p$. Analysis of the kinematic distributions of both the deuterium and neon data for slow, backward pions show no evidence of inelastic rescattering affects. Since this channel is dominated by Δ^{++}-production, we postulate that delta production suppresses pion inelastic rescattering. This hypothesis is supported by comparing the excess (neon minus deuterium) fractional population in the slow, backward region for inclusive π^+s with the excess found in the data samples formed by removing the $\mu^-\pi^+p$ mesons from the inclusive π^+ populations. Effectively, this procedure removes a (known) source of delta production from the data and should result in a larger inelastic rescattering rate than in the (delta contaminated) inclusive π^+ samples. With the $\mu^-\pi^+p$ channel removed, an additional two percent excess in the $f_{p\cap\theta}(\pi^+_{INC})$ in neon versus deuterium is observed.

No evidence for inelastic rescattering was found in the proton kinematic distributions. The $\Delta^{++} \rightarrow p\pi^+$ invariant mass distribution from target neon nuclei is observed to be broader than the Δ^{++} width from deuterium. This broadening may be due to either rescattering effects or to poorer mass resolution in the neon experiment. The $p\pi$ resonance analysis is in accord with published studies which showed that, at incident neutrino energies near the pion production threshold, delta resonance production is

abundant. From an atmospheric neutrino spectrum, we find that 0.51 ± 0.05 of all single pion events result from Δ^{++} disassociation.

The occurence of abundant delta production in the $\mu^-\pi^+p$ reaction channel together with the absence of pion inelastic rescattering in this final state, suggests that delta production suppresses the pion inelastic rescattering process. That the suppression is more apparent in the π^+ distributions than in π^- presumably arises from the predominance of Δ^{++} over Δ° and Δ^- production. As a result, in the neon π^- distributions, we may observe more fully the affect of inelastic rescattering, whereas the π^+s are "shielded" by delta production. This shielding may be the result of the delta system carrying the pion partially out of the nucleus before disassociation, thereby reducing the number of potential scattering sites in the pion's path. More precisely, deltas may serve to transport π^+s away from the dense core region, leaving the pion to traverse a lower density nuclear periphery.

10.3 Model for Pion Intranuclear Rescattering

In the following paragraphs, we describe a phenomenological model for pion rescattering within a spherical nuclear volume of radius R_{Nuc} and of uniform density ρ_{Nuc}. With this model, it is possible to set R_{Nuc} to be the nominal value of any nucleus, such as neon. With R_{Nuc} at the neon radius, the nuclear density ρ_{Nuc} is then assigned a value whereby the model best replicates the pion rescattering results of Chapters 7 and 8. Having established the value of the nuclear density in this phenomenological way,

the value of R_{Nuc} can be subsequently re-set so that the model extrapolates pion rescattering effects to nuclei of higher atomic number.

A computer program, called INTRANUKE[3], was developed to simulate the rescattering of pions born within a nuclear medium of finite spatial extent. The program is the embodiment of a simple cascade model. Starting from a randomly selected vertex within a sphere with a user-supplied momentum vector, each pion is stepped through the nuclear medium. The particle possesses the full rescattering probability of an "external" pion at every step. The pion may emerge from the parent nucleus unscathed; or it may "bounce" one or more times. A bounce may entail a change of direction, a loss of momentum , a change of electric charge, or complete termination. For pion charge exchange and inelastic scattering, the angular deflections are taken to be isotropic. For elastic rescattering, the angular deflections are distributed in accord with 180 MeV π^--^{48}Ca elastic scattering data[4].

As presently implemented, INTRANUKE depicts a nucleus to be a sphere of uniform density, ρ_{Nuc} and of finite radial extension, R_{Nuc}. These two parameters can be adjusted to replicate rescattering behavior in a given nuclear medium. Note, however, that the INTRANUKE model does not account for delta production within the nucleus. As a result, the inelastic rescattering rates generated by the software can only be compared to the empirical π^- distributions. In this way, INTRANUKE can describe rescattering in an average way; it can be "tuned" so as to approximately reproduce the neon charge exchange, absorption, and π^- inelastic rescattering rates by adjusting ρ_{Nuc} (with R_{Nuc} = 4.64 fermis). Table 10-1 lists the charge

TABLE 10-1

INTRANUKE RESCATTERING RESULTS FOR NEON (R_{Nuc} = 4.64 f)

	Rescattering rates				Rescattering rates		
ρ_{Nuc}	Inelas	CEX	ABS	ρ_{Nuc}	Inelas	CEX	ABS
1.0	0.11	0.03	0.07	3.1	0.17	0.08	0.21
1.1	0.13	0.04	0.08	3.2	0.17	0.07	0.21
1.2	0.13	0.03	0.09	3.3	0.16	0.07	0.21
1.3	0.12	0.04	0.10	3.4	0.17	0.08	0.22
1.4	0.13	0.04	0.11	3.5	0.17	0.07	0.22
1.5	0.14	0.04	0.12	3.6	0.17	0.08	0.23
1.6	0.14	0.05	0.12	3.7	0.18	0.07	0.24
1.7	0.15	0.05	0.13	3.8	0.19	0.08	0.25
1.8	0.16	0.05	0.14	3.9	0.17	0.07	0.26
1.9	0.15	0.05	0.13	4.0	0.18	0.08	0.28
2.0	0.16	0.06	0.14	4.1	0.18	0.08	0.27
2.1	0.16	0.06	0.17	4.2	0.17	0.08	0.27
2.2	0.16	0.06	0.16	4.3	0.17	0.09	0.27
2.3	0.16	0.06	0.17	4.4	0.16	0.09	0.28
2.4	0.17	0.06	0.17	4.5	0.17	0.09	0.28
2.5	0.18	0.06	0.18	4.6	0.17	0.08	0.31
2.6	0.18	0.07	0.18	4.7	0.17	0.09	0.30
2.7	0.18	0.07	0.18	4.8	0.18	0.09	0.30
2.8	0.17	0.07	0.20	4.9	0.17	0.09	0.30
2.9	0.17	0.07	0.20	5.0	0.17	0.10	0.31
3.0	0.17	0.07	0.20				

exchange, absorption, and inelastic rescattering rates as determined using INTRANUKE for ρ_{Nuc} ranging from 1.0 to 5.0. Figure 10-1 shows these rates graphically as a function of ρ_{Nuc}. In order to match our observed signatures for inelastic rescattering, $f_{p\cap\theta}$, with the INTRANUKE results, Table 10-2 presents the excess fraction of the neon rescattered π^+ and π^- population (compared to deuterium) which is in the backward hemisphere with a momentum magnitude less than 300 MeV/c.

From the results in Tables 10-1 and 10-2, it is difficult to select a single value for ρ_{Nuc} which reflects the fitted results for the neon charge exchange rate, the absorption rate, and $f_{p\cap\theta}$ values. The INTRANUKE results yield a 0.05 rate for charge exchange at ρ_{Nuc} = 2.0 while a 0.23 rate for absorption occurs at ρ_{Nuc} = 3.6. Hence, rather than selecting a single value of ρ_{Nuc}, we note that the neon data is compatible with a range of nuclear densities from 2.0 through 3.6. Consequently, in this Thesis, we provide INTRANUKE rescattering rates with ρ_{Nuc} value set at 2.0, 2.5, 3.0, 3.5, and 4.0.

The INTRANUKE lower limit rates for π^- inelastic rescattering, listed in Table 10-2, match the neon measurements in the nuclear density range 2.5 to 3.0. Assuming that half of the π^+s result from delta production, the INTRANUKE estimate for $(f^{Ne}_{p\cap\theta}-f^{D}_{p\cap\theta})$ for inclusive π^+s (Table 10-2) can be halved to approximate observed delta production affects. Doing this for ρ_{Nuc} = 2.5 and 3.0 result in π^+ inelastic rescattering rates near the 0.03 ± 0.04 measured in the neon data.

FIGURE 10-1

INTRANUKE NEON CHARGE EXCHANGE, ABSORPTION,

AND INELASTIC RESCATTERING RATES

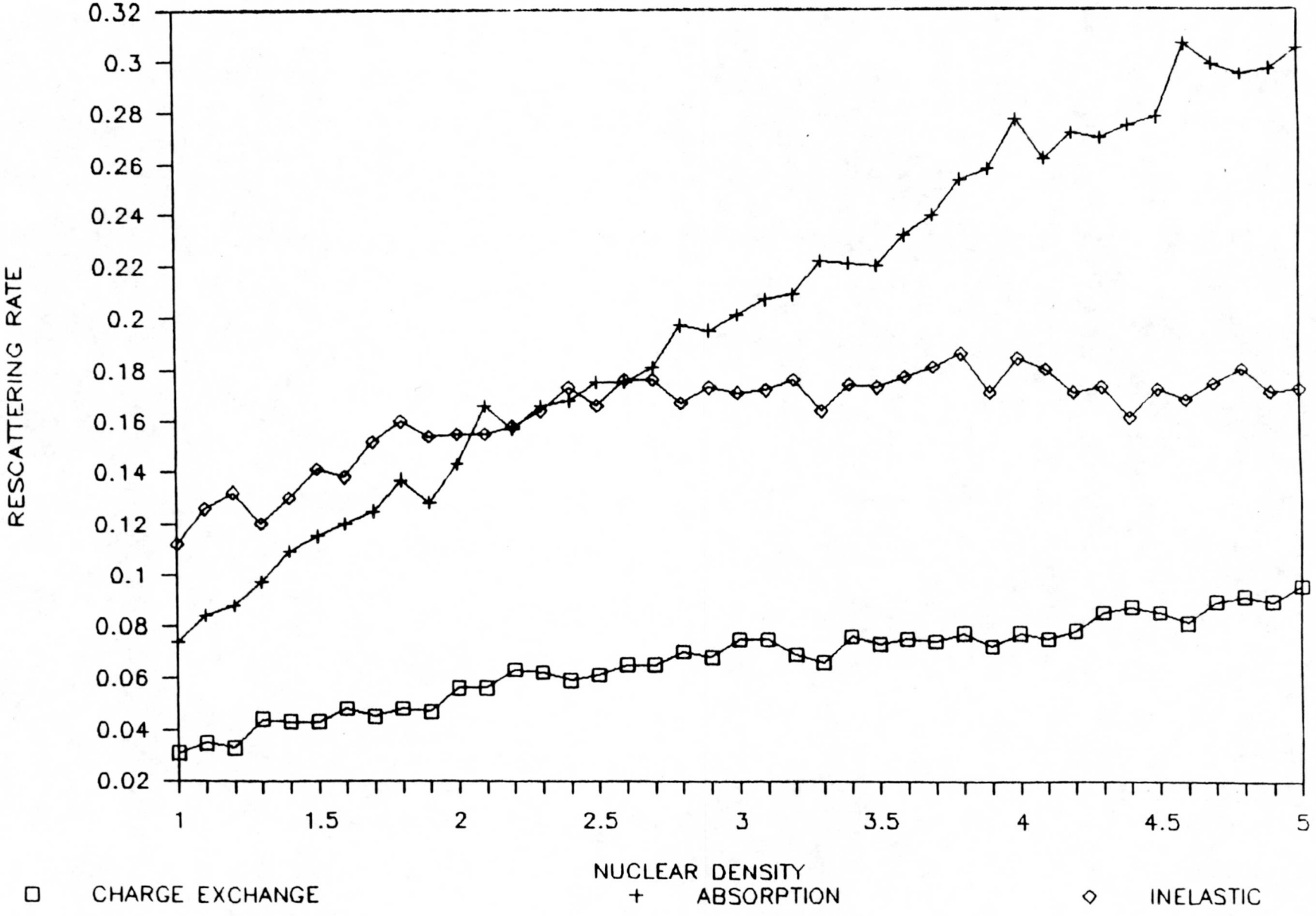

TABLE 10-2

INTRANUKE VALUES FOR $\Delta(f^{Ne}_{p\cap\theta} - f^{D}_{p\cap\theta})$

Nuclear Density (ρ_{Nuc})	$\Delta(\pi^+)$	$\Delta(\pi^-)$
2.0	0.09 ± 0.01	0.10 ± 0.01
2.5	0.09 ± 0.01	0.10 ± 0.01
3.0	0.10 ± 0.01	0.12 ± 0.01
3.5	0.11 ± 0.01	0.15 ± 0.02
4.0	0.11 ± 0.01	0.16 ± 0.02

10.4 Extrapolation to Denser Media

Having determined the nuclear density value which best reproduces the neon rescattering results, INTRANUKE can be used to predict rescattering rates for other nuclei. For the various specific values of ρ_{Nuc}, the program was run with different nuclear radii corresponding to oxygen, aluminum, argon, iron, and uranium, using the proportionality

$$R_{Nuc} = R_o A^{1/3}. \qquad (10\text{-}1)$$

The results of these computer runs are listed in Table 10-3 and shown in Figure 10-2.

Figures 10-2 provide an overview of the rescattering problems encountered by nucleon decay searchers. In order to increase a detector's sensitivity to nucleon decay without prohibitively increasing its size (and cost), detectors have been constructed which employ higher atomic number elements, thereby increasing the number of nucleons per unit volume which may decay. From Figure 10-2, it is evident that this increase in density results in an increase in the pion absorption rate. Water Cherenkov detectors, for which the decaying nucleons are mostly bound within oxygen nuclei, have absorption rates five to nine percent less than iron-based nucleon decay detectors, and four to seven percent less than argon-based detectors. The charge exchange and inelastic rescattering rates, however, are not dramatically greater in the denser detector media.

The occurrence of intranuclear pion rescattering within a nucleon decay detector serves to create erroneous events caused by atmospheric neutrino interactions and to falsify actual nucleon decays by charge

TABLE 10-3

INTRANUKE RESULTS FOR VARYING NUCLEAR RADII

Element	A	Radius (fermis)	Rescattering rate Inelas	CEX	ABS
ρ_{NUC} = 2.0					
Oxygen	16	4.3	0.16	0.05	0.13
Neon	20	4.6	0.15	0.05	0.14
Aluminum	27	5.1	0.15	0.06	0.15
Argon	40	5.8	0.16	0.06	0.18
Iron	56	6.5	0.18	0.07	0.20
Uranium	238	10.5	0.17	0.08	0.29
ρ_{NUC} = 2.5					
Oxygen	16	4.3	0.16	0.06	0.17
Neon	20	4.6	0.16	0.06	0.18
Aluminum	27	5.1	0.17	0.07	0.19
Argon	40	5.8	0.17	0.07	0.21
Iron	56	6.5	0.18	0.07	0.22
Uranium	238	10.5	0.17	0.10	0.35
ρ_{NUC} = 3.0					
Oxygen	16	4.3	0.17	0.07	0.19
Neon	20	4.6	0.17	0.07	0.21
Aluminum	27	5.1	0.17	0.08	0.22
Argon	40	5.8	0.17	0.08	0.24
Iron	56	6.5	0.17	0.08	0.26
Uranium	238	10.5	0.17	0.09	0.39
ρ_{NUC} = 3.5					
Oxygen	16	4.3	0.18	0.08	0.21
Neon	20	4.6	0.18	0.08	0.23
Aluminum	27	5.1	0.17	0.08	0.25
Argon	40	5.8	0.17	0.08	0.27
Iron	56	6.5	0.16	0.09	0.30
Uranium	238	10.5	0.16	0.09	0.42
ρ_{NUC} = 4.0					
Oxygen	16	4.3	0.18	0.07	0.25
Neon	20	4.6	0.18	0.07	0.26
Aluminum	27	5.1	0.18	0.08	0.27
Argon	40	5.8	0.18	0.08	0.32
Iron	56	6.5	0.17	0.10	0.33
Uranium	238	10.5	0.15	0.10	0.46

FIGURE 10-2a

INTRANUKE RESULTS FOR ABSORPTION RESCATTERING
AS A FUNCTION OF NUCLEAR DENSITY

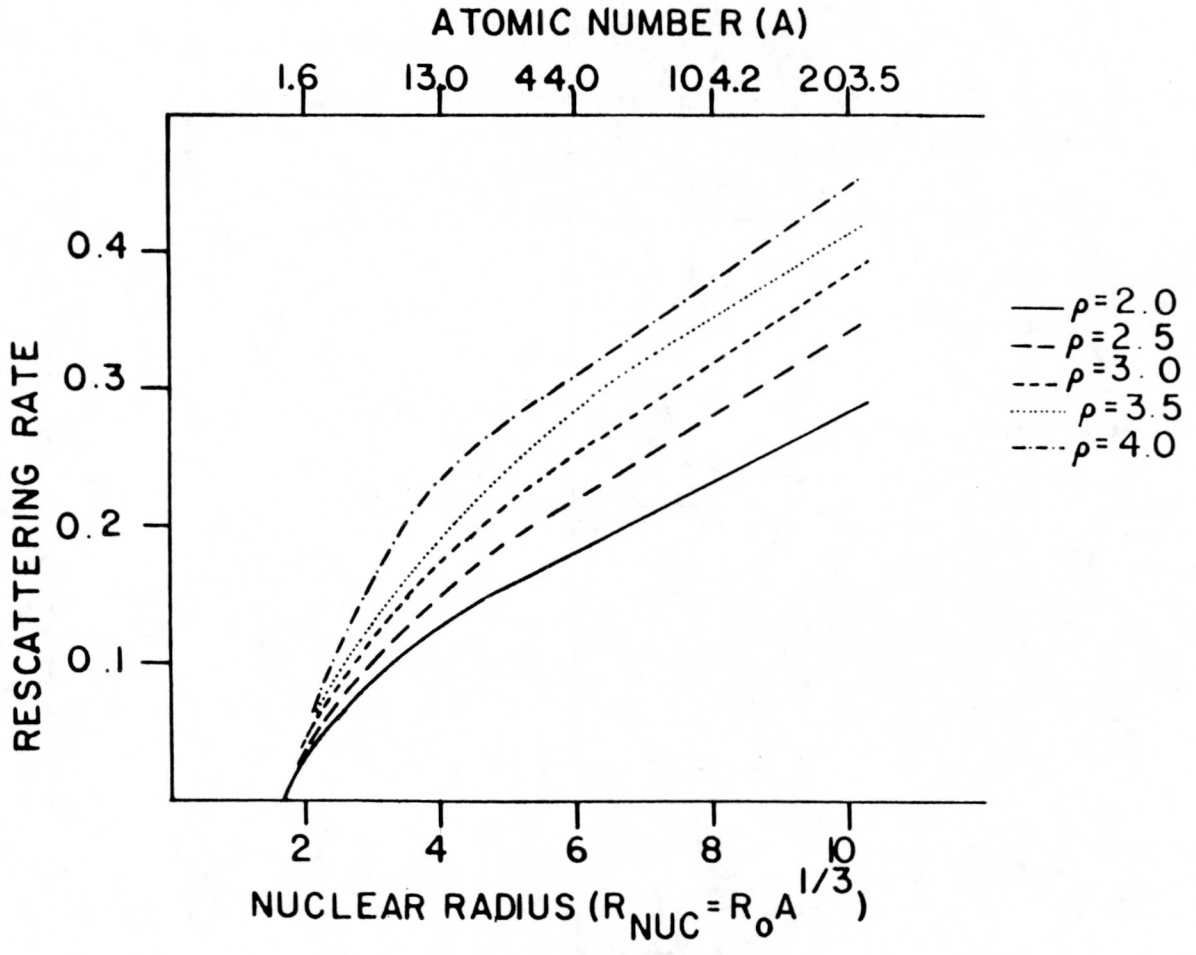

FIGURE 10-2b

INTRANUKE RESULTS FOR INELASTIC AND CHARGE EXCHANGE RESCATTERING
AS A FUNCTION OF NUCLEAR DENSITY

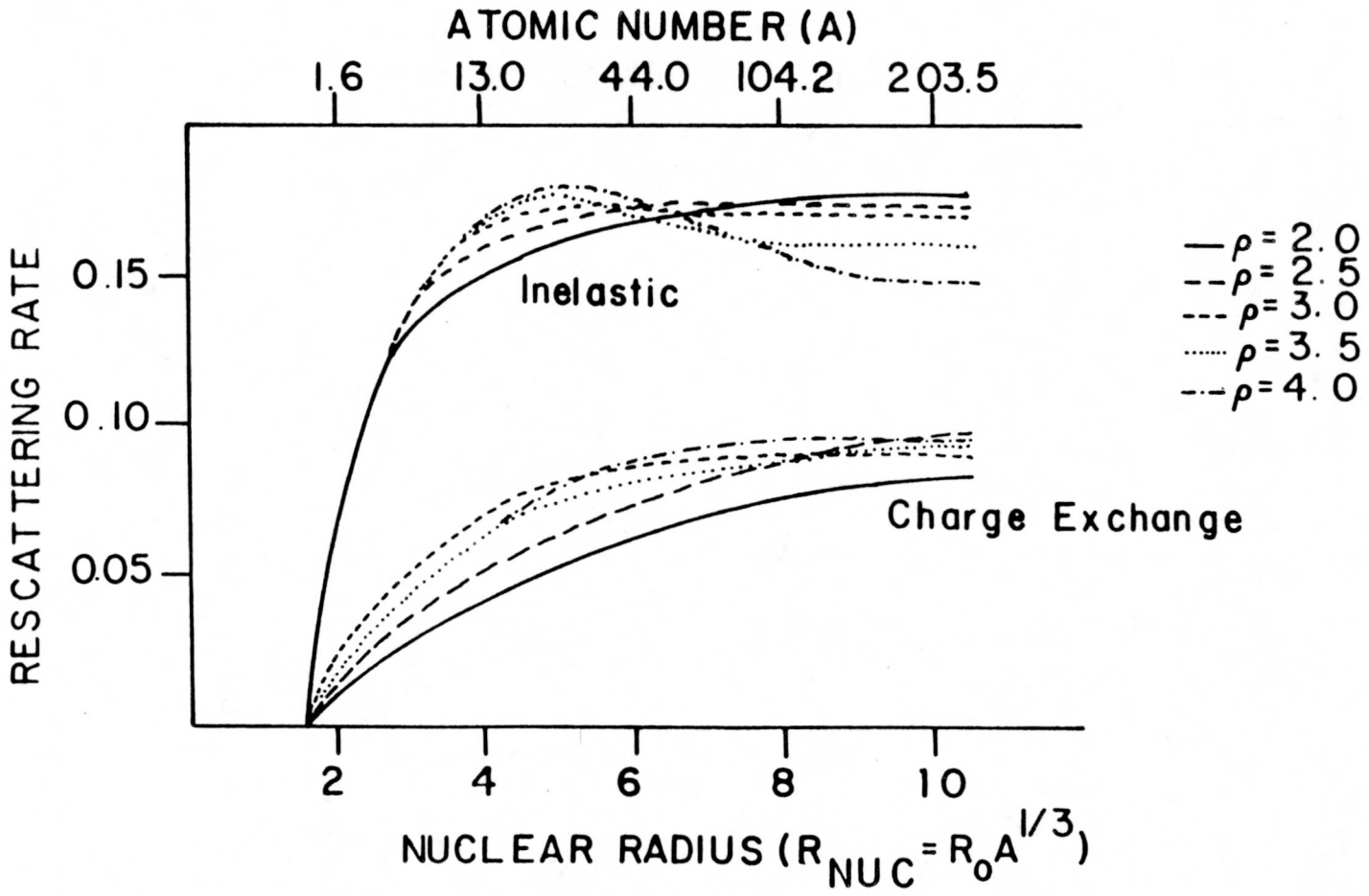

exchanging or absorbing final state pions. In going from oxygen as a detection medium to iron, the combined effects of charge exchange and absorption is expected to increase from six to ten percent - on average, one pion in 2.5 can be expected to be absorbed or charge exchanged in iron-based detectors versus one in three for water-based detectors, assuming a nuclear density of 3.5.

As the next generation of nucleon decay experiments begin to come on-line (Soudan II, ICARUS, and Sudbury), we recommend this simple phenomenologic model as a sensible, approximate way of characterizing intranuclear pion rescattering. It must be emphasized, however, that INTRANUKE employs a uniform, homogeneous sphere to model nuclear density and does not include delta production affects. Model variants, ranging from Gabriel and Goodman's three region nuclear density[5] to Miettinen and Stevenson's core and periphery model[6], can be considered.

The selection of one nuclear density model over another requires additional low energy experiments to constrain model selections and parameters. It is desirable to have more pion rescattering data from reactions on heavier nuclei initiated by "clean" projectiles (low energy neutrinos or photons). Such data, ν_μ and $\bar{\nu}_\mu$ interactions on aluminum, has been analyzed by the FREJUS collaboration. It is possible that in the future, data will become available for neutrino-argon interactions using an ICARUS prototype module or from a neutrino calibration of the Soudan II iron calorimeter.

References

1. J.Bartlett, et al., ANL-HEP-PR-81-12, Proposal: "Soudan 2, A 1000 Ton Tracking Calorimeter for Nucleon Decay", 91 (1981).
2. W.Lerche, et al., Nucl. Phys. B142, 65 (1978).
3. W.A.Mann, T.Vu, R.C.Merenyi, and W.L.Barrett, "INTRANUKE: A Phenomenological Code For Pion Rescattering Within An Extended Nucleus", ANL Note PDK-376, 1988.
4. H.Akbari and W.A.Mann, "Pion Trajectories In TWODAN", Tufts PDK Note 32, 1983.
5. T.A.Gabriel and M.S.Goodman, Phys. Rev. D25, 2463 (1982).
6. H.E.Miettinen and P.M.Stevenson, Phys. Lett. B199, 591 (1987).

APPENDIX A

ν_μ-D KINEMATIC FIT HYPOTHESIS

The neutrino and neutral hadron interaction fit hypotheses attempted for neutrino-deuterium events are tabulated. Table A-1 includes the event topology and fit constraint level as well as the reaction hypotheses.

TABLE A-1

NEUTRINO-DEUTERIUM KINEMATIC FIT HYPOTHESES

Topology	CPM	Reaction	Constraints
1 prong	1	$\nu d \rightarrow \mu^- p p_s$	3
	2	$\nu d \rightarrow \nu p n_s$	0
2 prong	3	$\chi d \rightarrow \mu^- p p_s$	0
	4	$\nu d \rightarrow \mu^- p p_s$	1
	5	$\nu d \rightarrow \mu^- p p_s$	3
	6	$\nu d \rightarrow \mu^- p p_s \pi^o$	0
	7	$\nu d \rightarrow \mu^- \pi^+ p_s n$	0
	8	$\nu d \rightarrow e^- p p_s$	3
	9	$\Lambda \rightarrow \pi^- p$	1
	10	$K_s^o \rightarrow \pi^- \pi^+$	1
	11	$\gamma d \rightarrow e^- e^+ d_s$	1
	12	$K_L^o \rightarrow \pi^- \pi^+ \pi^o$	0
	13	$K_L^o \rightarrow \pi^- e^+ \nu$	0
	14	$K_L^o \rightarrow e^- \pi^+ \nu$	0
	15	$K_L^o \rightarrow \pi^- \mu^+ \nu$	0
	16	$K_L^o \rightarrow \mu^- \pi^+ \nu$	0
	17	$\nu d \rightarrow \pi^- p p_s \nu$	0
	18	$\nu d \rightarrow \pi^- \mu^+ p_s n$	0
	19	$n d \rightarrow \pi^- p p_s n$	0
	53	$\chi d \rightarrow \mu^- \pi^+ p_s$	0
	91	$n d \rightarrow \pi^- d p_s$	1
	94	$\gamma d \rightarrow \pi^- p p_s$	1

TABLE A-1 (Continued)

Topology	CPM	Reaction	Constraints
3 prong	3	$xd \rightarrow \mu^- pp_s$	0
	4	$\nu d \rightarrow \mu^- pp_s$	1
	5	$\nu d \rightarrow \mu^- pp_s$	3
	6	$\nu d \rightarrow \mu^- pp_s\pi^o$	0
	7	$\nu d \rightarrow \mu^-\pi^+ p_s n$	0
	8	$\nu d \rightarrow e^- pp_s$	3
	17	$\nu d \rightarrow \pi^- pp_s \nu$	0
	18	$\bar{\nu} d \rightarrow \mu^-\mu^+ pn$	0
	19	$nd \rightarrow \pi^- ppn$	0
	21	$xd \rightarrow \mu^-\pi^+ pn_s$	0
	22	$\nu d \rightarrow \mu^-\pi^+ pn_s$	1
	23	$\nu d \rightarrow \mu^-\pi^+ pn_s$	3
	24	$\nu d \rightarrow \mu^-\pi^+ p\pi^o n_s$	0
	25	$\nu d \rightarrow \mu^-\pi^+\pi^+ nn_s$	0
	28	$\nu d \rightarrow \mu^- K^+ pn_s$	3
	29	$\nu d \rightarrow e^-\pi^+ pn_s$	3
	33	$\bar{\nu} d \rightarrow \pi^-\mu^+ pn_s$	3
	34	$\gamma d \rightarrow \pi^-\pi^+ pn_s$	3
	36	$nd \rightarrow \pi^- ppn_s$	1
	37	$nd \rightarrow \pi^- ppn_s$	3
	38	$nd \rightarrow \pi^- pp\pi^o n_s$	0
	39	$nd \rightarrow \pi^-\pi^+ pnn_s$	0
	40	$K_L^o d \rightarrow K^-\pi^+ pn_s$	1
	41	$K_L^o d \rightarrow \pi^- K^+ pn_s$	1

TABLE A-1 (Continued)

Topology	CPM	Reaction	Constraints
3 prong	42	$\nu d \rightarrow \mu^- \pi^+ p n_s$	(Δp_s=80 MeV) 3
	43	$nd \rightarrow \pi^- p p n_s$	(Δp_s=80 MeV) 1
	53	$xd \rightarrow \mu^- \pi^+ p$	0
	54	$xd \rightarrow \mu^- \pi^+ \pi^+ n_s$	0
	91	$nd \rightarrow \pi^- dp$	1
	92	$nd \rightarrow \pi^- \pi^+ d n_s$	1
	93	$\nu d \rightarrow \mu^- \pi^+ d$	3
4 prong	45	$xd \rightarrow \mu^- \pi^- \pi^+ p p_s$	0
	46	$\nu d \rightarrow \mu^- \pi^- \pi^+ p p_s$	1
	47	$\nu d \rightarrow \mu^- \pi^- \pi^+ p p_s$	3
	48	$\nu d \rightarrow \mu^- \pi^- \pi^+ p p_s \pi^o$	0
	49	$\nu d \rightarrow \mu^- \pi^- \pi^+ \pi^+ p_s n$	0
	50	$\nu d \rightarrow e^- \pi^- \pi^+ p p_s$	3
	51	$nd \rightarrow \pi^- \pi^- p p p_s$	1
5 prong	45	$xd \rightarrow \mu^- \pi^- \pi^+ p p_s$	0
	46	$\nu d \rightarrow \mu^- \pi^- \pi^+ p p_s$	1
	47	$\nu d \rightarrow \mu^- \pi^- \pi^+ p p_s$	3
	48	$\nu d \rightarrow \mu^- \pi^- \pi^+ p p_s \pi^o$	0
	49	$\nu d \rightarrow \mu^- \pi^- \pi^+ \pi^+ p_s n$	0
	50	$\nu d \rightarrow e^- \pi^- \pi^+ p p_s$	3
	51	$nd \rightarrow \pi^- \pi^- p p p_s$	1
	61	$xd \rightarrow \mu^- \pi^- \pi^+ \pi^+ p n_s$	0
	62	$\nu d \rightarrow \mu^- \pi^- \pi^+ \pi^+ p n_s$	1
	63	$\nu d \rightarrow \mu^- \pi^- \pi^+ \pi^+ p n_s$	3

TABLE A-1 (Continued)

Topology	CPM	Reaction	Constraints
5 prong	64	$\nu d \rightarrow \mu^- \pi^- \pi^+ \pi^+ p \pi^o n_s$	0
	65	$\nu d \rightarrow \mu^- \pi^- \pi^+ \pi^+ \pi^+ n n_s$	0
	68	$\nu d \rightarrow \mu^- \pi^- \pi^+ K^+ p n_s$	3
	69	$\nu d \rightarrow e^- \pi^- \pi^+ \pi^+ p n_s$	3
	73	$\bar{\nu} d \rightarrow \pi^- \pi^- \mu^+ \pi^+ p n_s$	3
	74	$\gamma d \rightarrow \pi^- \pi^- \pi^+ \pi^+ p n_s$	3
	76	$nd \rightarrow \pi^- \pi^- \pi^+ p p n_s$	1
	77	$nd \rightarrow \pi^- \pi^- \pi^+ p p n_s$	3
	78	$nd \rightarrow \pi^- \pi^- \pi^+ p p \pi^o n_s$	0
	79	$nd \rightarrow \pi^- \pi^- \pi^+ \pi^+ p n n_s$	0
	80	$K_L^o d \rightarrow \pi^- K^- \pi^+ \pi^+ p n_s$	1
	81	$K_L^o d \rightarrow \pi^- \pi^- \pi^+ K^+ p n_s$	1
	82	$\nu d \rightarrow \mu^- \pi^- \pi^+ \pi^+ p n_s$	(Δp_s=80 MeV) 3
	83	$nd \rightarrow \pi^- \pi^- \pi^+ p p n_s$	(Δp_s=80 MeV) 1
1[a]	98	$nd \rightarrow p n n_s$	0
2[a]	99	$nd \rightarrow n p \pi^- p_s$	0
	11	$\gamma d \rightarrow e^- e^+ d_s$	3
	9	$\Lambda \rightarrow \pi^- p$	3
	10	$K_s^o \rightarrow \pi^- \pi^+$	3

[a]Neutral induced 1 and 2 prong secondaries are fitted. The fit information is used in the primary event fit where appropriate.

APPENDIX B

EXPECTATIONS FOR MASSIVE UNDERGROUND EXPERIMENTS FROM FLUX-WEIGHTED ACCELERATOR NEUTRINO DATA

B.1 Introduction

We show in Section B.2 below that accelerator-neutrino data can be used to estimate atmospheric-neutrino final state populations. By examining the energy and momentum distributions for weighted events, background contamination channels for nucleon decay searches can be estimated, as shown in Refs. 1 and 2. In such underground experiments, final state muon tracks are commonly employed as indicators of neutrino direction. Section B.3 presents an examination of the inherent accuracy of this technique based on the ν_μ-deuterium data. Summary remarks are given in Section B.4.

B.2 Charged Current Reactions from Atmospheric Neutrinos

To approximate a charged current interaction sample induced by atmospheric neutrinos, the ν_μ-deuterium data is used. Events which pass the selection criteria of Chapter 2, and which have a fitted neutrino energy in the range $0.4 < E_\nu < 6.0$ GeV, are weighted to the atmospheric neutrino spectrum. The distribution of final states as a function of neutrino energy is then calculated. This distribution is subsequently normalized to the

atmospheric flux neutrino flux per kiloton year (kty) as calculated and approximately verified by the Mont Blanc (NUSEX Collaboration) experiment.

The normalization value is computed using the calculations of Battistoni et al.[3]; it assumes a neutrino flux ratio[4]

$$\Phi(\nu_e)/\Phi(\nu_\mu) = 1/2. \qquad (B\text{-}1)$$

According to Reference 3, there is a total of 67.6 muon-neutrino charge-current events per kty in the energy region $0.4 < E_\nu < 6.0$ GeV. This yields a normalization constant of 101 $\nu_{e,\mu}$ charge-current events per kty. Table B-1 lists the weighted, normalized final state distributions as a function of neutrino energy.

The results indicate that about 29 percent of the charged current $\nu_{e,\mu}$ interactions per kty at or below nucleon energies (that is, below 1 GeV) will result in single pion final states. These pions can subsequently rescatter in the nuclear medium, and may yield final state topologies which mimic nucleon decay.

B.3 The Muon as Estimator of the Incident Neutrino Direction

A common practice in neutrino astronomy investigations is to use the final state muon to estimate the incident neutrino direction to within seven degrees[4]. The ν_μ-deuterium data can be used to examine the reliability of this technique. For the purposes of discussing a specific momentum threshold for observing a muon, we will compare our estimations with results from the water Cherenkov detectors; however neutrino-muon directional colinearity is also invoked in the tracking calorimeter experiments.

TABLE B-1

NUMBER OF ATMOSPHERIC $\nu_{e,\mu}$-INDUCED EVENTS PER KILOTON YEAR

Total/E_ν Division

Reaction	0.4-0.6	0.6-0.8	0.8-1.0	1.0-1.2	1.2-1.4	1.4-1.6	1.6-1.8	1.8-2.0
$\nu_\ell N \to \ell^- pp_s$	9.61	10.71	7.74	4.69	2.70	2.07	1.86	1.54
$\nu_\ell N \to \ell^- \pi^\circ pp_s$	0.32	1.13	1.29	0.57	0.51	0.65	0.45	0.16
$\nu_\ell N \to \ell^- \pi^+ np_s$	0.59	0.67	0.88	1.12	0.61	0.65	0.85	0.98
$\nu_\ell N \to \ell^- \pi^+ pn_s$	0.83	2.93	3.00	2.18	1.81	1.62	1.28	1.00
$\nu_\ell N \to \ell^- \pi^+ \pi^\circ pn_s$	0.00	0.00	0.04	0.07	0.10	0.24	0.00	0.00
$\nu_\ell N \to \ell^- \pi^+ \pi^+ nn_s$	0.00	0.00	0.00	0.03	0.00	0.04	0.06	0.07
$\nu_\ell N \to \ell^- K^+ pn_s$	0.00	0.00	0.00	0.03	0.00	0.15	0.00	0.00
$\nu_\ell N \to \ell^- \pi^- \pi^+ pp_s$	0.00	0.00	0.15	0.08	0.12	0.19	0.35	0.31
$\nu_\ell N \to \ell^- \pi^- \pi^+ \pi^\circ pp_s$	0.00	0.00	0.00	0.00	0.00	0.00	0.00	0.00
$\nu_\ell N \to \ell^- \pi^- \pi^+ \pi^+ np_s$	0.00	0.00	0.00	0.00	0.00	0.07	0.00	0.00
$\nu_\ell N \to \ell^- \pi^- \pi^+ \pi^+ pn_s$	0.00	0.00	0.00	0.00	0.00	0.00	0.00	0.00
	11.35	15.44	13.10	8.77	5.85	5.68	4.85	4.12

Reaction	2.0-2.2	2.2-2.4	2.4-2.6	2.6-2.8	2.8-3.0	3.0-4.0	4.0-5.0	5.0-6.0	Total
$\nu_\ell N \to \ell^- pp_s$	1.33	0.93	0.49	0.92	0.99	1.39	1.13	0.33	48.45
$\nu_\ell N \to \ell^- \pi^\circ pp_s$	0.50	0.80	0.50	0.89	0.45	1.23	0.61	0.43	10.48
$\nu_\ell N \to \ell^- \pi^+ np_s$	0.55	0.97	1.26	0.77	0.95	2.74	0.49	0.00	14.08
$\nu_\ell N \to \ell^- \pi^+ pn_s$	0.30	1.06	0.15	0.54	0.19	1.20	0.32	0.00	18.42
$\nu_\ell N \to \ell^- \pi^+ \pi^\circ pn_s$	0.00	0.00	0.16	0.17	0.19	0.65	0.37	0.00	1.99
$\nu_\ell N \to \ell^- \pi^+ \pi^+ nn_s$	0.26	0.28	0.00	0.19	0.20	0.42	0.33	0.00	1.88
$\nu_\ell N \to \ell^- K^+ pn_s$	0.00	0.00	0.00	0.00	0.00	0.00	0.00	0.00	0.19
$\nu_\ell N \to \ell^- \pi^- \pi^+ pp_s$	0.24	0.00	0.42	0.22	0.00	0.52	0.19	0.19	2.98
$\nu_\ell N \to \ell^- \pi^- \pi^+ \pi^\circ pp_s$	0.00	0.00	0.26	0.22	0.00	0.00	0.00	0.00	0.48
$\nu_\ell N \to \ell^- \pi^- \pi^+ \pi^+ np_s$	0.00	0.00	0.00	0.17	0.00	0.34	0.00	0.00	0.58
$\nu_\ell N \to \ell^- \pi^- \pi^+ \pi^+ pn_s$	0.00	0.00	0.00	0.19	0.21	0.00	0.00	0.00	0.46
	3.18	4.04	3.24	4.28	3.18	8.49	3.44	0.95	

Some remarks concerning the operation of Cherenkov detectors are in order. The passage of a particle through a medium will result in Cherenkov radiation if the particle's velocity exceeds the speed of light in the medium. This radiation will be emitted in the form of a light cone with the particle's path acting as the symmetry axis and the angle of emission, θ_c, defined by[5]

$$\theta_c = \arccos(1/\beta n) \qquad (B-2)$$

where β is the relativistic velocity and n is the medium's index of refraction. Radiation is thus emitted when $\cos\theta_c$ is less than unity; i.e., the threshold velocity for emission is

$$\beta_t = 1/n. \qquad (B-3)$$

Since β is the ratio of particle momentum to energy,

$$\beta^2 = 1/[1 + (m/p)^2] \qquad (B-4)$$

or the threshold momentum, p_t, of a particle to produce Cherenkov light is

$$p_t = [m^2 / (n^2 - 1)]^{1/2}. \qquad (B-5)$$

For muons, this minimum threshold is 120 MeV/c in water. Medium inhomogeneities and detector inefficiencies, however, generally result in an effective threshold of 200 MeV/c for Cherenkov detection of muons in water.

This threshold is indicated on Figure B-1 which shows the distribution of muon production angle cosine as a function of momentum magnitude. This distribution is generated from the ν_μ-deuterium data weighted to the atmospheric spectrum with the neutrino energy requirement $0.4 < E_\nu < 6.0$ GeV.

Perfect alignment between muons and incident neutrinos occur at a cosine of unity. The seven degree error commonly assigned to the neutrino

FIGURE B-1

MUON MOMENTUM MAGNITUDE VS. PRODUCTION ANGLE COSINE

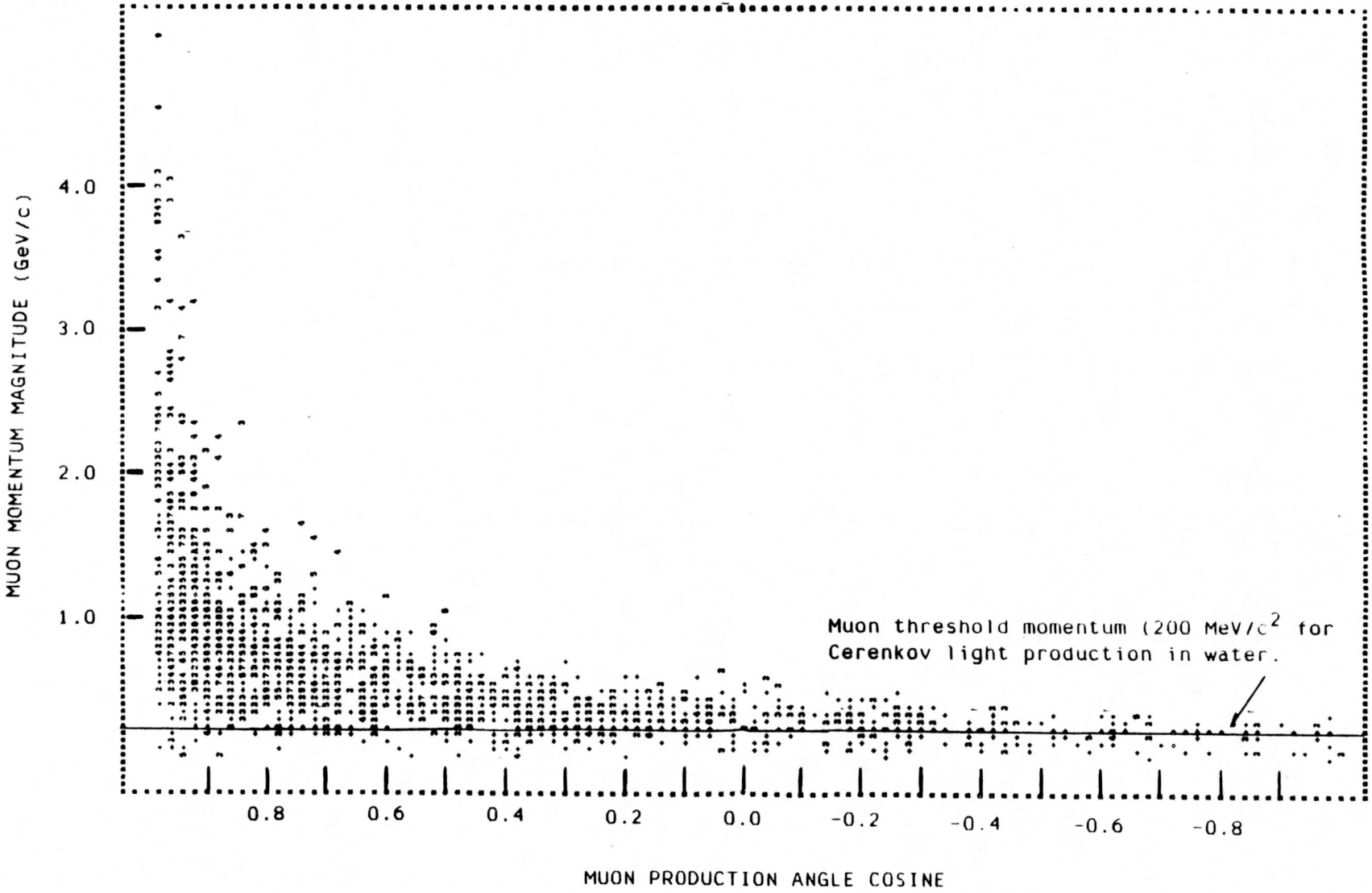

FIGURE B-2

MUON MAGNITUDE VS. PRODUCTION ANGLE COSINE
MUON MAGNITUDE GREATER THAN 2 GeV/c

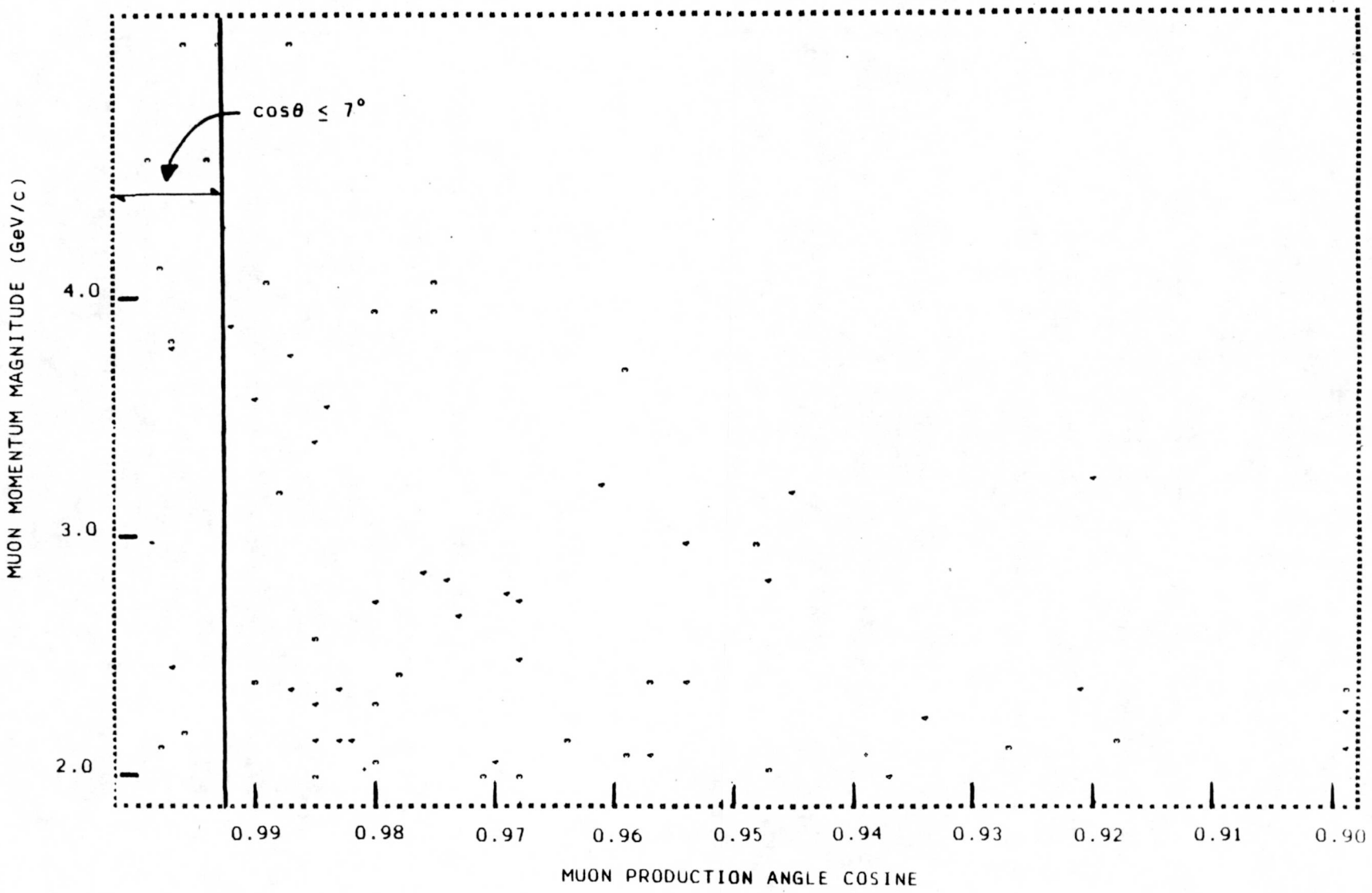

direction by Cherenkov telescopes yield a cosine value of 0.992. This is the left-most bin in Figure B-1, or approximately 0.04 percent of the above-threshold data.

Cherenkov-detected muons observed to come from below the detector are, in general, energetic, reflecting the high energy of the incident neutrinos. A general trend in neutrino interactions is that charged current muons are better indicators of directions of primary neutrinos at higher energies. To examine the degree to which this trend is operative, the muon momentum magnitude was required to exceed 2 GeV/c. Figure B-2 shows the production angle cosine distribution as a function of momentum for these particles. The seven degree uncertainty now accounts for 0.16 percent of the data. The remainder of the data deviates as much as 33 degrees from colinearity.

B.4 Summary

From our ν_μ-D event sample, we estimated the rates for charged current final states from an atmospheric neutrino flux, to occur per kiloton year as a function of neutrino energy. Of particular interest to the nucleon decay community is the distribution of events at and below the nucleon mass. In this region, single-pion production occurs with rate 29 percent of the total charged current interaction rate. This circumstance, together with the existence of nuclear rescattering, implies a significant source of background for nucleon decay.

In addition, results were presented on the use of event muons as indicators of incident neutrino directions. Based on the analysis

performed, the seven degrees uncertainty routinely applied to the resultant neutrino direction accounts for - in the ANL ν_μ-deuterium event sample - only four percent of all muons above the water Cherenkov momentum threshold of 200 MeV/c, and sixteen percent of all muons with momentum above 2 GeV/c. Our analysis finds that 95 percent of the muons with momentum greater than 2 GeV/c are within 25 degrees of colinearity and 70 percent are within 15 degrees.

References

1. M. Derrick et al., Phys. Rev. D30, 1605 (1984).
2. W.A. Mann et al., Phys. Rev SD34, 2545 (1986).
3. G.Battistoni et al., Nucl. Instrum. Methods 219, 300 (1984).
4. See for example Y.Oyama et al., Phys. Rev. Lett 59, 2604 (1987).
5. Particle Data Group, Review of Particle Properties, Phys. Lett. 170B, 1-350 (1986) p. 51.